

2014

Development And Validation Of A Hypersonic Vehicle Design Tool Based On Waverider Design Technique

Nastassja Dasque

North Carolina Agricultural and Technical State University

Follow this and additional works at: <https://digital.library.ncat.edu/dissertations>

Recommended Citation

Dasque, Nastassja, "Development And Validation Of A Hypersonic Vehicle Design Tool Based On Waverider Design Technique" (2014). *Dissertations*. 86.

<https://digital.library.ncat.edu/dissertations/86>

This Dissertation is brought to you for free and open access by the Electronic Theses and Dissertations at Aggie Digital Collections and Scholarship. It has been accepted for inclusion in Dissertations by an authorized administrator of Aggie Digital Collections and Scholarship. For more information, please contact iyanna@ncat.edu.

Development and Validation of a Hypersonic Vehicle Design Tool Based On Waverider Design
Technique

Nastassja Dasque

North Carolina A&T State University

A dissertation submitted to the graduate faculty
in partial fulfillment of the requirements for the degree of

DOCTOR OF PHILOSOPHY

Department: Mechanical Engineering

Major: Mechanical Engineering

Major Professor: Dr. Frederick Ferguson

Greensboro, North Carolina

2014

The Graduate School
North Carolina Agricultural and Technical State University
This is to certify that the Doctoral Dissertation of

Nastassja Dasque

has met the dissertation requirements of
North Carolina Agricultural and Technical State University

Greensboro, North Carolina
2014

Approved by:

Dr. Frederick Ferguson
Major Professor

Dr. John Kizito
Committee Member

Dr. Leonard Uitenham
Committee Member

Dr. Arturo Fernandez
Committee Member

Dr. Samuel Owusu-Ofori
Department Chair

Dr. Sajiv Sarin
Dean, The Graduate School

BIOGRAPHICAL SKETCH

Nastassja Dasque was born in Brooklyn, New York on March 29, 1984. She attended North Carolina Agricultural and Technical State University where she obtained her Bachelor of Science and Master of Science degrees in Mechanical Engineering.

ACKNOWLEDGMENTS

I would like to express my sincere gratitude to my advisor, Dr. Frederick Ferguson, for his guidance and support throughout the course of my Masters and Doctoral work. The time, patience and insight he has provided served as invaluable. I like to thank my committee members, Dr. John Kizito, Dr. Leonard Uitenham and Dr. Arturo Fernandez for their willingness to take part in assessing my work. I would also like to acknowledge my colleagues who assisted in performing some necessary tasks and offered suggestions.

I am extremely grateful for the technical advisement received from those at Air Force Research Laboratory at Wright Patterson Air Force Base during my visits. Their expertise served well in my growth and confidence. I would like to extend special thanks to Michael Atkinson for divulging his knowledge and expertise to me. I appreciate the Department of Defense for their generous supply of computational resources via High Performance Computing. In addition, I appreciate Foluso Ladeinde of TTC Technologies for extending access to their cloud CFD software, AEROFLO.

I am greatly indebted to friends and family who have made sacrifices and provided the moral support I needed to continue and complete the pursuit of my degree. I would like to give the utmost thanks to my daughter Janaya Dasque, the one with whom I began this journey. She provided the motivation and joy throughout my study as well as helped to keep life in perspective.

I am thankful for the funding provided for my work by the Title III fellowship program through the Department of Education.

TABLE OF CONTENTS

List of Figures	ix
List of Tables	xiii
List of Symbols	xiv
Abstract	1
CHAPTER 1. Introduction.....	3
1.1 Motivation	3
1.2 Goal of Work.....	4
1.3 Dissertation Overview.....	5
CHAPTER 2. Background.....	7
2.1 Challenges of Hypersonic Flight.....	7
2.2 Quests Towards Hypersonic Vehicle Design.....	10
2.2.1 Overview of waverider design methodology.....	13
2.2.2 Efforts towards waverider based hypersonic vehicles.....	15
2.3 Research of Waverider/Hypersonic Vehicle Performance.....	17
2.3.1 Engineering database and correlations.....	18
2.3.2 Experimental studies.....	19
2.3.3 Numerical simulation.....	21
CHAPTER 3. Development of Waverider Design and Analysis Tool.....	26
3.1 User Defined Inputs.....	27
3.2 Development of Design Space	28
3.2.1 Streamline to solid-line transformation	34
3.2.1.1 Skin friction.....	36

3.2.1.2	Stanton number.....	37
3.2.1.3	Pressure	37
3.2.1.4	Local boundary layer height.....	38
3.3	Waverider Construction Method.....	38
3.3.1	Ideal waverider formation.....	38
3.3.1.1	Use of base curve library.....	40
3.3.1.2	Parametric solid line selection function	41
3.3.2	Blunt leading edge design.....	42
3.3.2.1	Determining solid properties of leading surface	44
3.3.3	Generic stream-surface construction.....	47
3.4	Waverider Analysis	47
3.4.1	Geometric analysis.....	48
3.4.1.1	Volume	50
3.4.2	Aerodynamic analysis.....	50
3.5	Automated Grid Generation Methodology.....	52
CHAPTER 4.	Validation and Comparative Studies	56
4.1	Validation of Tool Features.....	56
4.1.1	Flow field generation validation	56
4.1.2	Streamline to solid line validation	58
4.1.3	Blunt body solid line validation.....	60
4.1.4	Surface mesh validation.....	62
4.2	Comparative Studies with Computational Fluid Dynamics (CFD).....	63
4.2.1	Euler comparative analysis	64

4.2.2 Viscous comparative analysis	69
CHAPTER 5. Conclusion	84
5.1 Accomplishments	84
5.2 Findings.....	86
5.3 Recommendations for Future Work	87
References.....	90

LIST OF FIGURES

Figure 2.1. Comparison of existing aircraft propulsion performance.....	9
Figure 2.2. Effect of L/D on range of hypersonic vehicles.....	10
Figure 2.3. Early hypersonic vehicle design of NASA.....	11
Figure 2.4. Established L/D ‘barriers’	12
Figure 2.5. Aircraft configuration with max L/D ratio for flight regime.....	12
Figure 2.6. Planar flow waveriders	14
Figure 2.7. Conical-flow waverider	14
Figure 2.8. NCAT Waverider derived Hypersonic Vehicle Configuration.....	16
Figure 2.9. L/D performance of NCAT waverider vs Bowcutt and Kuchemann.....	16
Figure 2.10. Two main blunt leading edge approaches	17
Figure 2.11. Hierarchy of CFD solvers.....	22
Figure 2.12. Flight corridor for aircrafts and aerospace vehicles	23
Figure 2.13. Earth atmosphere as altitude increases	24
Figure 2.14. Knudsen number and applicable flow equations.....	25
Figure 3.1. Design method operational Velocity, Mach and Altitude.....	28
Figure 3.2. Flight corridor used by code.....	29
Figure 3.3. Illustration of numerical process of constructing flow field	30
Figure 3.4. Illustration of directional derivatives.....	32
Figure 3.5. Example of prepared axisymmetric flow field plane	33
Figure 3.6. Example of waverider construction lines for upper and lower surface	34
Figure 3.7. Transformation of streamline definition to solid line definition	35
Figure 3.8. Construction of waverider from axisymmetric flow field.....	40

Figure 3.9. Flat top waverider.....	41
Figure 3.10. Flat bottom waverider.....	41
Figure 3.11. Derived waverider through merging	41
Figure 3.12. Illustration of blunting using control points	43
Figure 3.13. Illustration of effect of blunt factor on blunt surface	44
Figure 3.14. Illustration of heat interpolation procedure	46
Figure 3.15. Waverider with attached stream-surface duct	47
Figure 3.16. Example of elements on upper/lower surface	48
Figure 3.17. Illustration of treatment of quad elements in triangular method	48
Figure 3.18. Arbitrary elemental triangle ABC and its projections.....	49
Figure 3.19. Elemental irregular triangular prism	50
Figure 3.20. Example of a full volume mesh.....	54
Figure 3.21. Isolated surfaces of mesh.....	54
Figure 3.22. Zoom view into orthogonality at surface.....	55
Figure 3.23. Volume mesh with zone 1(blue) and zone 2(red) highlighted	55
Figure 3.24. Illustration of surface mesh	55
Figure 4.1. Illustration of radial angle and streamline perspectives	57
Figure 4.2. Comparison of semi analytical and Taylor-Maccoll solutions.....	57
Figure 4.3. Flow field streamline properties vs Taylor Maccoll solution.....	58
Figure 4.4. Validation of stanton number calculation with overlap graph	59
Figure 4.5. Validation of C_f calculation with overlap graph.....	59
Figure 4.6. Blunt body experiment conducted by Richards.....	60
Figure 4.7. Validation of blunt surface pressure.....	61

Figure 4.8. Validation of blunt heating distribution	62
Figure 4.9. Black surface mesh overlaid onto original geometry	62
Figure 4.10. Shockwave shape from pressure field from Euler results[61].....	65
Figure 4.11. Base non-dimensional pressure comparison of method and Euler results	65
Figure 4.12. Semi analytical flow field at symmetry plane	66
Figure 4.13. Comparison of pressure ratio at symmetry plane	66
Figure 4.14. Mach at base plane for Euler results.....	67
Figure 4.15. Streamlines emanating from blunt surface	68
Figure 4.16. Streamline comparison on upper surface	68
Figure 4.17. Streamline comparison on lower surface	69
Figure 4.18. Streamline distribution and boundary layer thickness recovery.....	70
Figure 4.19. Laminar vs. turbulent base plane Mach.....	71
Figure 4.20. Laminar vs turbulent base pressure ratio.....	71
Figure 4.21. Laminar pressure at symmetry plane.....	72
Figure 4.22. Turbulent pressure ratio at symmetry plane	72
Figure 4.23. Pressure field results.....	74
Figure 4.24. Shock with pressure results	74
Figure 4.25. Pressure distribution at cross-sections of one-thirds, two-thirds and base plane	74
Figure 4.26. Viscous symmetry plane results	74
Figure 4.27. Azimuthal plane (20° inclined)	74
Figure 4.28. Inviscid vs viscous lower surface pressure.....	75
Figure 4.29. Inviscid vs viscous upper surface pressure ratio	76
Figure 4.30. Turbulent vs Euler upper surface pressure	77

Figure 4.31. Viscous vs turbulent upper surface pressure ratio	77
Figure 4.32. Turbulent vs viscous lower surface pressure ratio	78
Figure 4.33. Turbulent vs inviscid lower surface pressure ratio	79
Figure 4.34. Laminar vs inviscid lower surface pressure ratio	79
Figure 4.35. Comparison of surface pressure analysis along symmetry plane	80
Figure 4.36. Turbulent vs laminar nose surface pressure ratio	81
Figure 4.37. Laminar vs modified Newtonian nose surface pressure ratio	81

LIST OF TABLES

Table 4.1. Conditions for chosen case study.....	63
Table 4.2. Aerodynamic performance comparison of analysis methods.....	83
Table 5.1. Hypersonic Vehicle Fidelity Assessment.....	86

LIST OF SYMBOLS

β	Half Shock Conical Angle
θ_c	Cone Angle
θ	Angle
$x_{1,1}$	Waverider x-nose Location
P	Pressure
T	Temperature
V	Velocity
μ	Viscosity
ρ	Density
τ	Shear Stress
q	Heat Flux
q_∞	Free stream Dynamic Pressure
γ	Ratio of Specific Heats
C_f	Coefficient of Friction
D_o	Diffusion Coefficient
D	Drag
L	Lift
G	Slip
C_D	Drag Coefficient
C_L	Lift Coefficient
A_{plan}	Planform Area
A_{base}	Base Area

h	Enthalpy
St	Stanton Number
Re	Reynolds Number
Pr	Prandtl Number
Sc	Schmidt Number
M	Mach Number
Le	Lewis Number
χ	Chi-Bar (Viscous Interaction Parameter)
δ	Boundary Layer Height
ϕ	Shape Angle
\hat{n}	Unit Normal
Pt	Cartesian Point
WR	Waverider
SL	Streamline/Solid Line
φ	Flow Field
r	Radial Component
R_c	Radius of Curvature
R_b	Blunt Radius
s	Curve length
WL	Waverider Length
ζ_{tr}	Intermittency Factor
s_{tr}	Transition Distance
κ	Curvature

S Surface Area

\vec{F} Force

Subscript

e Boundary Layer Edge

w Wall

i Point Index

j Streamline/Solid Line Index

∞ Free stream

t Total/Stagnation

D Disassociation

tr Transition

Superscript

U Upper

L Lower

K Surface Index

ABSTRACT

Methodologies required for the creation of an aircraft design tool capable of generating practical hypersonic vehicle configurations based on the waverider design concept were developed and validated. The design space for these configurations was formulated by using an algorithm that coupled the directional derivatives to the conservation laws to produce flow fields in the form of organized sets of post-shock stream-surfaces. This design space is used to construct ideal waverider configurations with a sharp leading edge. A carving methodology was also developed to transform the idealized waverider geometry into practical aircraft configurations with blunted leading edges for hypersonic mission applications. Further, methodologies, based on both empirical and analytical relations, were developed and implemented to evaluate the resulting aerothermo-dynamic performance of the resulting hypersonic aircraft configuration. In this dissertation, methodologies to determine the local pressure, skin-friction and heat flux were also developed, implemented and validated. For example, in regions where the surfaces of vehicle configuration allow for the use of planar models, the flat plate viscous relations for compressible flow were implemented in the evaluation of the local skin friction and heat flux quantities. However, in other regions, such as, the blunted leading edges, flat plate viscous relations are not applicable, and in those regions the modified Newtonian theory, Fay-Riddell theory and Modified Reynolds analogy were applied. At every stage of the creation of this design tool, the newly develop methodologies were validated using existing analytical solutions, empirical relationships, and independent computer simulation. For example, the set of streamlines that represents the inversely created hypersonic flow field generation by the technique developed herein compared particularly well to exact Taylor-Maccoll solution. Similarly, the observed relationships between the local Stanton number and skin friction coefficient with local Reynolds number along the

idealized region of the vehicle surface compared extremely well to that of experimental findings. Of particular importance to this dissertation is the creation of an automated grid generation methodology. For the purposes of independent CFD simulations, structured mesh, orthogonal to both the vehicle surface and the free stream, can be generated around the resulting hypersonic vehicle configuration. In addition, based on the users' requirements the grid information can be exported to appropriate CFD codes in their respective format. The efficacy of the grid generation methodology and the capability of the newly created hypersonic vehicle tool were analyzed. Overall, the independent CFD simulations compared well with the data predicted by the hypersonic vehicle design tool. In the areas of external flow field comparison, both methods, the independent CFD simulations and the vehicle design tool, closely recovered the exact solution described by the Taylor-Maccoll solution. In addition, the pressure distribution on the vehicle surface compares extremely well. However, the distribution of the viscous-related surface properties generated by the two methods showed some disagreements in the neighborhoods of the blunted edges. These preliminary results indicate that there may be room for improvements in the aerothermo-dynamic analysis methodologies implemented on the blunted regions.

CHAPTER 1

INTRODUCTION

1.1 Motivation

In aircraft and other transport vehicle design, there is always a desire to travel faster and farther, and to do so, conveniently and efficiently. For the most part, the designs for subsonic and supersonic vehicles have mastered these demands, unfortunately, hypersonic and space vehicles have not. Hypersonic flight vehicles are the next frontier, and the focus of this dissertation. Hypersonic transportation systems hold the promise of timely intercontinental travel as well as space access. Generally, hypersonic speeds can be considered as speeds more than five times the speed of sound. A basic feature of all hypersonic flight vehicles is the creation of relatively strong shockwaves surrounding the body. In addition, this feature is associated with severe aerothermodynamics challenges that severely limit the current capability of not only lifting air-vehicles but ballistic vehicles as well. Therefore, in either case, there are technical challenges and complexities that must be overcome if hypersonic transport systems are to be realized. Yet still, as with most aircrafts, the hypersonic vehicle shape is of fundamental importance to its aerodynamic performance, and therefore must be considered. These and other related technical challenges of interest to hypersonic flight vehicles are discussed in Chapter 2 of this dissertation.

The design of an optimized hypersonic vehicle for either intercontinental, space access or re-entry application is a complicated and multidisciplinary problem. Any acceptable design must involve an appropriate external streamlined configuration with integrated subsystems that allows for the appropriate integration of internal interfaces with optimal specifications. Research has shown that the waverider design technique can yield such streamlined configurations, and if done correctly, a complete practical integrated vehicle can be derived. Designing and building these

vehicles are not the only demands facing by the hypersonic community; in the end these vehicle must accommodate rigorous and efficient maintenance cycles. The cycle from vehicle design to first flight should be two to four years [1], not 10 – 15 years, as it now stands for subsonic transport systems. Therefore, the conceptual design and preliminary analysis phase should be streamlined and relatively quick. The methodologies must be formulated and proven for design and analysis.

1.2 **Goal of Work**

The technical efforts described in this dissertation are intended to meet the engineering developmental requirements of the hypersonic vehicle, and to validate its capabilities. In addition, this effort describes the waverider design approach and shows its versatility in constructing configurations with predictable performance characteristics of interest to the aircraft designers. Besides, this effort supports the ongoing hypersonic vehicle design challenges at North Carolina A & T State University (NCAT) [2-6], and as a whole, has served to push the creative envelop in this field [2-6]. A summary of the technical contributions is documented in Chapter 2. The overall goal of this dissertation is to formulate and compile a waverider-based method that can potentially support the creation of an engineering design tool with capabilities to aerodynamically design and analyze generic hypersonic vehicles during its conceptual design phase. If proven successful, the engineering tool based on the waverider design philosophy, developed herein, can potentially support ‘expedited hypersonic vehicle creation’ initiatives.

In this effort, the inverse design method uses the hypothetical streamlines within a hypersonic flow field as bases upon which stream surfaces are formulated. In turn, these stream surfaces are pieced together to construct engineering configurations. Finally, these configurations are manipulated to result in complete geometries, that when analyze delivers hypersonic vehicles with superior aerodynamic performance. In other words, the hypersonic flow acts as the design

space from which the resulting hypersonic vehicles for specified flight mission are carved. A generalized tool, especially one that is designed to create and analyze waverider configurations with and without modification, as well as, to assist in its independent verification is valuable to the hypersonic community. Currently, there is a lack of readily available tools, especially those capable of designing a fully integrated hypersonic vehicle, much less, and one that adheres strictly to the waverider design methodology. The currently available tools, matured and in development, offer the engineer a limited design space, and thus, a limited variety of waverider-based hypersonic configurations. In addition, these tools rely on less sophisticated and physics based methodologies in their vehicle construction process. Furthermore, any vehicle construction tool must be capable of accurately formulating a variety of post-shock flow fields, extract a large variety of waveriders and analyze resulting configurations. The design tool, formulated and described herein, is engineered to design, analyze and prepare waverider configurations for independent validation investigations. In efforts to independently validate the waverider-based vehicle design process, a variety of waverider configurations with predictable performance were developed and analyzed. These configurations were first analyzed using the newly developed tool, which was based on the engineering procedure constructed herein. Next, the configurations were imported into a set of sophisticated CFD tools, developed by AFRL at the WPAFB, and independently analyzed for comparison. The results of this validation study are documented in Chapter 4 of this dissertation.

1.3 **Dissertation Overview**

This dissertation consists of five Chapters. Chapter 1 highlights the need for the research effort that supports this dissertation, justifies the technical approach adopted herein and briefly describes its accomplishments. Also in Chapter 1, the potential impact of the ‘waverider-based hypersonic vehicle construction’ process is discussed in relationship to other competing efforts.

Of importance to note, in Chapter 1, the description of the research goals associated with this dissertation is clearly layout. In addition, all information that supports the rational for this research, and the technical challenges behind the engineering methods used in this effort are described.

Chapter 2 will provide the reader with background information that reinforces the need for such a tool as well as previous efforts and methods that provide the basis of the tool. Chapter 3 provides the detailed methods used regarding the design space generation, geometric construction, analysis, and automated grid generation. Here, methods were used and built upon creating a blueprint on how one can go through the design and analysis process employing strategic modifications and coupling of methods. The preliminary analysis performed by tool takes into account the viscous effects. Chapter 4 demonstrates the validation of the methods employed and formulated. In addition, comparative studies with independent analysis using Computational Fluid Dynamics (CFD) are presented. Chapter 5 will provide a summary of the work completed, findings and recommendations for future work.

CHAPTER 2

BACKGROUND

2.1 Challenges of Hypersonic Flight

The potential benefits derived from the practical implementation of reusable hypersonic flight vehicles are very desirable for all developed societies. However, the natural phenomena that occur during hypersonic travel within the atmosphere introduce technological challenges that render the development of such a vehicle an impossible task. The technical complexities associated with the development of reusable hypersonic vehicles that are capable of controlled performance while withstanding sustained high temperature in a low density aerodynamic environment are enormous. These natural phenomena which define hypersonic speed discussed by Anderson [7] are the following;

- the generation of shockwave due to the flow turning into itself causing large flow property and entropy gradients
- high level of viscous interaction between the fluid and wetted surface of the hypersonic object causing high heat flux on surface and thick boundary layers
- thin shock layers due to the close vicinity of the generated shock to the surface trapping high temperature flow around the hypersonic object.

This reality produces extremely large heat loads, which no current materials can endure for long periods. Therefore, material options for hypersonic vehicles are very slim and the residence time in the hypersonic regime very limited. The major technological challenges in this instance are the undesirable properties of existing materials and limited capabilities of existing thermal protection systems. Consequently, two hour travel at hypersonic speed pose very great challenges.

Furthermore, there are limited options and capabilities of current propulsion systems to provide and sustain the thrust required for hypersonic speeds. Thus far, all successful hypersonic crafts such as missiles and spacecraft use rockets to provide the thrust needed to achieve hypersonic speeds. Rockets, which have proven to be very effective, are expensively inefficient and dangerous. The required fuel accounts for a large portion of the take-off weight and success of rocket propulsion requires a very accurate and precise design of explosions. Alternatively, with the recent successful test flights of the X-51A[8] and X-43A[9], the scramjet is showing promise as another feasible option for hypersonic propulsion. The scramjet is a dynamic thrust air-breathing propulsion system that uses oxygen from the atmosphere as fuel. This feature dramatically decreases the weight of the required onboard fuel[10] and entails higher performance efficiency than rockets as shown in Figure 2.1. There's also research efforts in the design of the Magneto hydrodynamics(MHD) supersonic turbojet engine[11, 12] which is projected to be capable of operational speeds of Mach 0-7 utilizing existing technology. Both the scramjet and MHD supersonic turbojet are immature technologies still undergoing research studies and are not yet ready for extensive practical use.

Currently, rocket technology is the most mature hypersonic propulsion technology having been relied upon for space access missions throughout the world. For example, the United States of America has relied heavily upon rocket technology for the space shuttle program for 30 years in order to acquire manned access to space. However, the space shuttle program has been retired. Consequently, accessibility to space from the USA has virtually been eliminated leaving US astronauts to rely on other nations such as Russia for service into space. The current voids in America's means of space access and travel calls for a drive to develop a revolutionary space vehicle with relatively low cost, high reliability and reusability features. Such a task requires a

multidisciplinary effort. With the rapid evolution and innovation of technology in computing, materials, vehicle design, propulsion, manufacturing and other areas of interest, the environment for such a vehicle to be born is approaching.

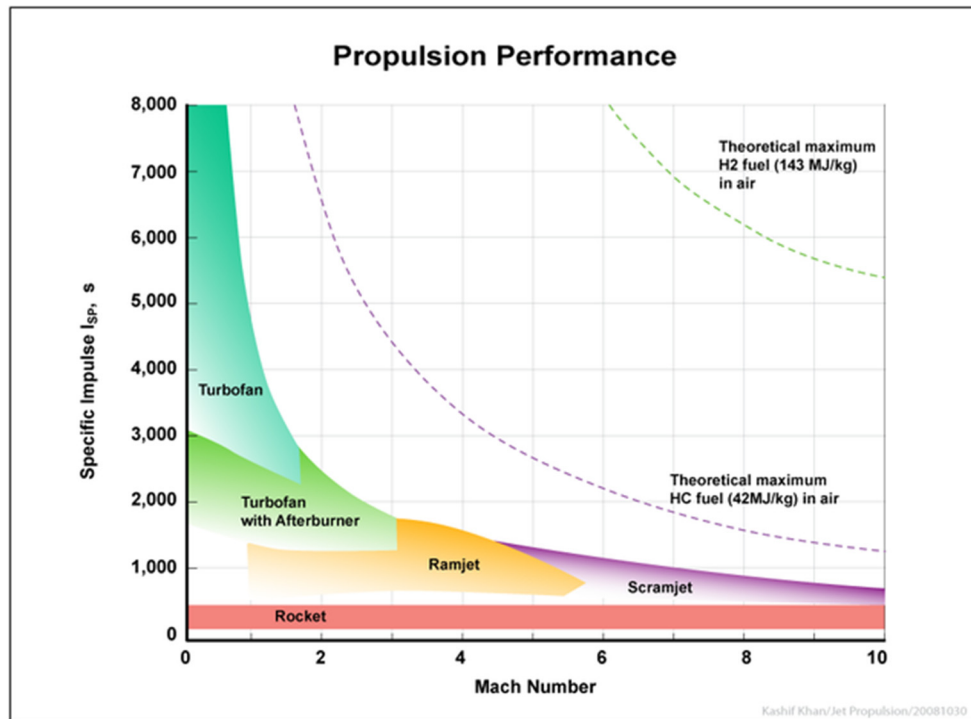


Figure 2.1. Comparison of existing aircraft propulsion performance[13]

In addition, there is a desire in pockets of humanity to create a space faring culture. Therefore, future space missions call for a vehicle to not only be aerodynamically efficient/effective within earth's atmosphere but extraterrestrial atmospheres as well[14]. For example, Mar's atmosphere is much thinner than earth's at about 1% of Earth's atmospheric height. The entry speed into Mars is very high around 5km/s. Clearly, a manned mission to Mars entails many safety and life sustainability challenges. Landing safely with life and equipment intact in such a reality is a challenge for the vehicle designer. This desire creates a need for a vehicle to be able to maintain flight while adequately reducing speed through the atmosphere for a relatively low impact landing and g-force experience. This technological challenge can be

approached from many fronts resembling such things as counter thrust and flow control mechanisms. However, a vehicle's geometric design naturally contributes aerodynamic effects within an atmosphere without the use of powered systems. An aerodynamic characteristic of a vehicle that is indicative of its glide performance is its lift to drag ratio (L/D). Figure 2.2 illustrates the effect of the L/D on a hypersonic vehicle's range.

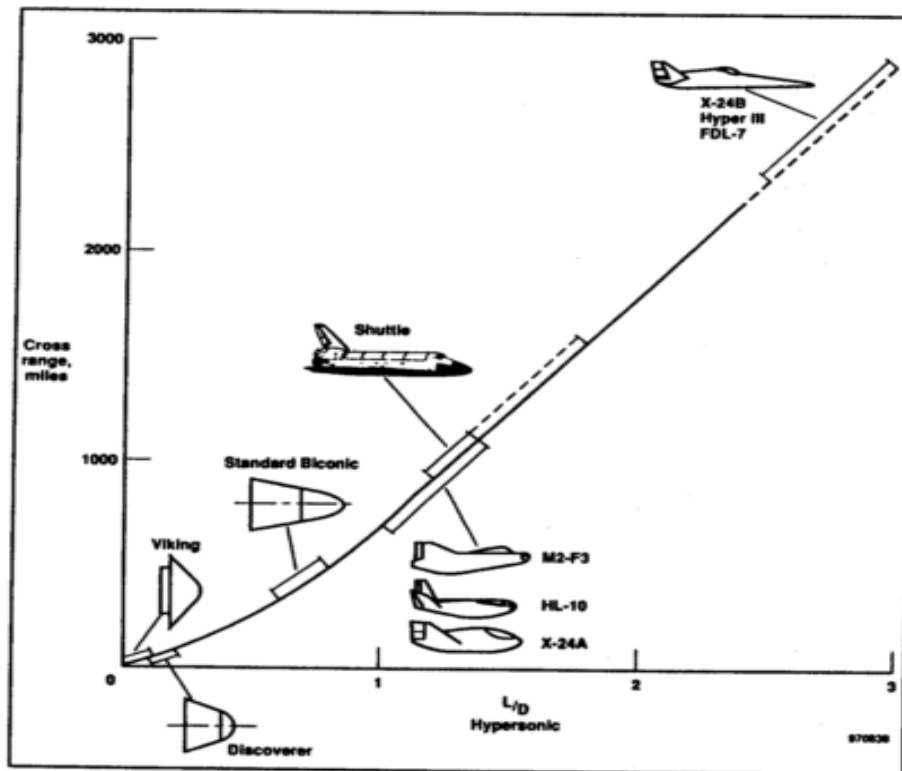


Figure 2.2. Effect of L/D on range of hypersonic vehicles [15]

2.2 Quests towards Hypersonic Vehicle Design

During the early quest for hypersonic flight, NASA [7] designed, constructed and tested a hypersonic vehicle. The vehicle, illustrated in Figure 2.3, demonstrated that it was capable of achieving speeds up to Mach 8. However, a closer look at wind tunnel data revealed an interesting phenomenon. It was observed that the vehicle's aerodynamic performance parameter L/D decreased as Mach number increased. Consequently, Kuchemann[16] conducted extensive

empirical studies of supersonic/hypersonic research and vehicle performance of that time over a range of Mach numbers and documented the trend that the maximum L/D observed decreased as Mach number increased establishing the ‘L/D barrier’. This detail highlights another challenge in the realization of hypersonic flight vehicles; the traditional aerodynamic designs and design methodology were not effective in the hypersonic regime. Later, Bowcutt[17] showed optimized viscous waveriders derived from conical flow fields; follows a similar trend but breaks the Kuchemann’s ‘L/D barrier’ yielding geometric configurations with relatively higher L/D ratios at higher Mach numbers.

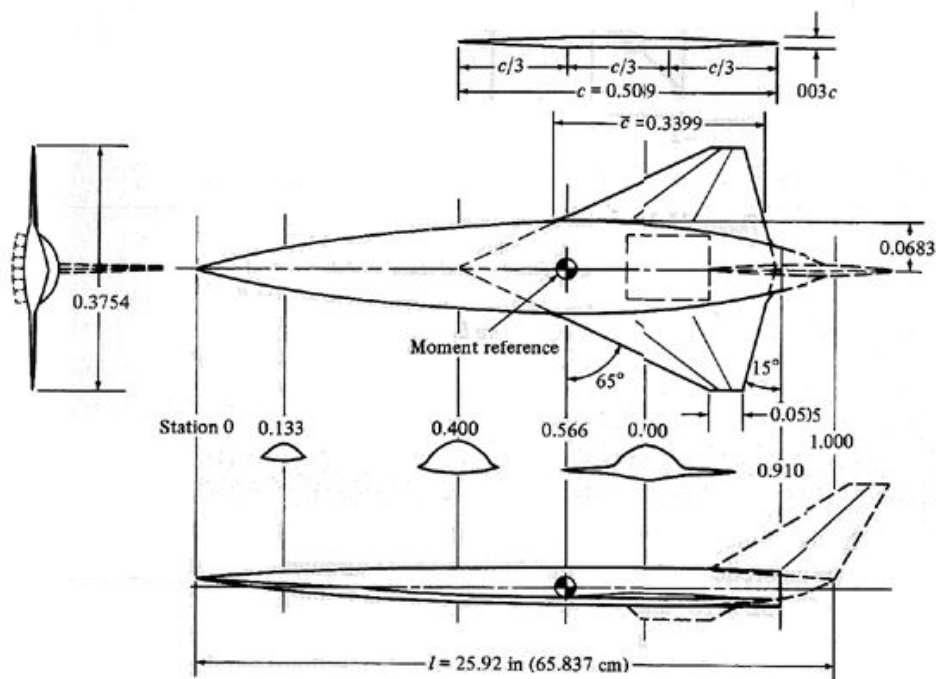


Figure 2.3. Early hypersonic vehicle design of NASA[7]

Bowcutt’s findings were later supported by others[18, 19]. Figure 2.4 illustrates the comparison of findings of Kuchemann, Bowcutt and Corda; the open circles represent experimental data obtained from flight tests and experiments, Kuchemann established the solid line and Bowcutt established the broken line. The work of Bowcutt renewed interest in the waverider design

technique that was first introduced in the 1950's by Nonweiler[20] in his attempt to design a hypersonic wing for re-entry purposes. Figure 2.5, established by Kuchemann, represent vehicle configurations that will likely achieve maximum L/D in their respective flight regime. The trend shows a highly integrated vehicle configuration with aerodynamic and propulsion features fused together would fare as the optimum aerodynamic configuration for the hypersonic regime. The waverider design methodology inherently yields geometries that support this type of configuration.

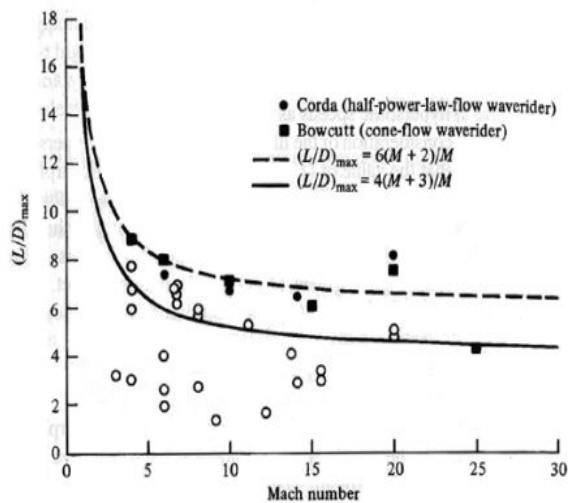


Figure 2.4. Established L/D 'barriers'[18]

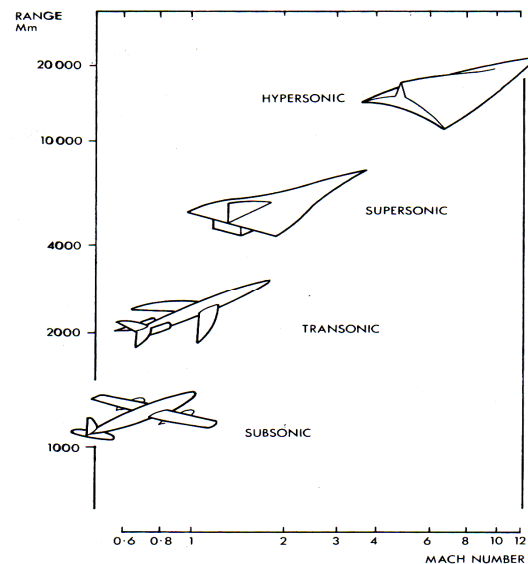


Figure 2.5. Aircraft configuration with max L/D ratio for flight regime[16]

A waverider is a hypersonic vehicle configuration designed such that the high pressure due to the shockwave generated is only seen by the lower surface of the vehicle. This configuration is achieved through an inverse design methodology that sets the leading edge of the geometry onto a generated shock. At the time of its creation, the waverider design concept solved a major re-entry problem by yielding configurations with the L/D needed for long-range glided re-entry landings. However, the leading edge of a waverider is inherently sharp which yields an extreme aerothermodynamic load. Also, early configurations[21] of the 1950's and 1960's were thin and

presented limited ‘volumetric efficiencies’ and their performance analysis did not consider viscous effects. After all, computational resources in the 1950s were not available to produce a wider range of configurations or perform viscous analysis due to their computational load. These circumstances rendered waveriders unrealistic at the time. However, the work of Bowcutt during the 1980s optimized waveriders by implementing established engineering relations and computational resources to predict the viscous effects on performance. With the renewed interest, many more research efforts of and with the waverider followed. However, even with the excitement of the waverider’s potential, its design methodology has yet to extend to a practical design of a working hypersonic vehicle.

2.2.1 Overview of waverider design methodology

Waveriders are designed as products of a hypersonic flow environment through an inverse design methodology. The inverse design approach uses the streamlines of a post shock inviscid flow field as the design space for the compression stream surface (usually the lower surface) of waverider geometries. The waverider methodology ideally produces a ‘streamlined’ geometry for the hypersonic flow regime. The lower surface formed by a set of neighboring streamlines yields the attachment of the leading edge to the shock. This task can be achieved in a variety of ways. The two most used techniques are:

1. prescribing the leading edge onto a shock and extracting the set of streamlines which emanate thereof and
2. prescribing a base curve which crosses the shock and extracting the set of streamlines that intersect the prescribed curves.

The chosen post-shock streamlines are matched to create the lower compression stream surface of a waverider. It is assumed that the stream surface designed does not greatly interfere with the

overall flow field, thereby keeping the shock attached to its leading edge and permitting undisturbed free stream flow along the upper surface. The upper surface is usually formed by lines set parallel to the free stream flow emanating from the leading edge[22]. It is imperative to predetermine the streamlines of a post-shock flow field accurately in order to formulate and analyze a true waverider configuration.

Popularly used post shock flow fields are planar and conical shocks. This is primarily due to the existence of their analytical solutions. For planar shocks, the oblique shock relations with free stream conditions are used to solve for the flow field. The flow field of a conical shock wave has an analytical axis-symmetric solution expressed by the Taylor-Maccoll equation[23]. Examples of waveriders formed from planar and conical flow fields are shown in Figure 2.6 and Figure 2.7, respectively. Between the two, conical flows are more popular due to the wider range of waverider geometries that can be extracted from such flow fields. In addition, waveriders derived from conical flow have larger volume efficiencies and pressure increases along the streamline, which can increase the aerodynamic performance, L/D as well as stability.

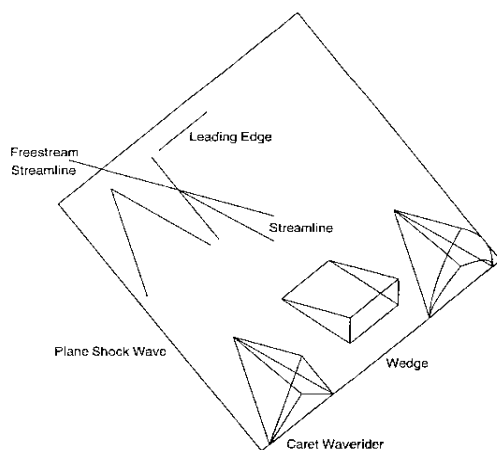


Figure 2.6. Planar flow waveriders

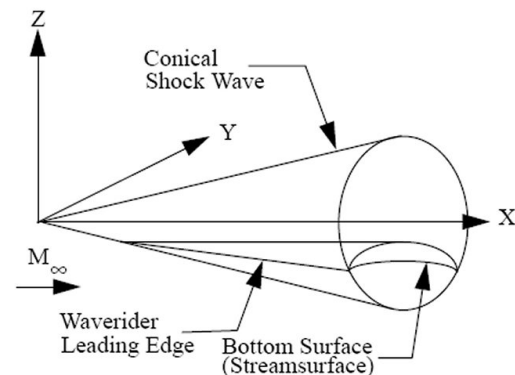


Figure 2.7. Conical-flow waverider[19]

2.2.2 Efforts towards waverider based hypersonic vehicles

Since the introduction of waveriders, there has been work done to show the possibilities and potential of its design methodology. The nature of the inverse design methodology links the variety of configurations to flow field shape. The work of Bowcutt utilized the Taylor-Maccoll method to form a conical design space. Hence, the optimized configurations of his work were from a design space of limited possibilities. Clearly, design spaces beyond planar and conical hypersonic flow fields will yield larger possibilities of configurations and performance. There has been a variety of work done to determine other types of flow fields (design space). Ferguson[2], Jones[24] and Sobieszczyk[25] used marching schemes to determine flow field from arbitrary shock shapes. Others have developed design spaces by manipulating and perturbing conical/analytical flow fields [26-28]. Some have utilized computational fluid dynamic methods to formulate flow fields to use as a waverider design space[18, 29].

The basic waverider usually serves as the fore body of a complete hypersonic vehicle as with the X51 and X43A. The design methodology can also be exploited to produce streamlined surfaces from one flow field that intersect with a waverider body to formulate other parts of the vehicle such as an engine inlet as shown by Dhanasar[30] creating an integrated vehicle. The aft body can be of stream surfaces made from an expansion flow field[17, 22]. More 'complex' geometries can be obtained using multiple flow fields[31, 32]; free stream, post-shock as well as expansion flows; through the merging stream-surfaces and bodies. Hence, an integrated hypersonic vehicle purely from the waverider design methodology [4, 5, 33-36] can be formed. An optimized vehicle derived from the wide variety of possibilities may have exceptional aerodynamic performance with appropriate volume compared to known designs to date. For example, Zhang et al [37] formulated optimized hypersonic vehicles, illustrated in Figure 2.8, from multiple planar shock flow fields

which showed to have good aerodynamic performance, shown in Figure 2.9, with design points beyond Bowcutt L/D curve of waveriders derived from purely conical flow fields.

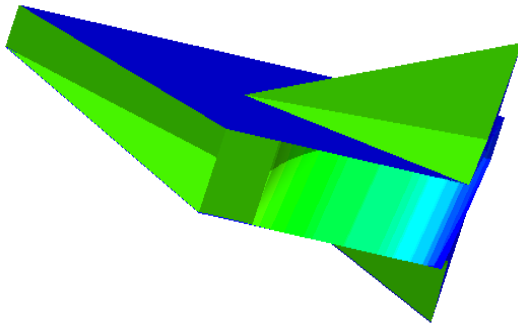


Figure 2.8. NCAT Waverider derived Hypersonic Vehicle Configuration[37]

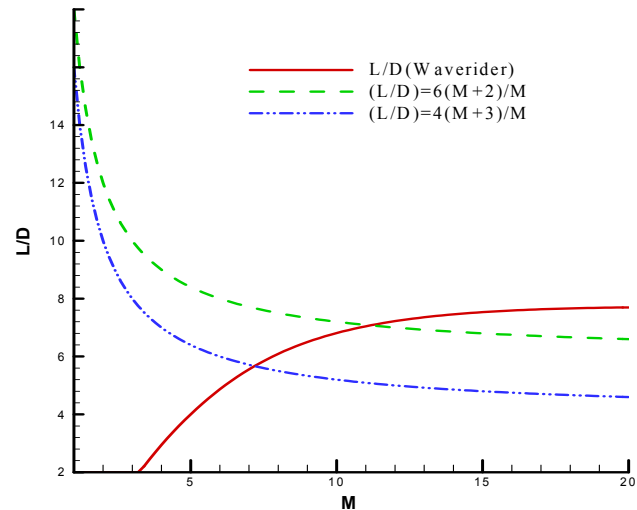


Figure 2.9. L/D performance of NCAT waverider vs Bowcutt and Kuchemann[37]

In order to produce a practical waverider based vehicle design, the inherent sharp leading edge must be handled. Therefore, a practical design tool must incorporate blunting techniques to handle this task. Blunting the leading edge as well as areas where two stream surfaces meet relieves heating effects and yields a more realistic shape for manufacturing processes. On the other hand, blunting inherently deviates from a true waverider design and allows some leakage of pressure from the lower surface to upper surface. Hence, drag is increased and aerodynamic performance of a waverider is decreased. It has been shown through studies[38, 39] that blunting decreases the heat flux experienced by a vehicle while negatively affecting its L/D. Even with this effect, a blunted waverider design will still potentially provide exceptional aerodynamic performance compared to others. The seepage of pressure can be controlled and potentially minimized through the design of the leading edge. The amount and type of blunting must be determined via a compromise between minimizing heating and maximizing aerodynamic

performance[40]. As there is a variety of configurations for a waverider, there is a variety of designs for a blunt leading edge. There are two main approaches to blunting a leading edge as shown in Figure 2.10. One approach removes material and the other adds material. Tincher and Burnett[41] suggested the addition of material will have less of an aerodynamic cost.

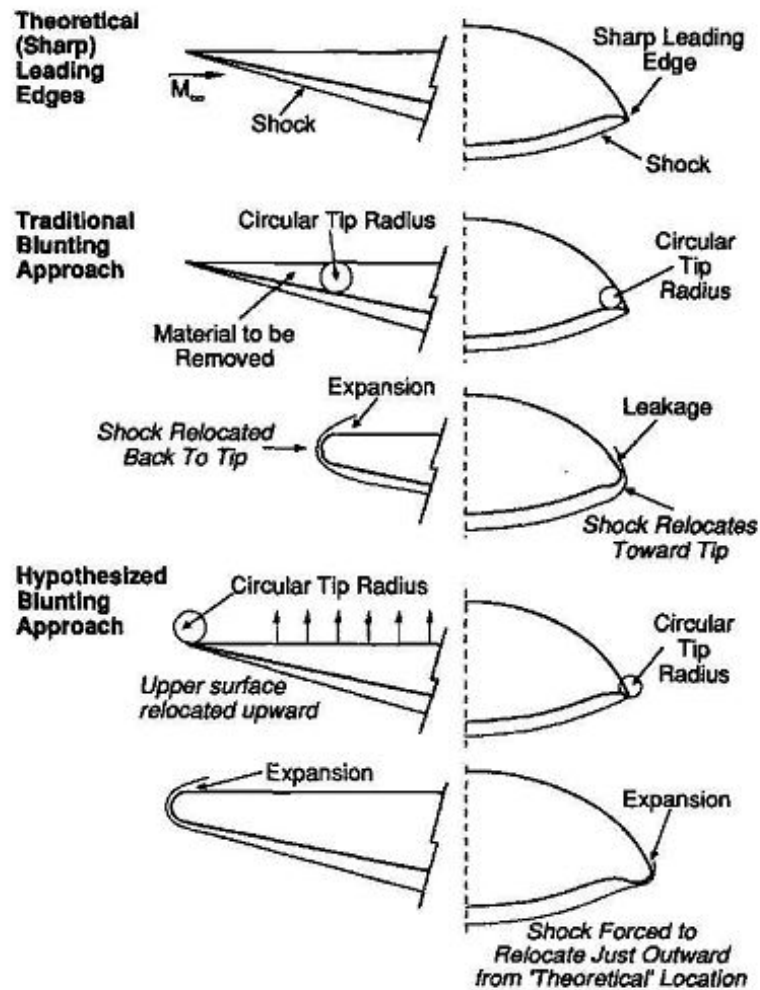


Figure 2.10. Two main blunt leading edge approaches[41]

2.3 Research of Waverider/Hypersonic Vehicle Performance

Since its inception, the waverider has been an object of study. Once a conceptual design is devised, the next step is its analysis. Aerodynamic analyses of flight vehicle configurations are obtained through various means. The typical methods are the use of engineering correlations,

flight tests, wind tunnel testing and numerical simulations. These methods are not only used for analyses but also proof of concept and building of knowledge. In the subsonic regime, each method has shown to be effective in conclusively determining performance and gaining scientific perspective. However, in hypersonics, each method has shown to have some issues in its reliability and/or implementation. Still research continues to improve upon these methods to gain knowledge for mastering the hypersonic regime.

2.3.1 Engineering database and correlations

Engineering correlation are equations and/or tables, which link physical characteristics with observed physics to produce straightforward predictive models. These relations and databases are typically formed empirically. However, the aerodynamic performance and characteristics of hypersonic waverider geometries have yet to be extensively studied or archived like that of subsonic airfoils. For instance, there exist large databases of NACA parametrically defined airfoil shapes along with their associated performance characteristics. This database started in the 1950s is still widely used in subsonic aircraft designs to date. With the advent of computational capabilities, the database has been compiled into easy to use software where a user can request an airfoil shape with a particular performance and geometric characteristic. Comparable readily available waverider geometric definition accompanied with its aerodynamic performance would be valuable in hypersonic vehicle design initiatives. Moreover, a flexible software design tool with rapid reliable analysis will serve invaluable. Efforts in section 2.2.2 are examples of steps that have been taken towards this end. Others[42] have made progress towards enhancing the analysis for the expected environment of waveriders. The design methodology of a viscous waverider, where design and analysis are coupled, can naturally lead to a tool with such capabilities.

In the mid-1950s and 1960s, a variety of critical aerothermodynamics problems associated with atmospheric reentry vehicles and related hypersonic systems were identified. One problem in particular was high-speed compressible flow over a flat plate. The efforts to solve and understand this problem lead to many experiments and engineering correlations to determine viscous surface information [43-49]. In Bowcutt's construction of a viscous waverider, empirical relations and theory for compressible flow over a flat plate were relied upon to obtain preliminary local skin friction and heating information on a waverider's surface. This was achieved by treating the streamline as a flat plate and using the flow field properties along said streamline as the conditions at the edge of a corresponding boundary layer. This leads to the empirical analysis of waverider configurations. However, the theoretical performance acquired from this preliminary analysis approach must be validated. There are two main means of validation, experimental and numerical study.

2.3.2 Experimental studies

Experimental validation in the hypersonic regime is very expensive and complex. There are two main forms of experimental testing aerodynamicists use, flight test and wind tunnel testing. In either case, the hypersonic experimental environment is short lived and there are high levels of complication and cost with instrumentation and manufacturing of models. Nonetheless, both methods are relied upon for proof of concept and fundamental research initiatives. In the subsonic regime, wind tunnel and flight test may have very close agreement but the same is not guaranteed in the hypersonic regime. The nature and reality of hypersonic flight as experienced at various levels of the atmosphere is practically impossible to replicate in a wind tunnel setting. Flight test give results that are more beneficial for the hypersonic community. Nonetheless, wind tunnel studies have been used to support waverider studies [50-54].

Despite the aforementioned technical issues that are currently adversely impacting the development of waverider derived hypersonic vehicle configurations, there are several examples of waverider vehicles that have been built for research purposes. Since the waverider design is highly dependent upon a particular flight condition, the geometry's performance envelop appears singular. However, experimental studies such as LOFlyte[55], which studied a waverider's aerodynamic performance in the subsonic regime, have shown a waverider's off design performance is also worthwhile. Other programs that aimed to collect additional knowledge of hypersonics and waverider performance in earth's atmosphere are HiFIRE and SOAREX. There is a considerable amount of encouraging research that indicate a hypersonic vehicle based upon waverider design techniques is a viable option for the next generation of aerospace and inter-continental vehicles.

Therefore, the previously discussed waverider design database tool has a purpose. However, the task of building such a database is not as straightforward as subsonic airfoils. Waveriders are three-dimensional geometries based on a plethora of variables. In contrast, airfoil shapes are two-dimensional geometries based on a small group of variables. In addition, the NACA database of airfoil performance was built using experimental results from wind tunnel tests. Flight or wind tunnel testing of a variety of waverider geometries will be very costly. Three-dimensional printing technology may ease the manufacturing process but testing can only yield but so much data. The use of today's computational capabilities via Computational Fluid Dynamics (CFD) will be a more feasible approach for building a knowledge database for waverider geometries and conducting multiple studies of validation.

2.3.3 Numerical simulation

In general, CFD has come to play a vital role in the design process. Although, CFD studies in the hypersonic regime involve its own complexities and reliability issues[56], it is less timely, costly and as effective in acquiring information of interest to researchers and designers. CFD is a three-step process of pre-processing, processing and post-processing. Pre-processing includes grid generation with defining initial and boundary conditions. Processing is the implementation of numerical methods and algorithms, which model physics of reality and usually solve Navier-Stokes equations in part or in full within the grid domain. Post-processing is the visualization of the result which usually entails a large amount of data. There are commercial and non-commercial tools that are available to assist in the execution of each step.

Grid generation is the representation of the fluid domain using a cloud of nodal points and their connectivity. Grid generation is arguably the most time consuming and frustrating part of the CFD process. However, for hypersonic studies it is even more crucial to have a high quality grid in order to capture true heat flux, boundary layer flow and shock placement. Grid features such as topology, type, orthogonality and density are factors of grid quality[1]. There are two main types of grids, structured and unstructured. Structured grids are known to be more reliable in capturing heat flux and derivatives but are difficult to implement on complex geometries. Unstructured grids are much easier to implement but may yield less accurate solutions in hypersonic studies and produce a larger load on researcher to determine heat flux and derivatives.

In processing, the solver implements a model onto the domain. The quality of the solution is reliant upon the grid but the realism of the solution depends on the physics modeled by the solver. There is an array of options which can be modeled by a solver namely; Euler, Viscous, Turbulent, Direct Numerical Simulation (DNS), Reynolds Averaged Navier-Stokes(RANS),

Large Eddy Simulation (LES) and more. In addition, with each model type, there are a number of algorithms and numerical techniques housed in various software packages. Therefore, one has a multitude of options of solver codes from research, commercial to non-commercial. The selection of the solver code is based upon a number of factors such as accessibility, computational load, level of physics desired, etc... Solvers, which model higher level of physics, may require more inputs from the user other than the pre-processing outputs. Higher level of physics gives a solution that would be considered closer to reality. However, realism calls for larger computational resources that translate to more time and higher cost as illustrated in Figure 2.11. When resources are limited, the user must choose the level of physics, which can closely replicate the anticipated environment in a cost effective and timely manner.

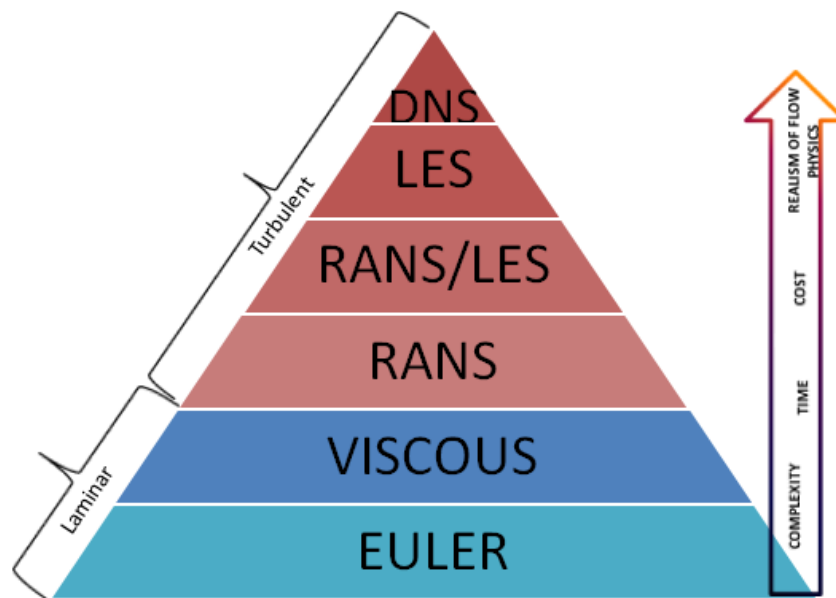


Figure 2.11. Hierarchy of CFD solvers

For hypersonic studies it is important for analysis purposes to determine the environment in which a vehicle will operate, in order to appropriately choose a solver. The most appropriate environment for a waverider derived hypersonic vehicle is shown in Figure 2.12 as the region for

hypersonic boost glide vehicle. Since, density decreases as altitude increases the aerodynamic effects such as lift and heating decrease as well. The corridor represents the heating and aerodynamic performance compromise reached through research.

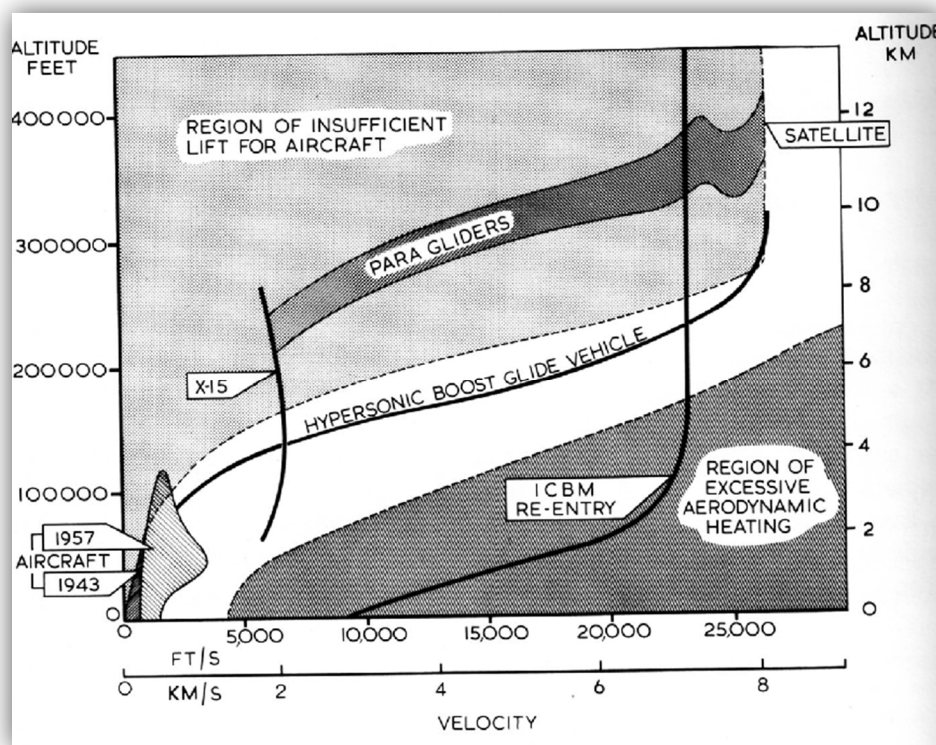


Figure 2.12. Flight corridor for aircrafts and aerospace vehicles[57]

Furthermore, at extremely high altitudes the atmosphere is essentially ‘fading’, thus the motion of individual molecules become very important. The flow can no longer be considered as a continuum, an assumption that the Navier-Stokes Equations (NSE) are based upon. Still, a waverider aerodynamic performance is of interest in low-density environment encountered at high altitudes. In practice, direct simulation Monte Carlo (DSMC), a particle method, is employed for the region of the atmosphere where NSE are not applicable. However, particle methods call for even more computational resources than NSE solvers. Figure 2.13 shows that the atmosphere can be treated as a continuum up to 80Km. More accurately, the Knudsen number can be used to

gauge the physics model to represent an environment. Figure 2.14 illustrates how Knudsen number is used to govern the applicability of various flow equations.

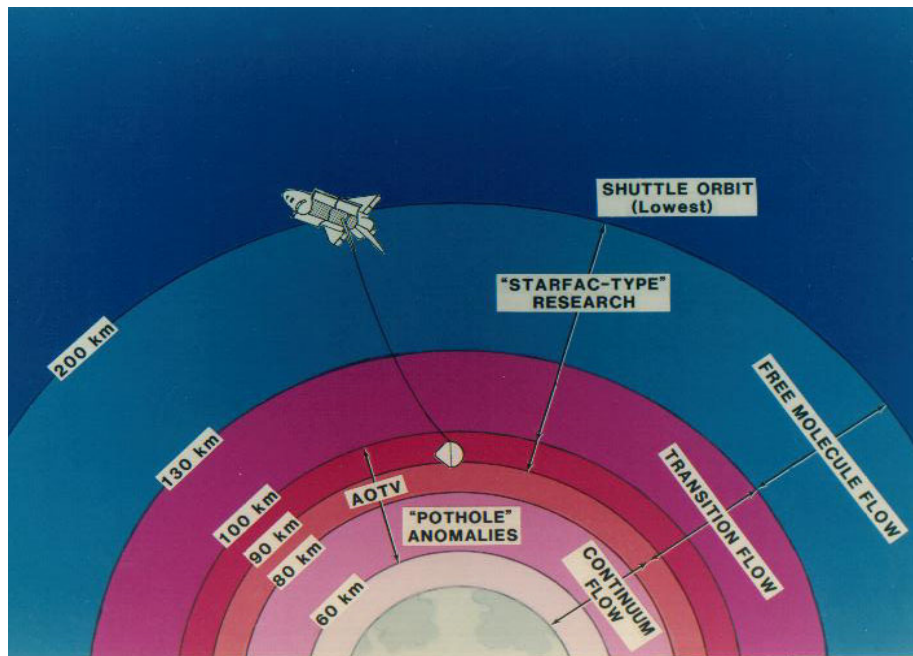


Figure 2.13. Earth atmosphere as altitude increases

The Knudsen number is the ratio of the mean distance between molecular collisions, λ , and a characteristic length, L . Today, we know that a reliable engineering relationship between the Knudsen number, Kn , vehicle length, L , Mach number, M_∞ , and Reynolds number, Re_∞ , can be expressed as follows,

$$Kn = \frac{\lambda}{L} = 1.26\sqrt{\gamma} \frac{M_\infty L}{Re_\infty \delta} \quad (2.1)$$

where the symbols, γ represents the ratio of specific heats, and δ the boundary layer thickness.

Therefore, one can determine the appropriate model for particular studies. Nonetheless, Navier-Stokes equations with viscous effects are applicable in hypersonic CFD studies for up to 80Km.

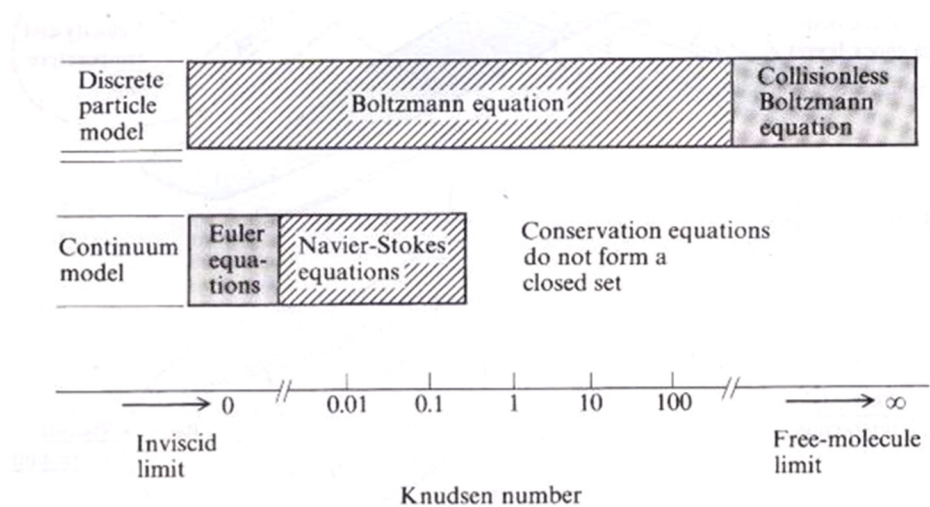


Figure 2.14. Knudsen number and applicable flow equations [7]

CHAPTER 3

DEVELOPMENT OF WAVERIDER DESIGN AND ANALYSIS TOOL

Recall the major objective of this research effort is to create a waverider based hypersonic vehicle design tool, with capability to yield practical designs, reliable preliminary analysis data, and assistance with transition to CFD studies. In efforts to achieve this objective, the following scientific methods were developed:

1. Methods for accepting users' defined inputs,
2. Methods for building post-shock inviscid flowfield from users' inputs,
3. Methods for transforming 'inviscid flow field space' to 'viscous stream surface design space',
4. Methods for extracting waverider configurations from 'viscous stream surface design space',
5. Methods for modifying waverider leading edges in response to users' defined bluntness,
6. Methods for analyzing waverider flight performance characteristics, and
7. Methods for creating and exporting CFD volume mesh to facilitate independent CFD studies,

Sections 3.2 through 3.5 detail the methods described above. All other related procedures and numerical techniques required for the efficient execution of these tasks are also documented. Also in Sections 3.2 through 3.5, where appropriate, carefully developed examples are described with the goal of highlighting the implementation and importance the newly created waverider design methods.

3.1 User Defined Inputs

The current design tool requires the users to provide appropriate technical inputs needed to construct the waverider flight envelope, its flow field, and its degree of bluntness. These inputs are waverider design Velocity, V_∞ , shock surface, waverider Length, WL, waverider nose position along x-axis, waverider base design index, waverider thermal wall conditions, q_w or T_w , and leading edge blunt radius, R_b , with blunt factor, BF. Each input's role in the design methodology for generation and analysis of a resulting waverider are described in sections 3.2 and 3.3.

There are limitations on user inputs. Inputs must not only be realistic but also within the operability of the design tool. Clearly, a user must specify a supersonic-hypersonic velocity as an input. More specifically, valid input velocities are 1.75km/s thru 8.0km/s. The tool is currently suited to build a flow field for axisymmetric and planar shock shapes. The user must provide a curve that represents a realistic shock shape, which monotonically increases or decreases. A valid shock curve should not have a local slope angle less than the minimum shock angle for the corresponding Mach number. Since Mach number is not a user input, the tool's relation of velocity with Mach number is dictated by altitude along the hypersonic glide corridor. The relation used is illustrated in Figure 3.1. Lastly, the user must be cautious when setting a position for the waverider nose. The method assumes that the shock curve meets its generating body at $x=0$. The scheme goes into runtime error when $x_{1,1}$ is on the order of 10^{-4} . From experience, computer architecture may also play a role in the limits of some input combinations causing unexpected runtime error. However, these issues are only a concern at the bounds of a realistic environment.

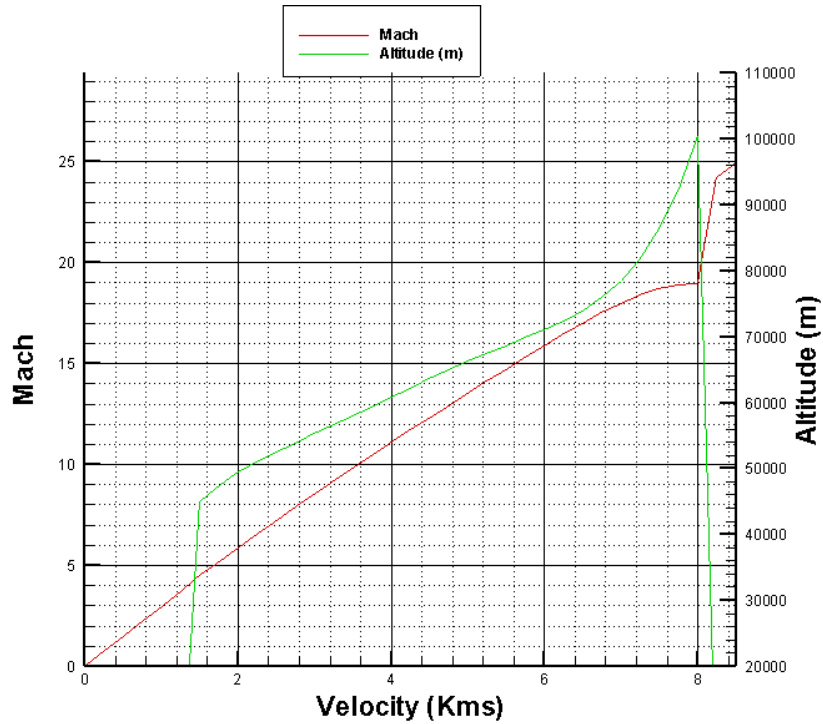


Figure 3.1. Design method operational Velocity, Mach and Altitude

3.2 Development of Design Space

As previously discussed, knowledge of a post-shock inviscid flow field is fundamental to the waverider inverse design methodology. The design tool makes use of a numerical method coined the “semi-analytical” approach for solving the Euler equations. The methodology developed by Ferguson[2] is used to generate the streamlines of a post shock supersonic inviscid flow field with known planar and axis-symmetric shock curves and pre-shock flow conditions. The hyperbolic nature of hypersonic flow makes this numerical approach reasonable. The flow generation method is computationally efficient and permits rapid parametric studies. In an effort to describe this computational method without undue complexity, a complete analysis is given of a conical flow field generated by an arbitrary axis symmetric shockwave line.

The process is described in a cylindrical coordinate frame of reference, namely, x , r and ϕ , where the x -axis is aligned with the free stream velocity vector. The flow variables are the

properties of the flow field, namely u , v , p and ρ , where u and v the cylindrical velocity components in the x and r directions respectively, ρ is the density and p the pressure.

Given flight velocity, V_∞ , the altitude is obtained using the formulated flight path of the hypersonic glide corridor, illustrated in Figure 3.2 by the solid black line and expressed as follows

$$Altitude_g = 0.0389V_\infty^5 - 0.8115V_\infty^4 + 6.5376V_\infty^3 - 25.45V_\infty^2 + 53.425V_\infty + 3.8234 \quad (3.1)$$

From the flight altitude, free stream flow properties can be calculated using Earth's Atmosphere Model[58].

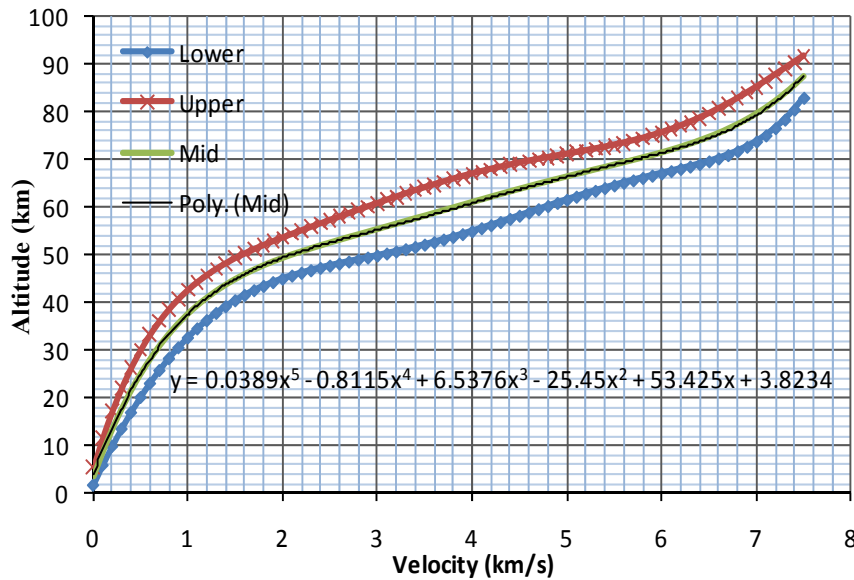


Figure 3.2. Flight corridor used by code[59]

An axis symmetric shock surface is expressed by a 2D curve discretized by N points on the xr -plane in the form of equation 3.2. The function for the curve must monotonically increase in a manner that yields a realistic shock shape. The inviscid post-shock flow field is defined by streamlines, indexed by j , starting at the shock. Each streamline is defined by a set of points, indexed by i . The $x_{1,1}$ location sets the position of the nose of the waverider as well as the beginning of the flow field construction. Therefore, the flow field for waverider construction uses a shock that starts at the desired x nose location of the waverider and extends to an x that is twice as long

as the desired length of the waverider, WL . With this information, the flow field variables immediately behind the shock can be calculated using oblique shock relations[60] with the known local Mach and shock angle (curve slope angle) the numerical process can begin. In this dissertation, the shock is defined by the relationship,

$$r_{1,j} = f(x_{1,j}), \quad x_{1,j+1} = x_{1,j} + \delta x \quad (3.2)$$

Figure 3.3 is an illustration of the numerical process. The first data line, along which the flow field information is known, is immediately after the shockwave, and can be represented by the shockwave itself for the sake of simplification. The marching scheme forms data lines that coincide with points on streamlines emanating from discretized points on shock. Therefore, data lines are also indexed as i . The independent variable, x , is defined in the interval $(x_{1,1}, x_{1,1}+2*WL)$, where $\delta x = (2*WL)/N$.

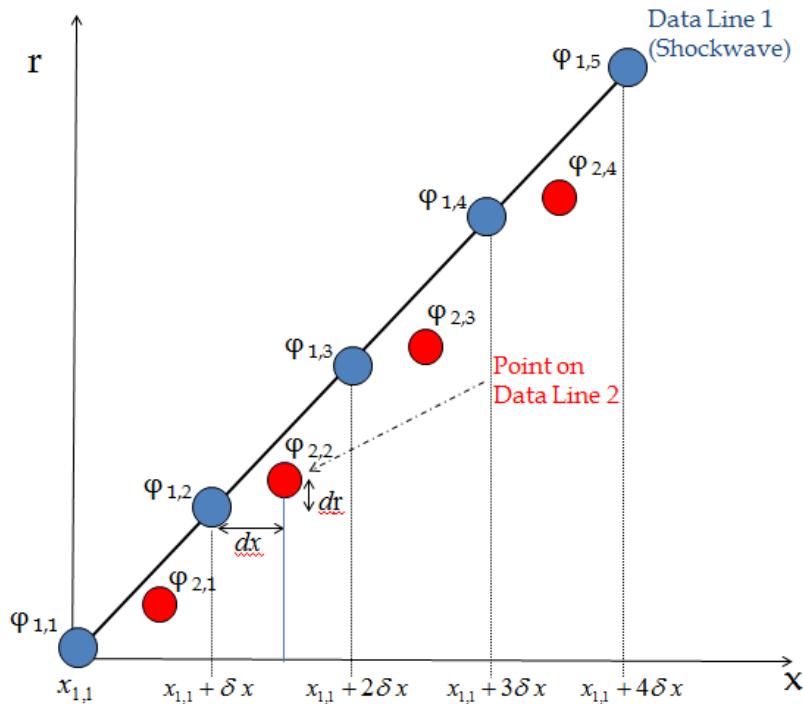


Figure 3.3. Illustration of numerical process of constructing flow field[61]

To develop a new data line, new flow field parameters: u , v , p and ρ are evaluated as per Taylor series expansion formulation in equation 3.3. The flow variables and their respective partial derivatives at each point on a given data line must be determined as follows,

$$\varphi_{i+1,j} = \varphi_{i,j} + \frac{\partial \varphi}{\partial x} dx + \frac{\partial \varphi}{\partial r} dr_{i,j} \quad (3.3)$$

where the symbol, φ , represents any flowfield property; u , v , p or ρ . The increment, dr , must be calculated at each grid point using the streamline definition,

$$dr_{i,j} = \frac{v_{i,j}}{u_{i,j}} dx \quad (3.4)$$

The partial derivatives come as result of the solution to a system of equations formed by the Euler equations coupled with directional derivatives. The axis-symmetric inviscid flowfield is governed by the conservation laws represented as the Euler Equations, which is defined as follows,

$$u \frac{\partial \rho}{\partial x} + \rho \frac{\partial u}{\partial x} + \rho \frac{\partial v}{\partial r} + v \frac{\partial \rho}{\partial r} = -\frac{\rho v}{r} \quad (3.5)$$

$$u \frac{\partial u}{\partial x} + v \frac{\partial u}{\partial r} + \frac{1}{\gamma \rho M_\infty^2} \frac{\partial \rho}{\partial x} = 0 \quad (3.6)$$

$$u \frac{\partial v}{\partial x} + v \frac{\partial v}{\partial r} + \frac{1}{\gamma \rho M_\infty^2} \frac{\partial \rho}{\partial r} = 0 \quad (3.7)$$

$$u \frac{\partial P}{\partial x} + v \frac{\partial P}{\partial r} - \frac{\gamma P u}{\rho} \frac{\partial \rho}{\partial x} - \frac{\gamma P v}{\rho} \frac{\partial \rho}{\partial r} = 0 \quad (3.8)$$

It is of interest to note that for planar flow fields the $-\frac{\rho v}{r}$ term is set to zero. Directional derivatives are formed using the chain rule expressed by

$$\frac{d\varphi_1}{dL} = \frac{\partial \varphi_1}{\partial x} \frac{dx}{dL} + \frac{\partial \varphi_1}{\partial r} \frac{dr}{dL} \quad (3.9)$$

Consider the model illustrated in Figure 3.4 along with the directional derivatives relationships defined in equations 3.10-3.13. The expressions, $\frac{d\phi_1}{dL}$, $\frac{dx}{dL}$ and $\frac{dr}{dL}$, are calculated using information from neighboring points along a given data line, as illustrated in Figure 3.4.

$$\frac{d\phi_1}{dL} = \frac{\phi_2 - \phi_1}{dL} \quad (3.10) \quad \frac{dr}{dL} = \frac{r_2 - r_1}{dL} \quad (3.11)$$

$$\frac{dx}{dL} = \frac{x_2 - x_1}{dL} \quad (3.12) \quad dL = \sqrt{(x_2 - x_1)^2 + (r_2 - r_1)^2} \quad (3.13)$$

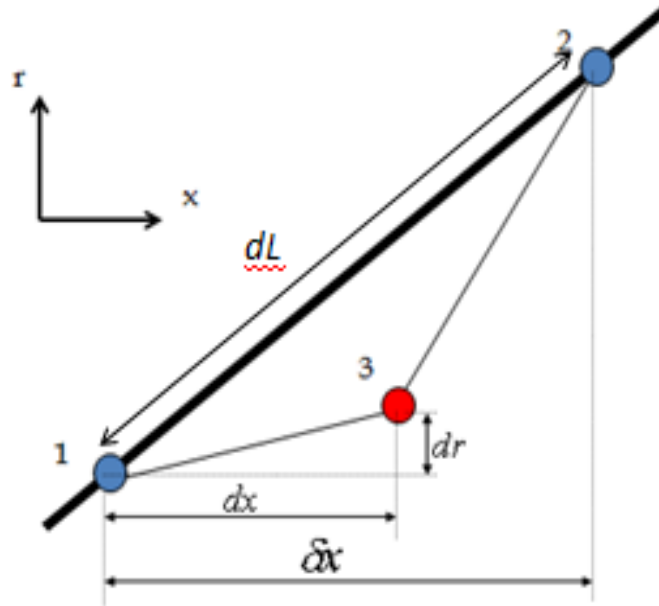


Figure 3.4. Illustration of directional derivatives

Since the directional derivatives require information from two points on the data line, it is only possible to obtain the derivatives for $j = 1, N-1$. Thus, the next data line will be one point shorter than the previous.

The coupling of the directional derivatives and Euler Equations yields a closed system of eight equations with eight unknowns, as follows:

$$\begin{pmatrix}
 \rho & 0 & 0 & \rho & u & v & 0 & 0 \\
 u & v & 0 & 0 & \frac{1}{\gamma\rho M_\infty^2} & 0 & 0 & 0 \\
 0 & 0 & u & v & 0 & \frac{1}{\gamma\rho M_\infty^2} & 0 & 0 \\
 0 & 0 & 0 & 0 & \frac{-\gamma Pu}{\rho} & \frac{-\gamma Pv}{\rho} & u & v \\
 \frac{dx}{dL} & \frac{dr}{dL} & 0 & 0 & 0 & 0 & 0 & 0 \\
 0 & 0 & \frac{dx}{dL} & \frac{dr}{dL} & 0 & 0 & 0 & 0 \\
 0 & 0 & 0 & 0 & \frac{dx}{dL} & \frac{dr}{dL} & 0 & 0 \\
 0 & 0 & 0 & 0 & 0 & 0 & \frac{dx}{dL} & \frac{dr}{dL}
 \end{pmatrix}
 \begin{pmatrix}
 \frac{\partial u}{\partial x} \\
 \frac{\partial u}{\partial r} \\
 \frac{\partial v}{\partial x} \\
 \frac{\partial v}{\partial r} \\
 \frac{\partial \rho}{\partial x} \\
 \frac{\partial \rho}{\partial r} \\
 \frac{\partial P}{\partial x} \\
 \frac{\partial P}{\partial r}
 \end{pmatrix}
 =
 \begin{pmatrix}
 -\frac{\rho v}{r} \\
 0 \\
 0 \\
 0 \\
 \frac{du}{dL} \\
 \frac{dv}{dL} \\
 \frac{d\rho}{dL} \\
 \frac{dP}{dL}
 \end{pmatrix}
 \quad (3.14)$$

Equation 3.14 is solved using Kramer's rule. Once the marching scheme is completed, streamlines are selected and truncated to form the flow field solution, ϕ . An illustration of this flow field, ϕ , is illustrated in Figure 3.5. At this stage, this flow field has all the desired characteristics from which waveriders with desirable technical requirements can be created.

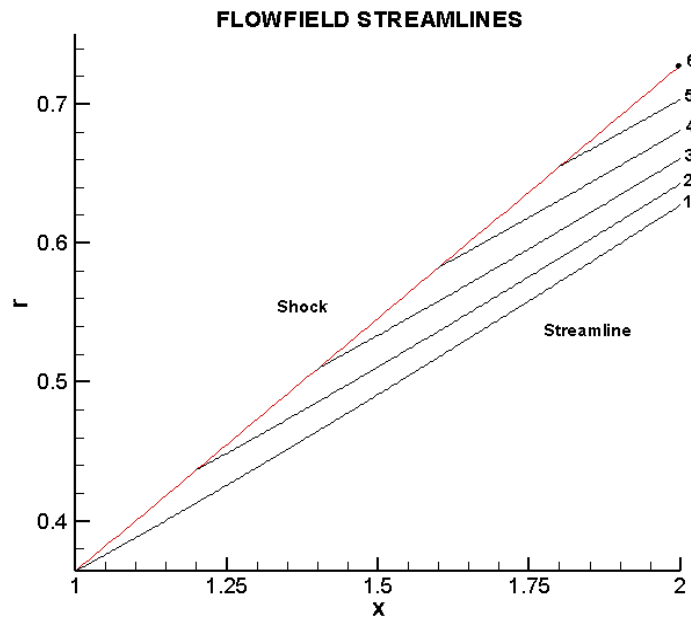


Figure 3.5. Example of prepared axisymmetric flow field plane

In this dissertation, the flow field solution, in regards to the streamlines, can be written in the form,

$$\varphi_{i,j} = SL_j(x_i, r_i, u_i, v_i, P_i, \rho_i) \quad 1 \leq j \leq N \quad 1 \leq i \leq N - j + 1 \quad (3.15)$$

where they are a maximum of N discrete streamlines, SL , and each streamline is defined by an appropriate number of discrete points.

3.2.1 Streamline to solid-line transformation

The inviscid hypersonic flow field is transformed into a viscous waverider design space by way of established engineering relations as discussed in Section 2.3.1. An ideal waverider is constructed using cross-sections formed by two independent streamlines that meet at the shock. These streamlines are used to form the upper and lower surface of waveriders. The upper surface is formed by streamlines that are parallel to the free stream and the lower surface is formed by the streamlines of the post-shock flow field. Therefore, in creating the design space, each streamline of the flow field solution is coupled with a free streamline beginning at the shock, creating design cross sections illustrated in Figure 3.6.

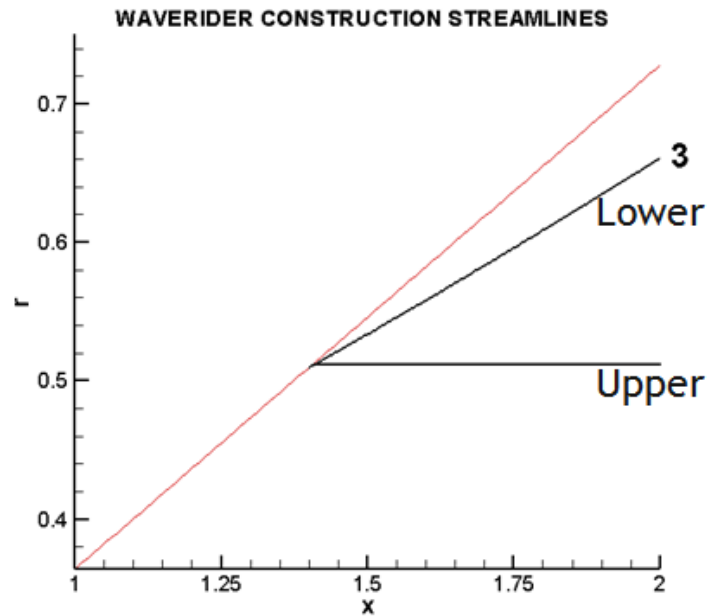


Figure 3.6. Example of waverider construction lines for upper and lower surface

Each inviscid streamline is then processed to form a solid line with viscous and blunting effects taken into account. The solid line takes the form of the corresponding streamline and its solid properties are determined. Continuing the case of an axisymmetric flow field solution, the variables along the streamline expressed in equation 3.15 are used to determine the boundary layer edge properties, velocity, V_e , pressure, P_e , temperature, T_e , and density, ρ_e . The edge velocity is simply the magnitude of velocity, the edge temperature is determined using the ideal gas relationship, edge pressure and density are equivalent to streamline values.

For the solid line, the local variables are wall pressure, P_w , heat flux, q_w , shear stress, τ_w and boundary layer height, δ . The tool archives the inviscid and viscous wall pressure, whose difference is explained in Section 3.2.1.3. Figure 3.7 illustrates the variation in definition of a streamline and solid line.

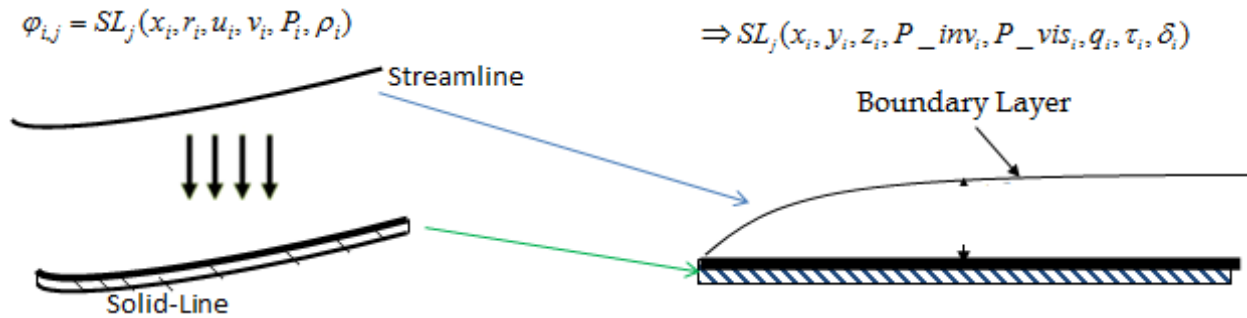


Figure 3.7. Transformation of streamline definition to solid line definition

The shear stress, τ , at each point of the inviscid streamlines is identified by

$$\tau_w = \frac{1}{2} \rho_e V_e^2 C_{f_e} \quad (3.16)$$

where C_{f_e} is the local skin friction. The local heat flux, q_w , is defined as

$$q_w = St_e \rho_e V_e (h_{aw} - h_w) \quad (3.17)$$

where St_e is the local Stanton number and enthalpy for adiabatic wall, h_{aw} , is calculated as follows

$$h_{aw} = c_p T_e + 0.5 Pr_e V_e^2 \quad (3.18)$$

The tool accounts for a laminar and turbulent region through the values of C_f and St_e . Boundary layer transition is predicted by determining transitional Reynolds number, Re_{tr} , using the correlation employed by Bowcutt[17], which is expressed as

$$\log Re_{tr} = 6.421 \exp\left(1.209 \times 10^{-4} M_e^{2.641}\right) \quad (3.19)$$

The transition point exists where the local Reynolds number Re_s , is equivalent to the transitional Reynolds number. The transition region is considered with the use of the intermittency factor, ζ_{tr} , where C_f and St_e are a concoction of their laminar and turbulent values illustrated in equation

$$(C_{fe_{tr}}, St_{e_{tr}}) = \zeta_{tr}(C_{fe_{lam}}, St_{e_{lam}}) + (1 - \zeta_{tr})(C_{fe_{turb}}, St_{e_{turb}}) \quad (3.20)$$

The end of transition is determined using the Reynolds number at the extent of transition relation given by Chen and Thyson and presented by Cebeci[62]. in the form,

$$Re_{end} = C * Re_{tr}^{\frac{2}{3}} + Re_{tr} \quad (3.21)$$

where

$$C = 60 + 4.86 M_e^{1.92} \quad (3.22)$$

The tool calculates the intermittency factor using the Cebeci correlation, which is given by

$$\zeta_{tr} = 1 - \exp\left[-\left(\frac{G}{V_e}\right)(s - s_{tr})^2\right] \quad (3.23)$$

where the beginning of transition, s_{tr} , and the variable, G , are listed as follows:

$$s_{tr} = \frac{Re_{tr} \mu_e}{\rho_e V_e}, \quad G = \left(\frac{3}{c^2}\right) \left(\frac{\rho_e}{\mu_e}\right)^2 V_e^3 Re_{tr}^{-1.34} \quad (3.24)$$

3.2.1.1 Skin friction

The skin friction coefficients are evaluated using the correlations employed by Ferguson[2]. In the case of laminar, the skin friction coefficient is evaluated as follows,

$$C_{f,Lam} = \frac{0.664}{\sqrt{\text{Re}_s}} \left(0.45 + 0.55 \frac{T_w}{T_e} + 0.09(\gamma - 1.0) M_e^2 \sqrt{\text{Pr}_e} \right)^{(\omega-1)/2} \quad (3.25)$$

where, ω is 0.75. Whereas, in the case of turbulent flows, the skin friction coefficient is evaluated as follows

$$C_{f,Turb} = \frac{0.0592}{(\text{Re}_s)^{0.2}} (1.0 + 0.5(\gamma - 1) \text{Pr}_e^{1/3} M_e^2)^{-0.55} \left(\frac{T_w}{T_e} \right)^{-0.21} \quad (3.26)$$

3.2.1.2 Stanton number

The local heat transfer rate in the laminar region is computed using the Reynolds analogy

$$St_{e,Lam} = 0.5 \text{Pr}_e^{-2/3} C_{f,eLam} \quad (3.27)$$

The local heat transfer in the turbulent region was calculated using the relationship,

$$S_{e,turb} = 0.5 \left(\frac{C_{fe,turb}}{1.0 + (8.7 \text{Pr}_e - 1.0) \sqrt{\frac{C_{fe,turb}}{2}}} \right) \quad (3.28)$$

3.2.1.3 Pressure

Recalling boundary layer theory, pressure is constant through the boundary layer normal to the surface. The pressure along the solid line can be considered equivalent to the pressure at the corresponding point on the streamline. However, close to the leading edge, where shock and surface are very close, the entropy and boundary layers merge. Consequently, higher pressures than that calculated in the flow field solution exist in this vicinity. In reality, the leading edge shock over a flat plate, whether sharp or blunt, induces high pressures that decay with downstream distance[63]. Hence, the presumed inviscid boundary edge pressure is considerably greater towards the leading edge. The wall pressure rise due to the leading edge shock and viscous interaction effects is approximated using the viscous interaction parameter, $\bar{\chi}$, defined by

$$\bar{\chi} = \frac{M_\infty}{\sqrt{Re}} \sqrt{C} \quad (3.29)$$

where,

$$C = \frac{\rho_w \mu_w}{\rho_e \mu_e} \quad (3.30)$$

The wall pressure ratio due to viscosity is a function of $\bar{\chi}$

$$\frac{P_w}{P_e} = f(\bar{\chi}) \quad (3.31)$$

Be aware there is also an influence on pressure due to blunting which is not within the scope of this work. P_e is the presumed inviscid boundary edge pressure. The tool uses the pressure relation expressed by equation 3.32.

$$\frac{P_w}{P_e} = \begin{cases} 0.514\bar{\chi} + 0.759 & \bar{\chi} > 3 \\ 1 + 0.31\bar{\chi} + 0.05\bar{\chi}^2 & \bar{\chi} < 3 \end{cases} \quad (3.32)$$

3.2.1.4 Local boundary layer height

Other useful local information attributed to the solid-line is the local boundary layer height. The boundary layer height is archived for the automated grid generation process discussed in section 3.5. The incompressible laminar local boundary layer height, δ ,

$$\delta_{\text{lam}} = \frac{5s}{\sqrt{Re_s}} \quad (3.33)$$

is used to guide the degree of clustering at the surface. However, a widely acceptable equation for hypersonic flow [64] is given as,

$$\delta = \frac{1.721s}{\sqrt{Re_s}} \left(2.397 + \frac{T_w}{T_e} + 0.193Pr^{0.5}(\gamma - 1)M_e^2 \right) \quad (3.34)$$

3.3 Waverider Construction Method

3.3.1 Ideal waverider formation

Three-dimensional ideal waverider geometries are devised by using the cross-sections formed by the solid lines of the design space. In order to create a three-dimensional configuration

a third dimension must be introduced, for an axisymmetric flow field it is the ϕ -parameter and for planar it's the z-parameter. A large class of three-dimensional shapes can be created with the appropriate set of ϕ , such that each cross-section is associated with an azimuthal plane. The shape angle, ϕ , is best defined by choosing a base plane curve in which $\phi = f(r)$ at the base plane where $x = x_{1,1} + WL$. The resulting waverider, WR, takes on the local attributes of the chosen set of solid lines. In this tool, a given waverider configuration is represented by the expression,

$$WR_j^{U,L}(x_i, y_i, z_i, P_i, \tau_i, q_i, \delta_{i,lam}, \delta_i) = SL_{\phi_j}^{U,L}(x_i, r_i, P_i, \tau_i, q_i, \delta_{i,lam}, \delta_i) \quad (3.35)$$

where

$$WR_j^{U,L}(x_i, P_i, \tau_i, q_i, \delta_{i,lam}, \delta_i) = SL_j^{U,L}(x_i, P_i, \tau_i, q_i, \delta_{i,lam}, \delta_i) \quad (3.36)$$

$$WR_j^{U,L}(y_i) = SL_j^{U,L}(r_i) * \cos \phi_j \quad (3.37)$$

$$WR_j^{U,L}(z_i) = SL_j^{U,L}(r_i) * \sin \phi_j \quad (3.38)$$

and the superscripts, U and L, represent the upper and lower surfaces. j represent the axisymmetric cross-section. Each waverider is defined by its own unique set of shape angles, ϕ . Due to the design methodology; practically any set of ϕ which increases from zero to some angle will result in a waverider configuration. However, a set of angles can be derived or determined in a number of ways. A designer can prescribe a leading edge curve, base curve or arbitrary monotonically increasing function where $\phi = f(j)$.

The tool is equipped with a design library built off the base curve approach. The advantage of using the base curve approach is that the designer has a sense of the resulting configuration. Figure 3.8 presents an illustration of the base curve approach. Here a curve is prescribed on the right side of the symmetry plane. The point where the prescribed base curve crosses the base point of a

radial cross section determines the angle of the azimuthal plane corresponding to that solid cross section.

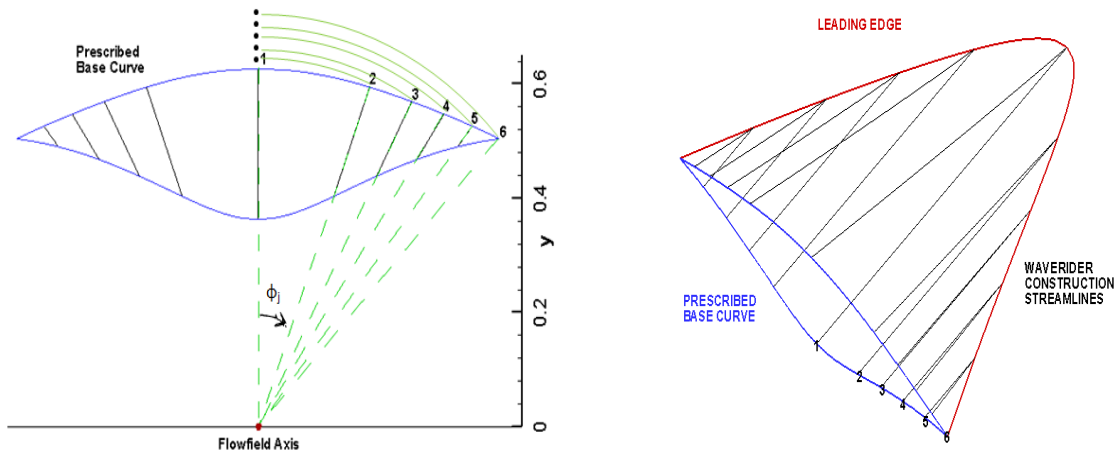


Figure 3.8. Construction of waverider from axisymmetric flow field

3.3.1.1 Use of base curve library

The library of shape angle functions has grown to more than 27 functions. It generates various configurations, by way of simply using one function or merging two or more functions to dictate span wise base curve geometry. For example, two developed waveriders, a flat top waverider and a flat bottom waverider, are offered as examples. The shape angle functions, equations 3.39 and 3.40, are used to construct the flat top waverider, shown in Figure 3.9, and the flat bottom waverider, shown in Figure 3.10:

$$\phi_j = \arccos \left(\frac{r_{N+1,1}^u}{r_{N+1,j}^u} \right) \quad (3.39)$$

$$\phi_j = \arccos \left(\frac{r_{N+1,1}^l}{r_{N+1,j}^l} \right) \quad (3.40)$$

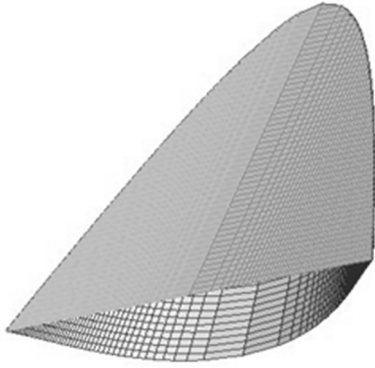


Figure 3.9. Flat top waverider

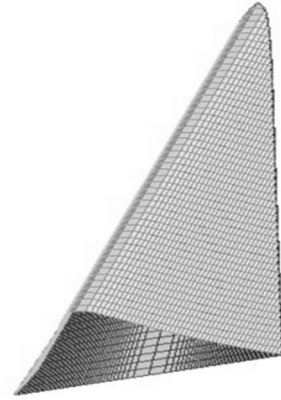


Figure 3.10. Flat bottom waverider

In a similar manner, configurations composing of desired features of the ‘flat top and flat bottom’ waveriders can also be derived as illustrated in Figure 3.11.

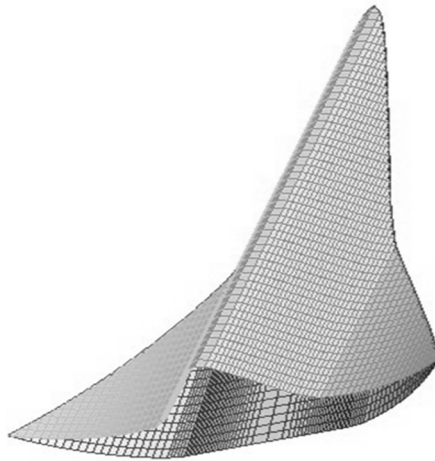


Figure 3.11. Derived waverider through merging

3.3.1.2 Parametric solid line selection function

Parametric shape angle function is a generic cross-section selection function. An example is the use of a stretching function commonly used in grid generation, where $\phi = f(j, \kappa, \phi_{\max})$. For example, a generic shape angle function is expressed as

$$\phi_j = \phi_{\max} \frac{e^{\kappa \varepsilon_j} - 1}{e^{\kappa} - 1}, \quad \varepsilon_j = \frac{j-1}{N-1} \quad \text{for } 1 \leq j \leq N \quad (3.41)$$

Many other functions can be devised in a similar manner. These types of equations can be exploited for parametric studies as well as waverider identification efforts. The use of other parametric functions like Bezier curves and splines for prescribing a base curve can determine a set of ϕ .

3.3.2 Blunt leading edge design

Waverider geometries inherently have sharp leading edges. The sharp edge produces extremely small stagnation region that leads to unmanageable thermal loads that will destroy any material/vehicle. Therefore, in order to make waverider geometries practical for surviving the hypersonic flight environment some degree of blunting must be employed.

For the waverider geometries produced by the FORTRAN tool, blunting was achieved using cubic bezier curves. The upper surface is separated from the lower by twice the desired blunt radius, illustrated by $WR^U(y) = WR^U(y) + 2R_b$. A bezier curve, defined by

$$\text{BezierCurve} = (1 - t)^3 Pt_0 + 3t(1 - t)^2 Pt_1 + 3t^2(1 - t) Pt_2 + t^3 Pt_3 \quad 0 \leq t \leq 1 \quad (3.42)$$

is produced to close the gap at each yz cross-section. The four control points for the curve were determined using the slopes and leading edge points of the surfaces. In addition, a blunt factor, BF, was introduced to control the distance at which the curve extends from the body, thereby controlling the degree of blunting. Figure 3.12 illustrates the resulting curve and the control point locations.

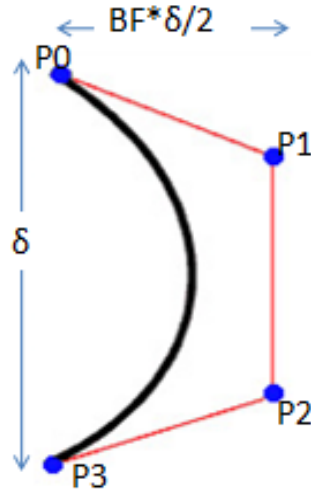


Figure 3.12. Illustration of blunting using control points

The four control points Pt_0 , Pt_1 , Pt_2 , and Pt_3 defined with (x, y, z) coordinates are determined as follows. Since, the streamlines were formulated have common x -coordinates, each yz cross-section control points share the same x -coordinate. Therefore, for all cross-sections, $x_0=x_1=x_2=x_3$. Since, the upper and lower surface endpoints coincide with the blunt curves endpoints, those coordinate values are assumed by the first and last control point. Hence, $Pt_0=WR_j^U(x_1, y_1, z_1)$ and $Pt_3=WR_j^L(x_1, y_1, z_1)$. As shown in Figure 3.12, the z -coordinates of Pt_1 and Pt_2 are represented as $Pt_1(z) = Pt_2(z) = Pt_0(z) + R_b * BF$. The y -coordinates of Pt_1 and Pt_2 are a function of the slope of the yz cross-section given by equations,

$$Pt_1(y) = Pt_0(y) + dydz_j^u * BF * R_b \quad (3.43)$$

$$Pt_2(y) = Pt_3(y) + dydz_j^l * BF * R_b \quad (3.44)$$

where

$$dydz_j^u = \frac{WR_j^u(y_1) - WR_{j-1}^u(y_2)}{WR_j^u(z_1) - WR_{j-1}^u(z_2)} \quad (3.45)$$

$$dydz_j^l = \frac{WR_j^l(y_1) - WR_{j-1}^l(y_2)}{WR_j^l(z_1) - WR_{j-1}^l(z_2)} \quad (3.46)$$

Figure 3.13 illustrates the effects of the blunt factor.

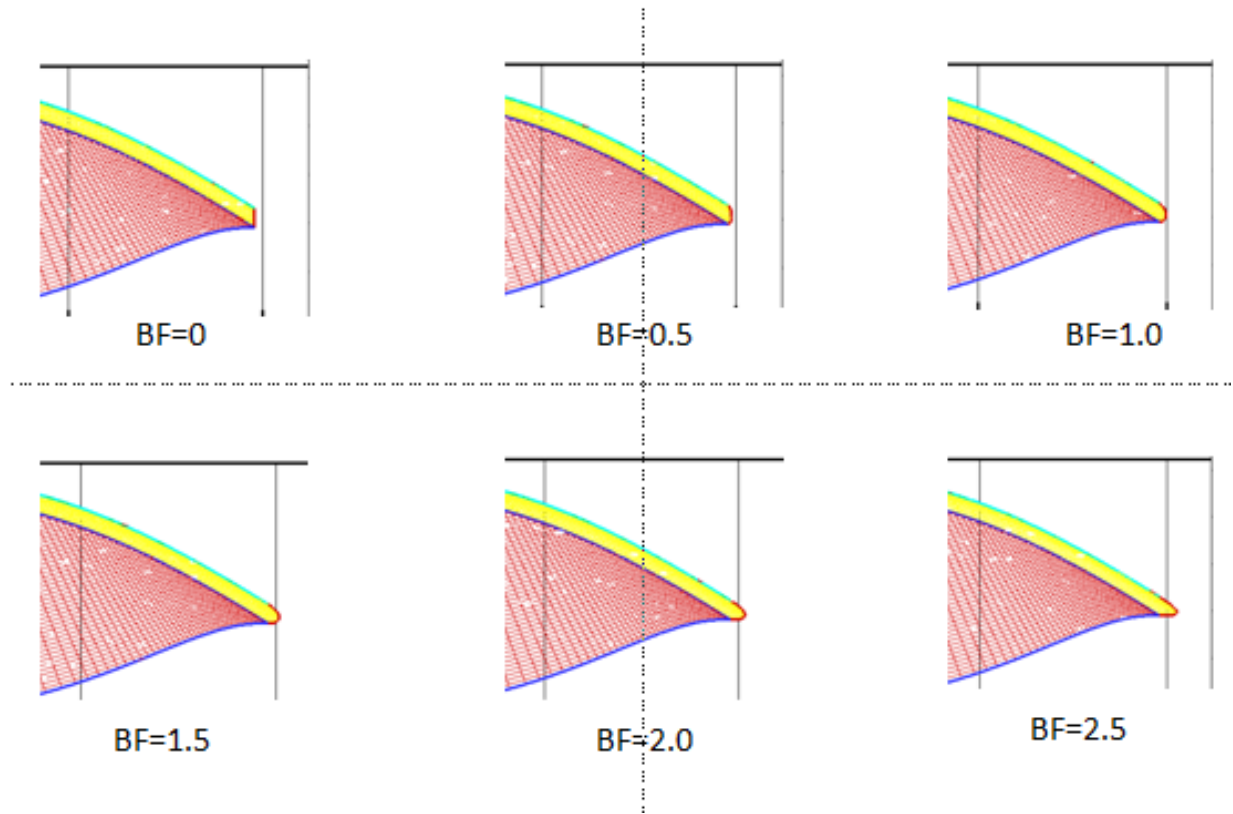


Figure 3.13. Illustration of effect of blunt factor on blunt surface

3.3.2.1 Determining solid properties of leading surface

Since the waverider solid lines house local viscous properties, any surface added to the design should also have such information. Since the blunt surface is formed without any association to a streamline or flow field, the pressure, shear, τ , and heat flux, q , are obtained through alternative means. The edge variables can take on the flow values seen along the leading edge of the waverider. However, this assumption is improper because the effects of a blunt surface in hypersonic flow are known to create a subsonic region. Therefore, the edge velocity variables would greatly differ from that of the inviscid leading edge. Pressure is determined using modified Newtonian theory. The tool determines the local shear stress across the blunt surface with a relation to heating. Heating is determined using the stagnation heat and a distribution relation. The details are as follows.

3.3.2.1.1 Pressure

The tool utilizes modified Newtonian theory, expressed by the relationship,

$$C_{p,i,j} = C_{p,\max} \frac{|V_\infty \cdot \hat{n}_{i,j}|^2}{V_\infty^2} \quad (3.47)$$

where

$$C_{p,\max} = \frac{2}{\gamma M_\infty^2} \left[\left(\frac{(\gamma + 1)^2 M_\infty^2}{4\gamma M_\infty^2 - 2(\gamma - 1)} \right)^{\gamma/\gamma-1} \left(\frac{1 - \gamma + 2\gamma M_\infty^2}{\gamma + 1} \right) - 1 \right] \quad (3.48)$$

to determine local pressure on the blunt surface. In addition, the local unit normal, $\hat{n}_{i,j}$, is determined using

$$\hat{n}_{i,j} = \frac{(Po \text{ int}_{i+1,j} - Po \text{ int}_{i-1,j}) \times (Po \text{ int}_{i,j-1} - Po \text{ int}_{i,j+1})}{|(Po \text{ int}_{i+1,j} - Po \text{ int}_{i-1,j}) \times (Po \text{ int}_{i,j-1} - Po \text{ int}_{i,j+1})|} \quad (3.49)$$

The local pressure on the blunt surface is determined using equation 3.50.

$$P_{i,j} = C_{p,i,j} * q_\infty \quad (3.50)$$

3.3.2.1.2 Heating

The heat flux distribution along the blunt surface is determined using the stagnation heating. The stagnation heat flux is considered at the mid of the blunt surface assumed to be where $t=0.5$ along the Bezier curve. The stagnation heating is determined using Fay-Riddell relationship [65],

$$q_{stag} = 0.537a \text{Pr}^{-0.6} \left[1 + \left(\frac{Dx}{Dz} \right)^{0.5} \right]^{0.5} \left(\frac{du_e}{dx} \right)_{x=0}^{0.5} \left[1 + (Le^d - 1) \frac{h_{De} - h_{Dw}}{h_e - h_w} \right] (h_r - h_w) \quad (3.51)$$

where the auxiliary symbols are defined as follows:

$$\left(\frac{du_e}{dx} \right)_{x=0} = \frac{2}{D_x} \sqrt{\frac{2(P_t - P_e)}{\rho_t}} \quad (3.52)$$

$$a = (\rho_t \mu_t)^{0.4} (\rho_w \mu_w)^{0.1} \quad (3.53)$$

The variables D_x and D_z are the principal diameters where $D_x < D_z$. $Le = 1.0$ and $d=0.52$ since disassociation is not considered. The boundary layer edge pressure is considered equivalent to the wall pressure. The local heating along the blunt surface was estimated via interpolation between the stagnation and upper/lower heating points, shown in Figure 3.14. The interpolation procedure used the Fay-Riddell equation with the local edge properties approximated using the interpolation expression,

$$Property_e = \frac{x^p}{D^p} (Property_{wL,wU}) + \left(1.0 - \frac{x^p}{D^p}\right) Property_{stag,e} \quad (3.54)$$

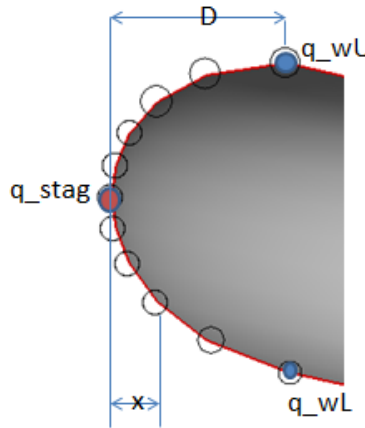


Figure 3.14. Illustration of heat interpolation procedure

3.3.2.1.3 Skin friction

Skin friction across the blunt surface is also approximated via interpolation between the stagnation point and the upper and lower surfaces. The skin friction coefficient at the stagnation point is zero and increases to its maximum value at the point where the lower and upper surfaces meet the blunted surface. It is assumed to increase in a trend similar to the y-component of the normal vector along the blunt surface. Therefore, in this case, the interpolation relationship is not necessarily linear, but rather, expressed with the relationship,

$$C_{f_{pt}} = \frac{ny_{pt}}{ny_{L,U}} C_{f_{L,U}} \quad (3.55)$$

3.3.3 Generic stream-surface construction

In addition to blunt surfaces, generalized stream surfaces may be carved from the existing flow field and used as auxiliary surfaces that may serve as engine components or control surfaces. A generic stream-surface is not restricted to the rules of a waverider stream-surface, in that it does not have to meet the shock. It may be formed by any set of neighboring solid-lines. Its design space is the remaining solid lines of the post shock flow field as well as the free-stream flow above the upper surface. Auxiliary stream-surfaces can be formed in ways similar to that of waverider surfaces, with a base curve definition or a generalized function. The freedom of the formation of a generic stream-surface allows for a completely streamlined hypersonic vehicle with integrated components. The integrated resulting waverider with solid stream-surface body represents a higher order of waverider configurations. For illustrative purposes, Figure 3.15 shows an auxiliary stream-surface, serving as an engine component, attached to the waverider. This example serves as a simple demonstration of a potential design process for constructing an entire vehicle using the waverider design technique.

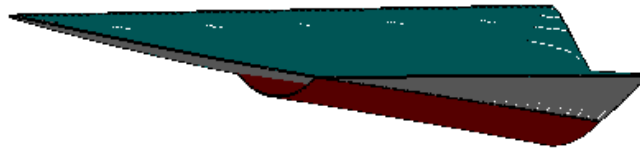


Figure 3.15. Waverider with attached stream-surface duct

3.4 Waverider Analysis

With a complete configuration and local surface properties known for all viscous surfaces of the design, a complete analysis can be performed. The analysis determines the global

characteristics of the resulting waverider configurations. The characteristics of a waverider design can be placed in two categories, geometric and aerodynamic. The geometric analysis is used to determine volumes, surface area, lengths and widths. Global aerodynamic analysis determines characteristics such as lift, drag, and aerodynamic coefficients. This section illustrates the methodologies used to perform such analysis.

3.4.1 Geometric analysis

The geometric characteristics such as area and volume are determined by utilizing the coordinates, which define the waverider's surfaces. In this analysis, the triangular method is used to calculate all elementary areas of interests. The areas of interest include the total wetted area, the base area and the plan form area. The triangular method considers each surface as a set of triangles. The upper, lower, blunt surfaces and arbitrary stream surfaces are treated separately. In this analysis, all elementary surfaces are first described by quads, and later divided into elementary triangular surfaces, except for the leading edge region, where the elementary surfaces are described directly by triangles. Refer to Figure 3.16 that highlights this concept. Similarly, refer to Figure 3.17.

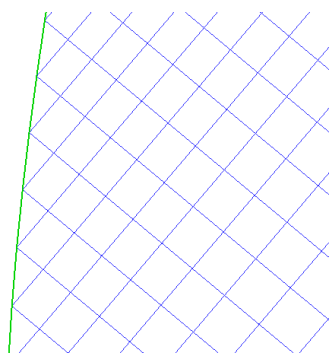


Figure 3.16. Example of elements on upper/lower surface

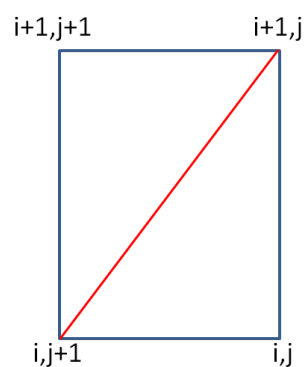


Figure 3.17. Illustration of treatment of quad elements in triangular method

The area of all elementary triangles, including the projected areas, is calculated based on Heron's formulation. For instance, the areas of the elemental surface triangle ABC, Figure 3.18, are found using Heron's formula. Total base and plan form areas are acquired in a similar manner using the elemental projected areas of surface triangles also illustrated in Figure 3.18. Base area use the projected area, dS_x , on yz-plane and planform area use projected area, dS_y , on xz-plane.

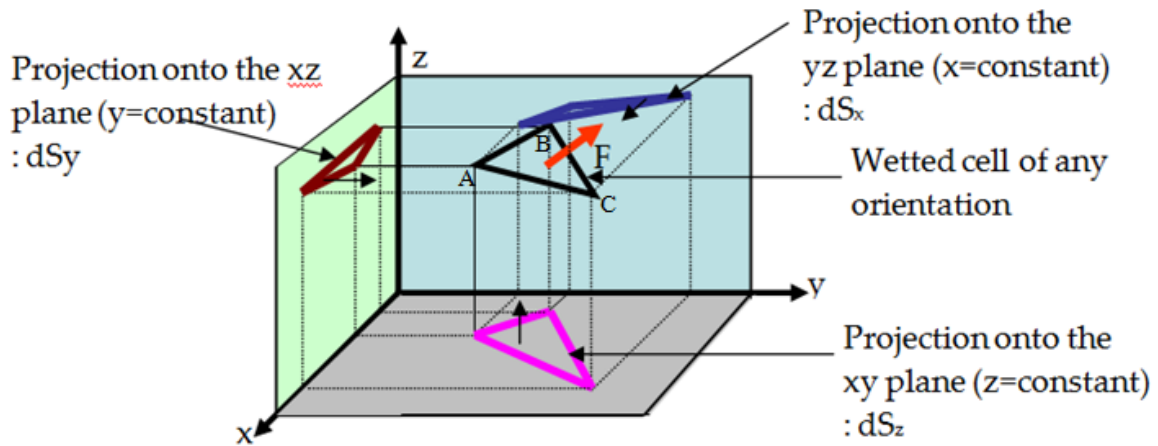


Figure 3.18. Arbitrary elemental triangle ABC and its projections

Heron's formula employs the lengths of the sides of triangle,

$$\begin{aligned}
 AB &= \left\{ \lambda_x (X_A - X_B)^2 + \lambda_y (Y_A - Y_B)^2 + \lambda_z (Z_A - Z_B)^2 \right\}^{0.5} \\
 AC &= \left\{ \lambda_x (X_A - X_C)^2 + \lambda_y (Y_A - Y_C)^2 + \lambda_z (Z_A - Z_C)^2 \right\}^{0.5} \\
 BC &= \left\{ \lambda_x (X_B - X_C)^2 + \lambda_y (Y_B - Y_C)^2 + \lambda_z (Z_B - Z_C)^2 \right\}^{0.5}
 \end{aligned} \tag{3.56}$$

where λ_m equals 1, or 0 if the projection is in the m direction. It is of interest to note that the m^{th} direction represent the x, y or z normal. The evaluated lengths of the respective sides of a given triangle are then used to compute the area, as follows:

$$\begin{aligned}
 t &= (AB + BC + AC)/2 \\
 A_{\text{element}} &= (t * (t - AB) * (t - BC) * (t - AC))^{0.5}
 \end{aligned} \tag{3.57}$$

Finally, the surface areas are simply the summation of elemental areas of interests as expressed by

$$S_m = \sum \sum A_{element} \quad (3.58)$$

In addition to planform, side, base, and wetted areas, this tool can provide the user with the amount of wetted area contributed by waverider upper, lower, blunt surface or generic stream surface.

3.4.1.1 Volume

The volume of the waverider consists of irregular elemental triangular prisms formed by two corresponding elemental triangles ABC and DEF, as illustrated in Figure 3.19. The volumes of the cells are calculated using equation,

$$V_{element} = avg(ABC_{Area}, DEF_{Area}) * avg(\overline{AD}, \overline{BE}, \overline{CF}) \quad (3.59)$$

The total volume of the waverider is the sum of two main volumes, which are the volume of the ideal waverider and the additional volume created by the blunting process. The volume of the ideal waverider uses the corresponding triangles of the upper and lower surfaces. The volume from blunting is equivalent to the waverider planform area times the displacement of the upper surface plus the volume using the corresponding triangles of the blunted region.

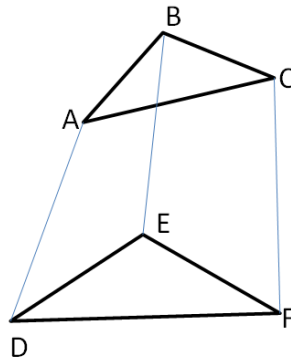


Figure 3.19. Elemental irregular triangular prism

3.4.2 Aerodynamic analysis

Waverider aerodynamic analysis is performed through the integration and processing of the local surface information. The aerodynamic force, \vec{F} , is a global characteristic of the

waverider configuration. The evaluation of the aerodynamic force on a given waverider configuration involves the evaluation of the following expressions as they are applied to the upper, lower and blunt waverider surfaces.

$$\vec{F} = \vec{F}_p + \vec{F}_\tau \quad (3.60)$$

where F_p is the force resulting from pressure and \vec{F}_τ is the force resulting from shear stress. The aerodynamic force can also be expressed into its three general constituent components shown in equation,

$$\vec{F} = D\vec{i} + L\vec{j} + G\vec{k} \quad (3.61)$$

where D , L and G , are the drag, lift and slip forces respectively. Furthermore, the contributions from the pressure and viscous forces to the constituent forces may be resolved as shown in equation set,

$$\begin{aligned} \vec{F}_p &= \iint_S p d\vec{S} = p_{avg} \iint_S d\vec{S} = p_{avg} \iint_S (dS_x \vec{i} + dS_y \vec{j} + dS_z \vec{k}) \\ \vec{F}_\tau &= \iint_S \tau d\vec{S} = \tau_{avg} \iint_S d\vec{S} = \tau_{avg} \iint_S (dS_x \vec{i} + dS_y \vec{j} + dS_z \vec{k}) \end{aligned} \quad (3.62)$$

The average pressure and shear are determined on each surface as follows. The average pressure is simply calculated as:

$$P_{avg} = \frac{\sum_i \sum_j P_{i,j}}{\text{Number_of_Surface_Points}} \quad (3.63)$$

In order to calculate the average shear stress, a triangular element is once again used. First, the average force due to shear stress on each element is calculated in the following manner:

$$f_{avg}^{element} = \frac{(\tau_A + \tau_B + \tau_C)}{3} * A_{element} \quad (3.64)$$

Then, the average shear stress is determined as follows.

$$\tau_{avg} = \frac{\sum \sum f_{avg}^{element}}{Total\ wetted\ area} \quad (3.65)$$

Keeping in mind that the lift is the j component, the Drag the i component, and Side Force the k component, these forces are evaluated as

$$\begin{aligned} L &= P_{avg} A_{Plan} - \tau_{avg} A_{Base} \\ D &= P_{avg} A_{Base} + \tau_{avg} A_{Plan} \end{aligned} \quad (3.66)$$

where A_{Plan} is the plan form area, A_{Base} is the base area. The side force is neglected due to the symmetry of the waverider. Other aerodynamic properties like the coefficients of lift and drag are found as follows:

$$\begin{aligned} C_L &= \frac{L}{q_{\infty} A_{Plan}} \\ C_D &= \frac{D}{q_{\infty} A_{Plan}} \end{aligned} \quad (3.67)$$

3.5 Automated Grid Generation Methodology

With a completed geometry, as previously stated, a method for automated grid generation was developed to conduct CFD studies. As mentioned in Chapter 2, there is a great demand to produce quality grids for hypersonic flow compared to most other flow studies. Some current solvers call for cell clustering and alignment of cell faces towards the shock and waverider surface. The waverider design methodology presented provides the advantage of knowing the approximate vicinity and shape of the shock as well as the approximate boundary layer height across the surface. This information is used in meeting grid quality demands in a timely automated grid generation process.

The most critical aspect of the grid generation process is the construction of the surface mesh. Structured cells redefine the waverider surface in two zones, the body and nose. The surface mesh was formulated using spline routines obtained from Ref. [66] to redefining the waverider geometry

without changing its original shape. In addition, user-defined inputs maybe implemented to garner numerical clustering controls of the waverider defining coordinates. Due to the numerical noise in using splines, the nodes of the surface mesh were determined in a piecemeal manner for the upper, lower and blunt portion of the waverider surface. Even though, this approach led to issues of controlling the spacing between the nodes at the junction of surfaces, it relieved the discrepancies formed by the initial use of splines.

Once the surface mesh was completed, the volume mesh was constructed with the use of local surface information such as the surface unit-normal, boundary layer height, approximate shock surface, shock unit normal, and Bezier curves. The control points of the Bezier curves were determined such that a grid has orthogonality at the surfaces of the waverider. A mesh was formed for the shock surface having a similar distribution of points as the waverider surface. This was done in order to prevent the occurrence of folded faces during the grid generation process. The shock surface was determined with the original shock offset by sum of the standoff distance and boundary layer height at the corresponding point on the waverider surface. The corresponding points of the two meshes were then connected using Bezier curves and their unit norms. Therefore, the control points of the Bezier curves were defined as follows.

$$Pt_0 = WR_{Pt} \quad (3.68)$$

$$Pt_1 = WR_{Pt} + 1.6 * \delta_{Pt} * WR_{\hat{n}} \quad (3.69)$$

$$Pt_2 = Shock_{Pt} - 0.5 * (standoff + \delta_{Pt}) * Shock_{\hat{n}} \quad (3.70)$$

$$Pt_3 = Shock_{Pt} \quad (3.71)$$

The volume mesh is completed by building out the resulting mesh from the shock to a corresponding far field mesh. The computational grid produced by the automated method is

exported as a Plot3d file for portability into CFD solvers and other grid manipulation tools. Some examples of the waverider computational grids are displayed in Figures 3.20 thru 3.24.

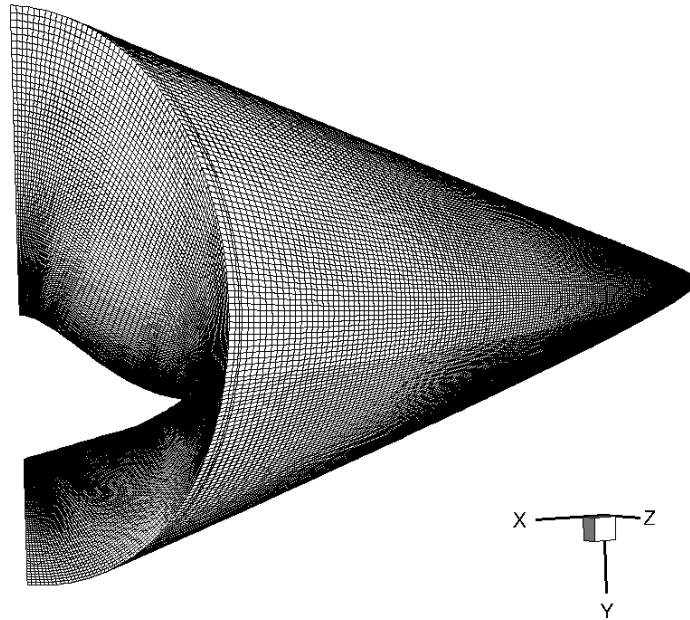


Figure 3.20. Example of a full volume mesh

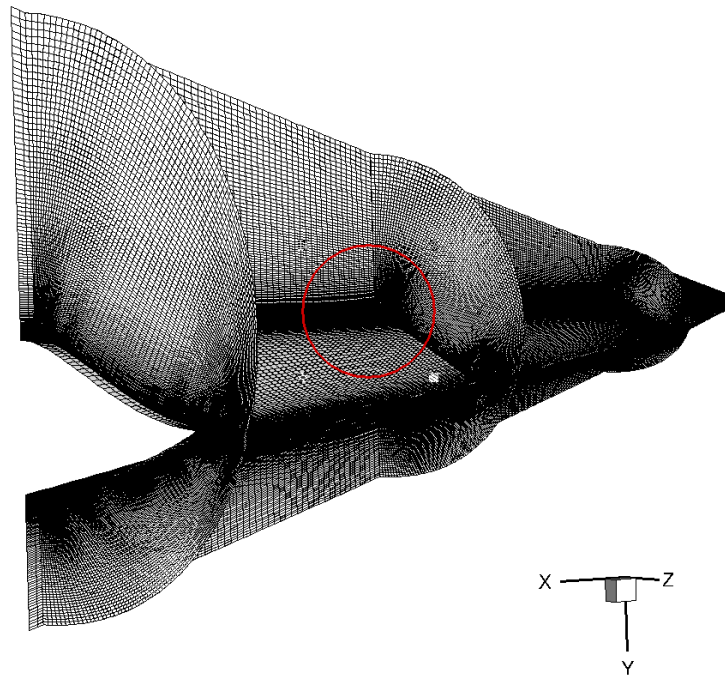


Figure 3.21. Isolated surfaces of mesh

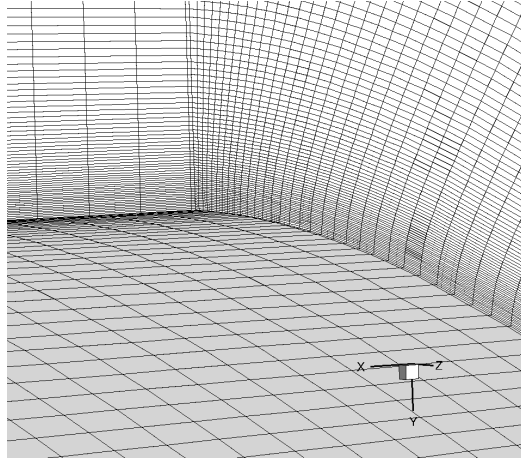


Figure 3.22. Zoom view into orthogonality at surface

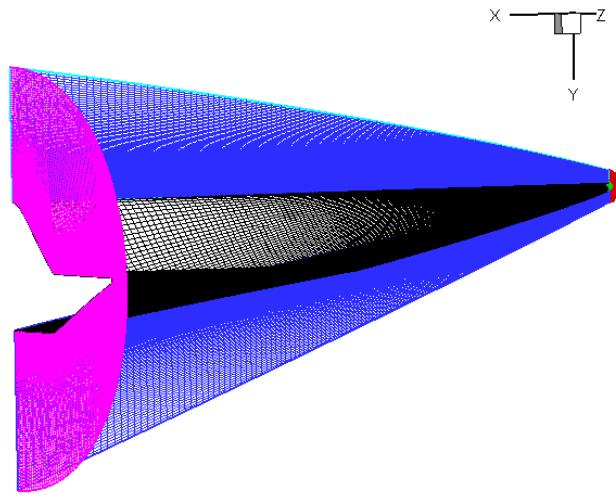


Figure 3.23. Volume mesh with zone 1 (blue) and zone 2 (red) highlighted

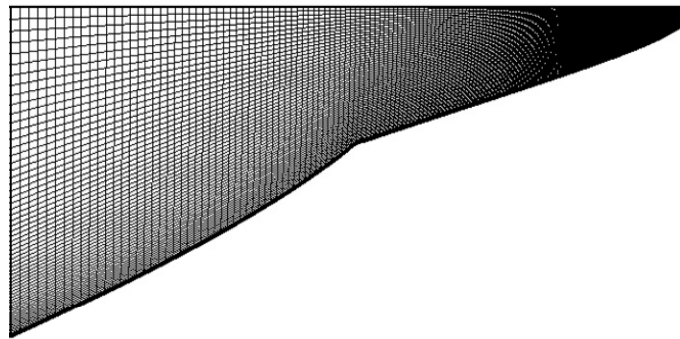


Figure 3.24. Illustration of surface mesh

CHAPTER 4

VALIDATION AND COMPARATIVE STUDIES

The results obtained from the implementation of the waverider design methodology presented in Chapter 3 are compared to existing analytical, experimental and numerical data to determine their validity. Recall, the inverse design process consists of several important technical methods, such as, the generation of an inviscid flow field, the transformation of inviscid streamlines to solid viscous streamlines, the creation of a flexible waverider design space, the construction of waveriders, and the analysis of waverider configurations. Section 4.1 of this Chapter describes the validation of each method, and justifies the implementation and legitimacy of the design and analysis approach developed herein. Further, section 4.2 compares the results obtained from the use of this tool to that of independent and credible CFD solutions.

4.1 Validation of Tool Features

4.1.1 Flow field generation validation

The solution obtained from the marching scheme described in Section 3.2 is compared to the Taylor-Maccoll analytical solution for supersonic conical flow fields solved by a Matlab code[67]. Recall, the Taylor-Maccoll procedure transforms the Euler equations in spherical coordinates into a single ordinary differential equation that is solved using the Runge-Kutta scheme. It is of interest to note that the Taylor-Maccoll solution generates the flow properties, ρ , u , v and p , as functions of the angle, θ , which is measured between the generating cone angle and the shockwave angle. On the other hand, the solution generated by the presented marching scheme method provides the flow properties, ρ , u , v and p , along streamlines. Refer to Figure 4.1.

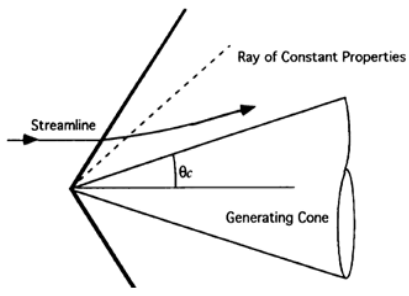


Figure 4.1. Illustration of radial angle and streamline perspectives

Through transformation, the streamline solution is converted to a radial solution for comparison. A grid independent test was conducted using the marching scheme, in which the number of points along a given shock was increased from 101 to 201 to 401, thus increasing the points on a resulting streamline. The study shows only slight variations in the solution accuracy. Refer to Figure 4.2.

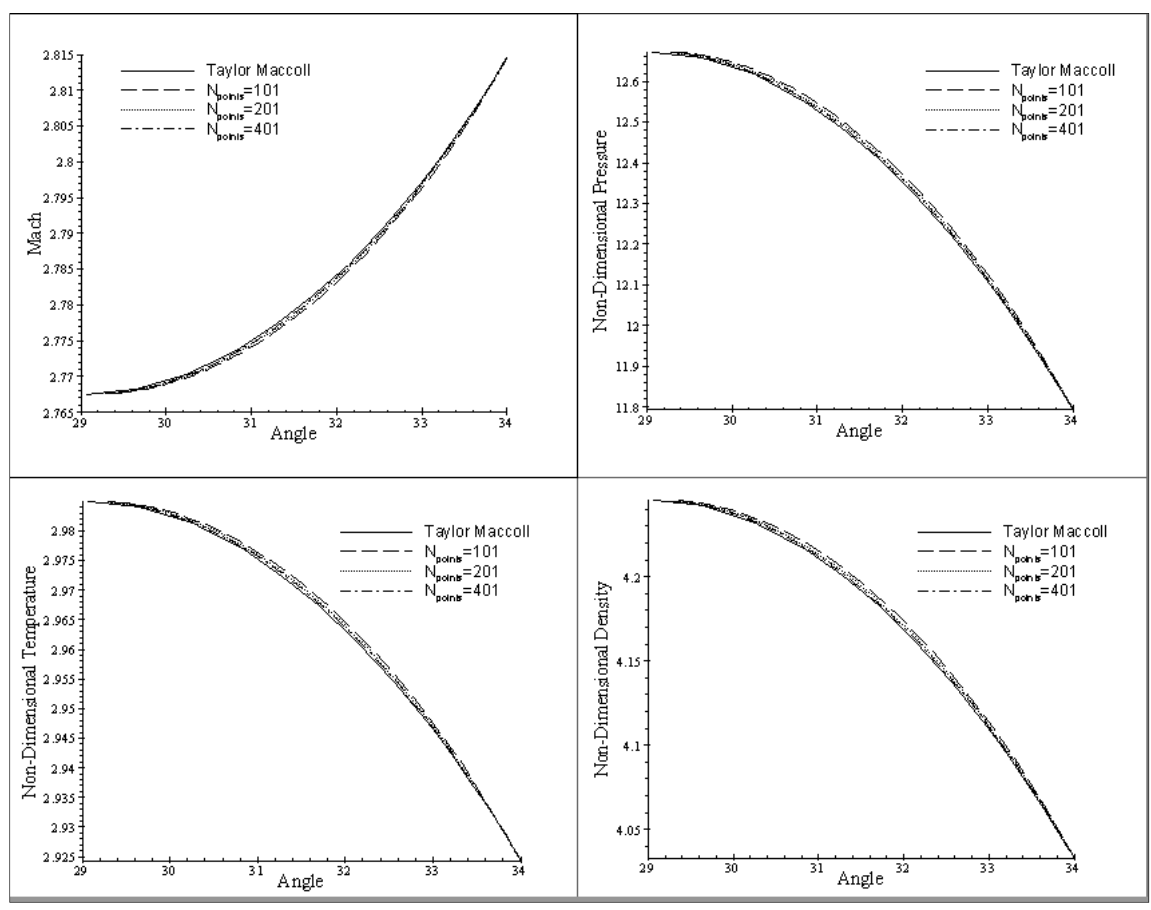


Figure 4.2. Comparison of semi analytical and Taylor-Maccoll solutions

The grid independence test was performed for a flight velocity of 1.95km/s and a half cone angle of 34° . It is of interest to observe that the accuracy of the marching scheme increases with a finer shock, but still the coarsely defined shock solution is numerically acceptable as well. A similar validation test is presented using multiple streamlines from the same flow field solution. Figure 4.3 shows that each streamline is true to the solution.

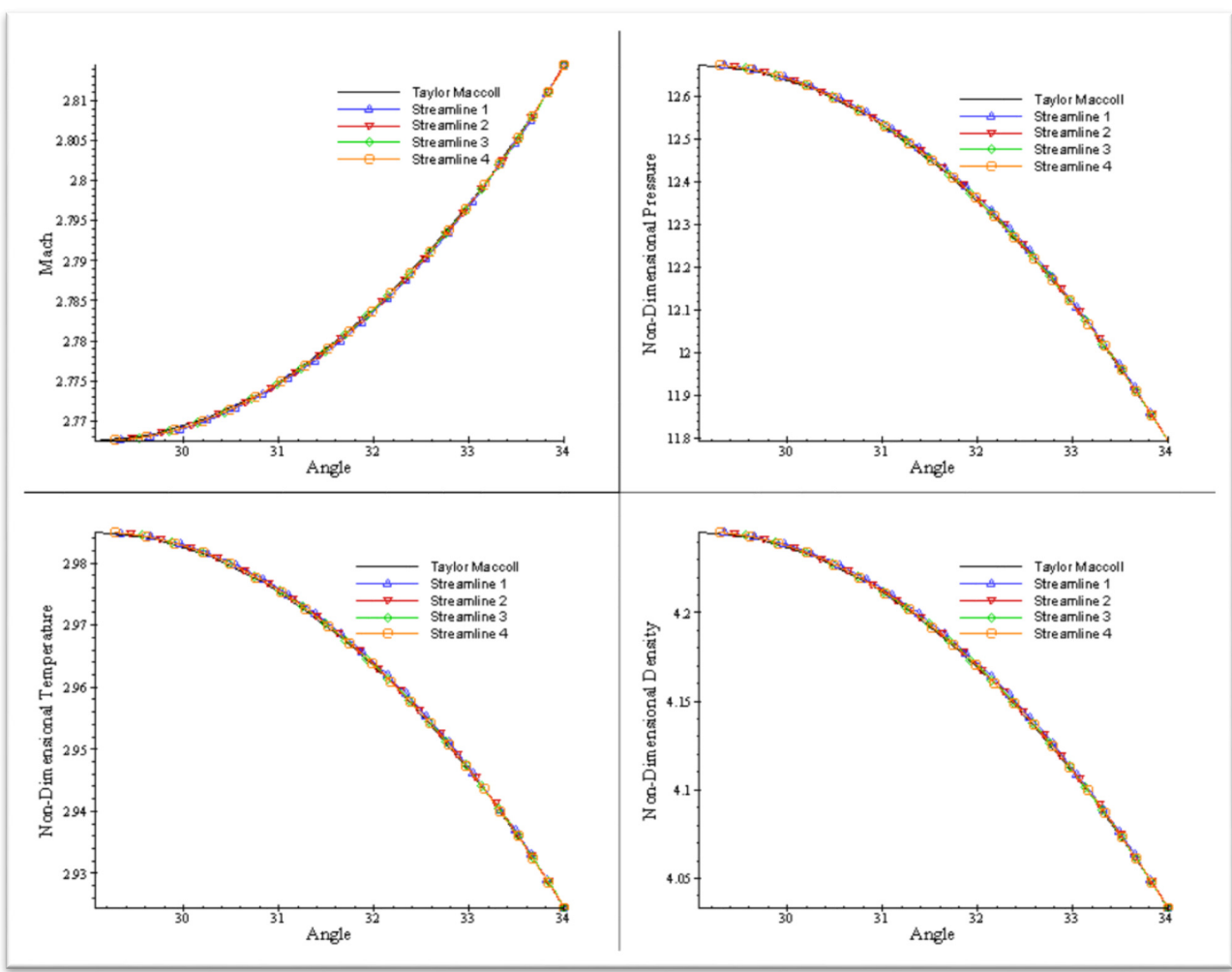


Figure 4.3. Flow field streamline properties vs Taylor Maccoll solution

4.1.2 Streamline to Solid Line Validation

For the transformation of a streamline to a solid line, empirical relations and theory for flow over a compressible flat plate were relied upon. Since established engineering correlations

are used, the validation exercise only aims to show that relations were properly implemented. Experimental results from Neal[63] were compared to viscous analysis results obtained along a streamline for skin friction and heating coefficients vs the local Reynolds number. Refer to Figure 4.4 and Figure 4.5. The results of the model used were overlaid in red onto the graphs extracted from Neal.

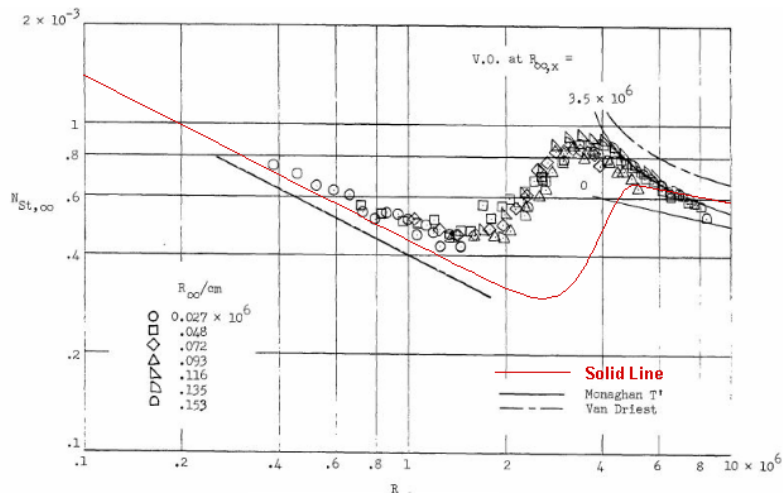


Figure 4.4. Validation of stanton number calculation with overlap graph

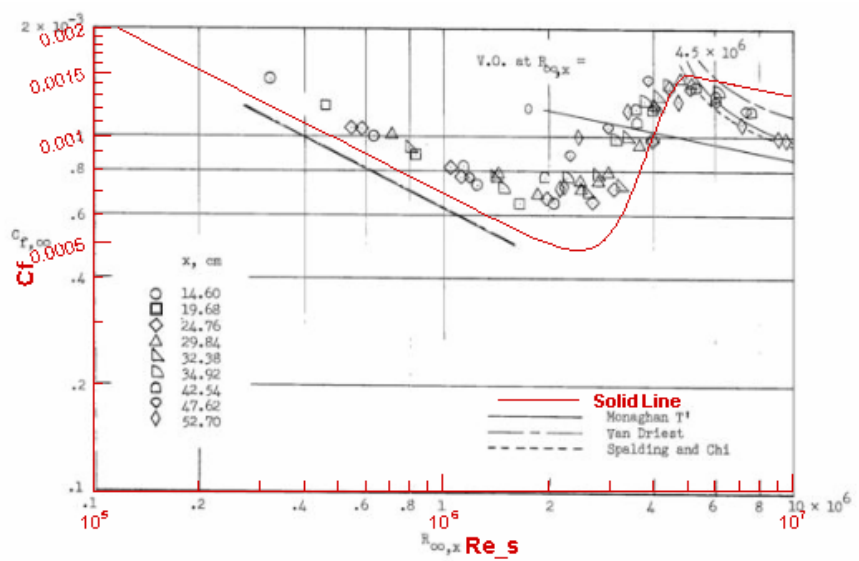


Figure 4.5. Validation of Cf calculation with overlap graph

The figures show that both the laminar and turbulent values are in good agreement with experimental results. In the laminar region, the model used has better agreement than the Monaghan. However, in the turbulent regime the model used does not agree as well with the experimental data. In addition, the predicted transition point is beyond that of the experimental data but well within reason. This may actually be a decent sign since it has been shown that transition occurs later in atmospheric conditions compared to laboratory environments.

4.1.3 Blunt Body Solid Line Validation

In order to perform validation for the method used to determine local pressure and heating on a blunt surface, an experimental study conducted by Richards[68] on a blunt body, illustrated in Figure 4.6, was utilized. The method formulated was applied to the blunt portion of the body defined by the equation. The results from the methods discussed in Section 3.3.2(red) were overlaid onto the experimental results showcased by Richards; refer to Figure 4.7 and Figure 4.8.

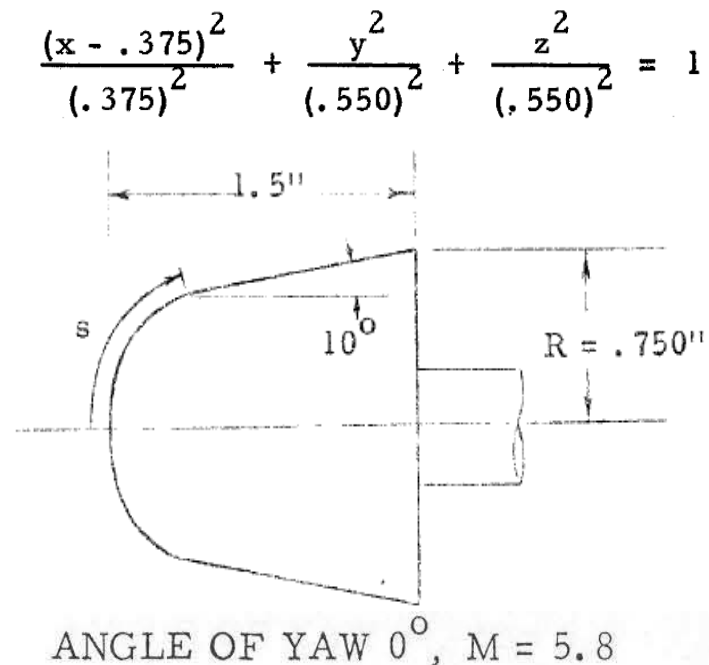


Figure 4.6. Blunt body experiment conducted by Richards[68]

Figure 4.7 shows the comparison of the experimental and modified Newtonian ratio of the coefficient of pressure distribution across the body. It is observed that the method was implemented properly since it lies directly onto the Newtonian line. However, there is some observed discrepancy far removed from the nose region. This is because only the blunt portion was modeled and the 10° conical portion of the body was not modelled.

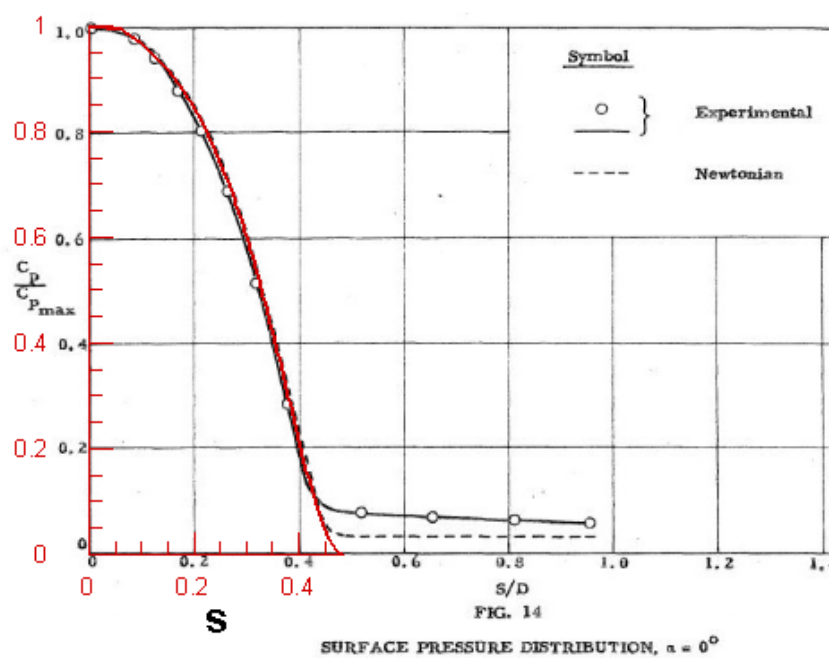


Figure 4.7. Validation of blunt surface pressure

Figure 4.8 shows the comparison of the ratio between local heat flux and stagnation heat results from the Fay-Riddell model used and experimental data. The graph merely shows the trend of the distribution of heat across the body. The trends seem to closely agree close towards the nose region but disagree far from the nose. This may also be attributed to the model of the geometry. The comparison between the calculated stagnation heat, $42,526.7\text{W/m}^2$, and the experimental heat, $27,006.8\text{W/m}^2$, shows a 55% difference. Therefore, the model over predicts the heating as compared to this experimental study.

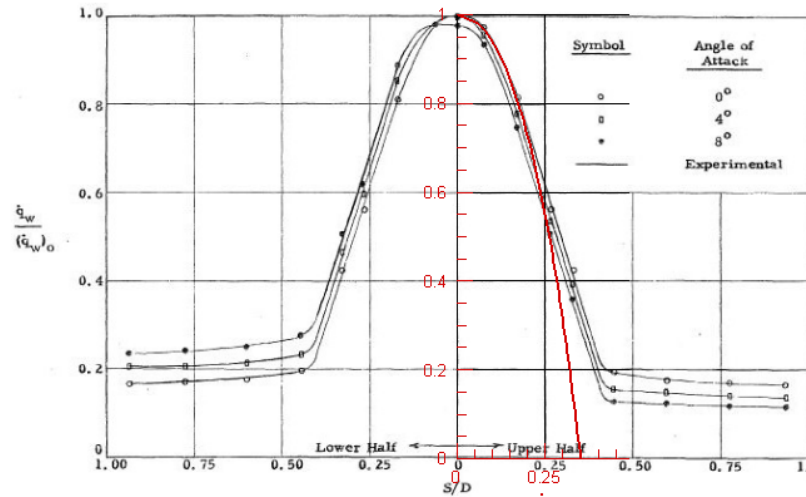


Figure 4.8. Validation of blunt heating distribution

4.1.4 Surface Mesh Validation

The grid generation begins with a surface mesh formed using spline routines. Validation of the surface mesh routine was conducted through visual inspection. It verified that the meshed geometry stayed true to the original waverider geometry. Consider Figure 4.9. It shows the two surface meshes; the original surface mesh is indicated in purple and the redefined mesh in black. Further, Figure 4.9 illustrates the typical behavior of transforming the waverider from one grid system to the next, and justifies the integrity of the transformation procedure developed and implemented herein.

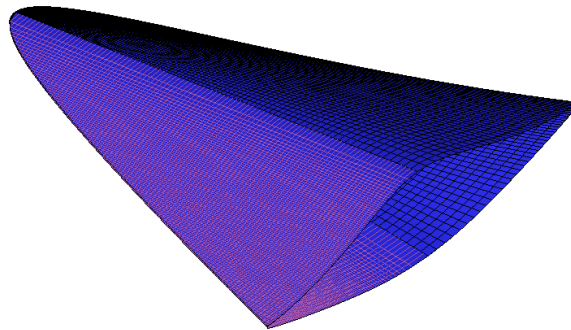


Figure 4.9. Black surface mesh overlaid onto original geometry

4.2 Comparative Studies with Computational Fluid Dynamics (CFD)

In an effort to further validate the waverider design methodology; examine the integrity of its analysis methods; and measure the degree of success of its grid generation procedure, an extensive and independent CFD analysis was conducted. Euler, laminar and turbulent case studies were conducted. The automated grid generation feature discussed in Section 3.5 created the computational grids used in these tests. In addition, the computational grids were created to best model, both, the fluid physics over the waverider configurations at hypersonic speeds, and the unique geometric features of the ‘streamlined body’ and ‘blunted leading edges’ of each waverider. Also used in these studies were the Air Vehicles Unstructured Solver (AVUS) CFD aerodynamic analysis tool, and the flow field visualization tool, TecplotTM. AVUS is a finite volume unstructured-grid Euler and Navier-Stokes solver developed at Air Force Research Laboratory. Its algorithm is cell-centered, first-order accurate in space and time and based on exact Riemann solver of Godunov[69]. TecplotTM is a commercially available tool, commonly used in the CFD industry.

As discussed in Chapter 2 section 2.3.3 the choice of the Mach number and the other design inputs for the case study was guided by the requirements of the hypersonic glide corridor and to some extent, the capabilities of Navier-Stokes solvers. The pressure and temperature were hardwired. The conditions set for the test case are as follows:

Table 4.1. Conditions for chosen case study

$R_{Bluntness}$ (%)	M_{inf}	P_{inf} (N/m ²)	T_{inf} (K)	T_{Wall}/T_{inf}
0.25	6.0	290.0	290.0	Adiabatic

The flow was initialized as free stream. The boundary condition were prescribed as follows; symmetry plane was set as a slip wall, waverider surface as no slip walls and the remaining bounds

of the volume mesh as a modified Riemann invariant far field. The focuses for comparisons were shock shape, shock location, flow field, surface pressure and overall aerodynamic performance.

4.2.1 Euler comparative analysis

In the Euler study, the waverider surface was consider as a slip wall. In this case, the behavior of the flow field within the neighborhood of the waverider is of utmost interest. Figure 4.10 shows the overall flow field in terms of pressure. It clearly illustrates an axis-symmetric like flow field about the lower surface of the waverider. It is important to observe the shape of the shock that emanates from the leading edge. Figure 4.11 gives a closer look where the Euler results are compared at the base plane to the flow field used to construct the waverider. The comparison show the shape and location of the shock are in close agreement. In addition, the pressure distribution throughout the flow field closely agrees as well with small discrepancies that can be explained. For example, the construction flow field was used to derive an ideal waverider whereas the CFD study was conducted on a blunted waverider. Therefore, the offset of the shock is due to the small addition of blunting which causes the shock to standoff from its ideal location. Also due to blunting, and as expected, there is some leakage of flow and thus pressure variation around the leading edge shown in Figure 4.11. However, the leakage does not greatly influence the pressure distribution across the upper surface, which sees uniform pressure close to the free stream value, thus yielding the expected designed characteristics. In addition, the pressure along the lower surface is dictated by the post-shock flow field. The results strongly confirm the legitimacy of the waverider inverse design methodology.

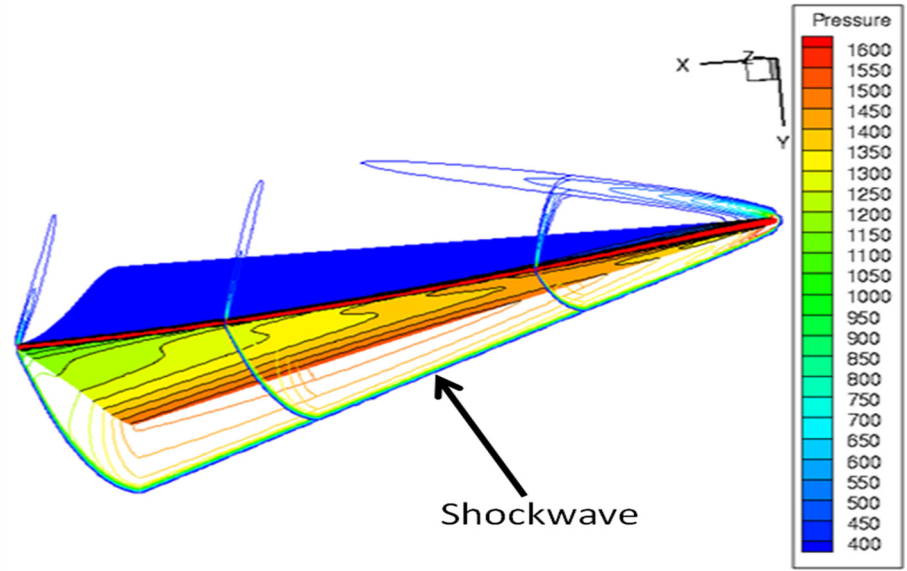


Figure 4.10. Shockwave shape from pressure field from Euler results[61]

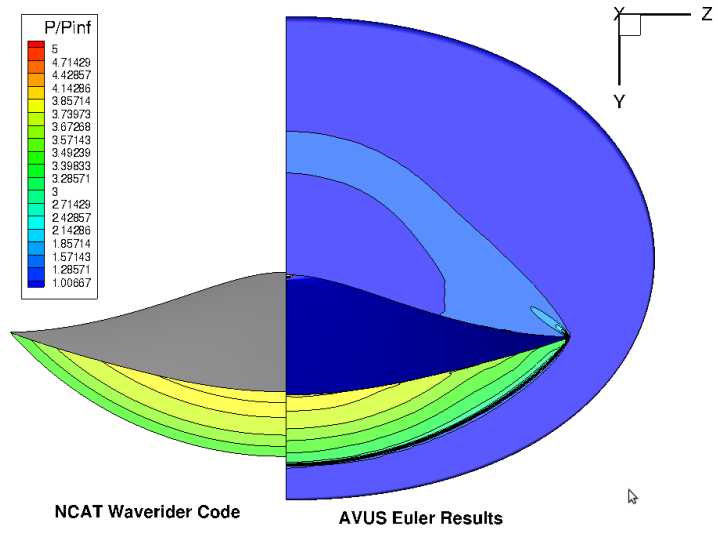


Figure 4.11. Base non-dimensional pressure comparison of method and Euler results [70]

Figure 4.12 and Figure 4.13 reiterates the comparison of the flow fields at the symmetry plane. Again, the higher pressures in the nose region of the Euler study display the effects of the leading edge and blunting. The induced pressure rise towards the leading edge due to blunting

deteriorates downstream yielding a pressure distribution similar to the flow field that does not account for blunting. Additionally, Figure 4.14 shows that the Mach is uniform within the shock layer as expected.

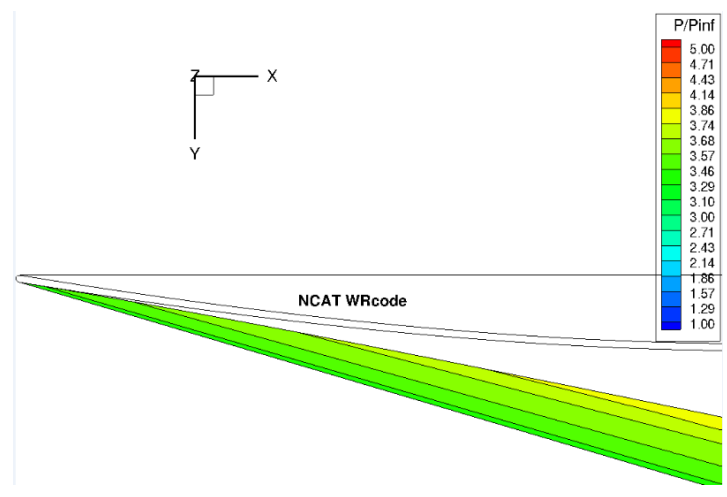


Figure 4.12. Semi analytical flow field at symmetry plane

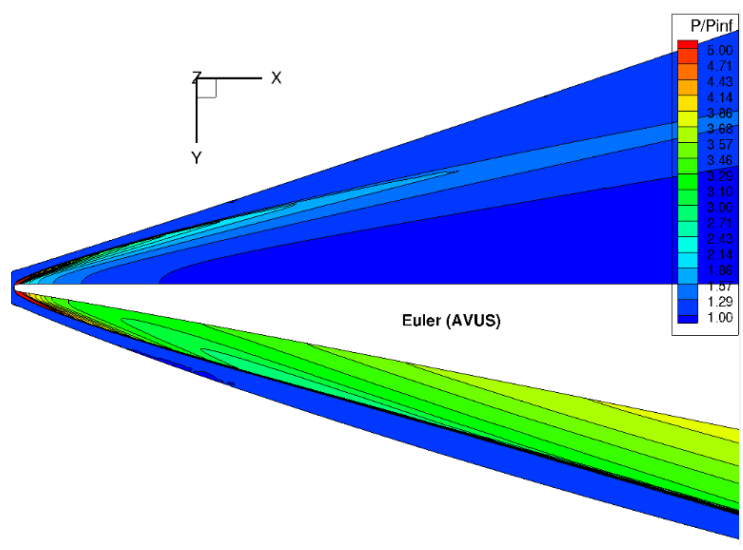


Figure 4.13. Comparison of pressure ratio at symmetry plane

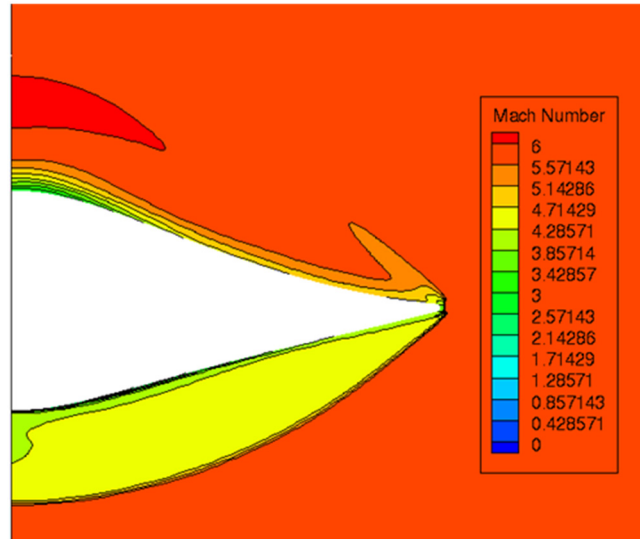


Figure 4.14. Mach at base plane for Euler results

Another technical feature of interest to design engineers and subject for comparison are the streamlines location and behavior. Recall, the upper and lower surfaces were formed by tracing streamlines. Figure 4.15 shows the streamlines along the surface resulting from the Euler study of the blunted waverider (colored in black) overlaid onto the streamline mesh that formed the ideal surfaces (colored in red). The streamlines of the Euler study clearly depict the stagnation line in the mid-region of the blunt surface where stagnation was assumed. Figure 4.16 and Figure 4.17 show the Euler study streamlines overlaid onto upper and lower surface streamlines respectively. For both cases, the streamlines are in close agreement close to the leading edge but veer off towards the tip downstream. This may be due to the blunt surface design, which influences the flow towards the tip. The influence is stronger on the lower surface than the upper surface. However, it is important to acknowledge the streamlines that emanate from the nose region want to deviate towards the root of the waverider. It is not clear as to why this may be the case. One suspicion is there may be some deviation in the geometry close to the nose region that was not detected during the visual inspection of the mesh. Even with the disagreements between the particular streamlines,

the general flow field was recovered as presented in the pressure contours. Therefore, minor discrepancies that may be present in the geometry do not greatly disturb the overall flow field.

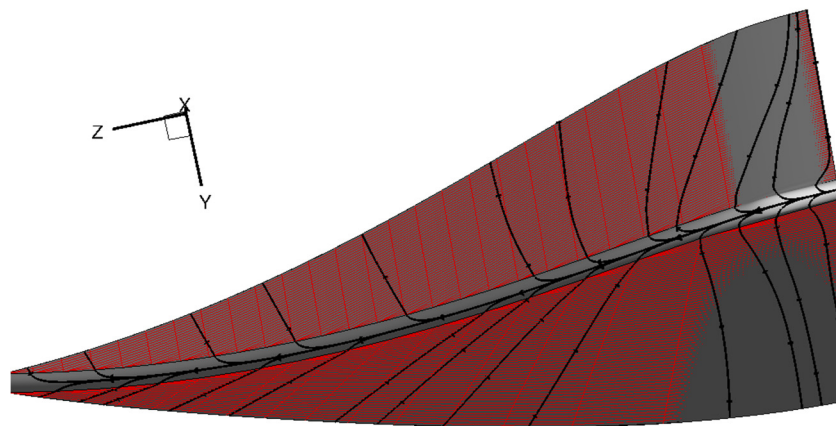


Figure 4.15. Streamlines emanating from blunt surface

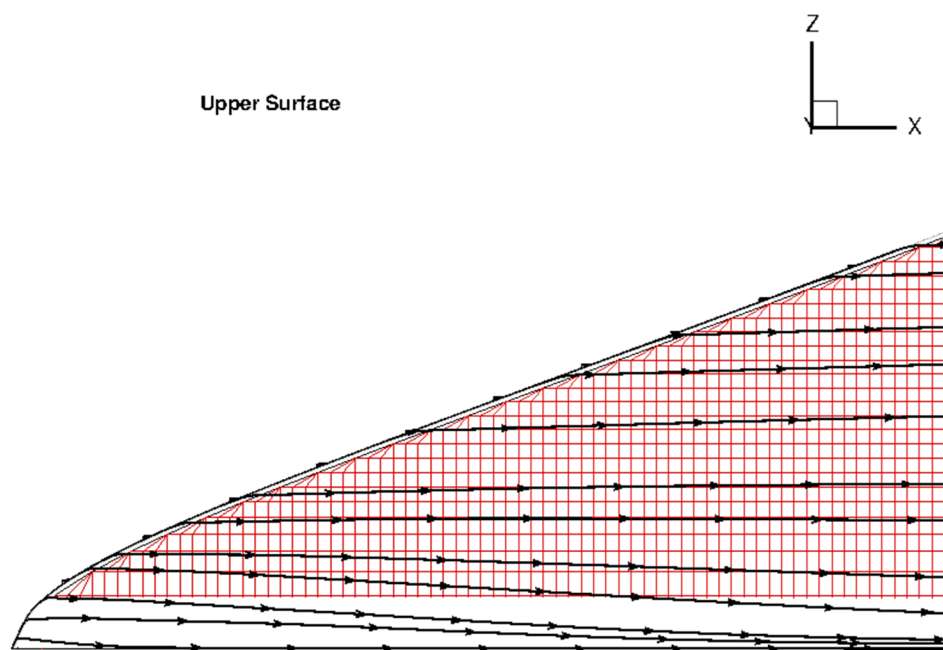


Figure 4.16. Streamline comparison on upper surface

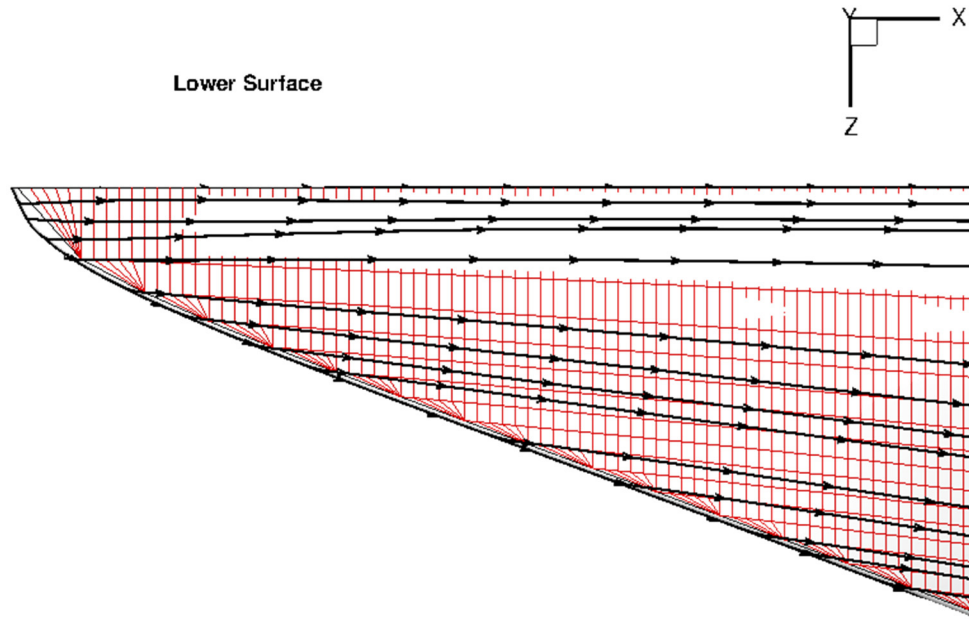


Figure 4.17. Streamline comparison on lower surface

4.2.2 Viscous comparative analysis

In efforts to validate the newly created waverider analysis methods, both laminar and turbulent CFD studies were conducted, again using the independent AVUS tool, while the local surface properties were compared. During this case study, the turbulence model selected was the Spalart-Allmaras model. The results of the laminar and turbulent flow fields were prepared in identical plots and displayed in Figure 4.18 thru Figure 4.21 for ‘side-by-side’ comparison. In this study, the effects of blunting, viscosity and turbulence were observed. Figure 4.18 shows the Mach contours at the symmetry plane with streamlines for the laminar flow field. The streamlines indicate the validity of the design methodology by displaying the flow traveling parallel to the upper surface and being process by the shock at the lower surface. The turbulent and laminar Mach contour comparison at the base plane, shown in Figure 4.19, shows the existence of a boundary layer for both cases as expected. Furthermore, the turbulent boundary layer is thicker at

the base cross-section. Thus, the shock is further detached from the body as assumed in the automated grid generation process.

The pressure contour comparison, Figure 4.20, shows the effects of a thicker boundary layer within the flow field. Boundary layer theory concludes that pressure along the normal from the surface does not change within the boundary layer. This is also captured in the pressure contour line results shown in Figure 4.21 and Figure 4.22. However, beyond the boundary layer the flow fields are quite comparable to the flow field from which the waverider is constructed. It is also worthy to note that the flow field induced by and around the blunting is further influenced by the addition of viscous and turbulent effects. Figure 4.20 highlights the enhancement of the viscous-blunting leading edge effect due to turbulence. Whether this can be attributed to the actual existence of turbulence or merely an artifact of the turbulence model has yet to be determined or speculated.

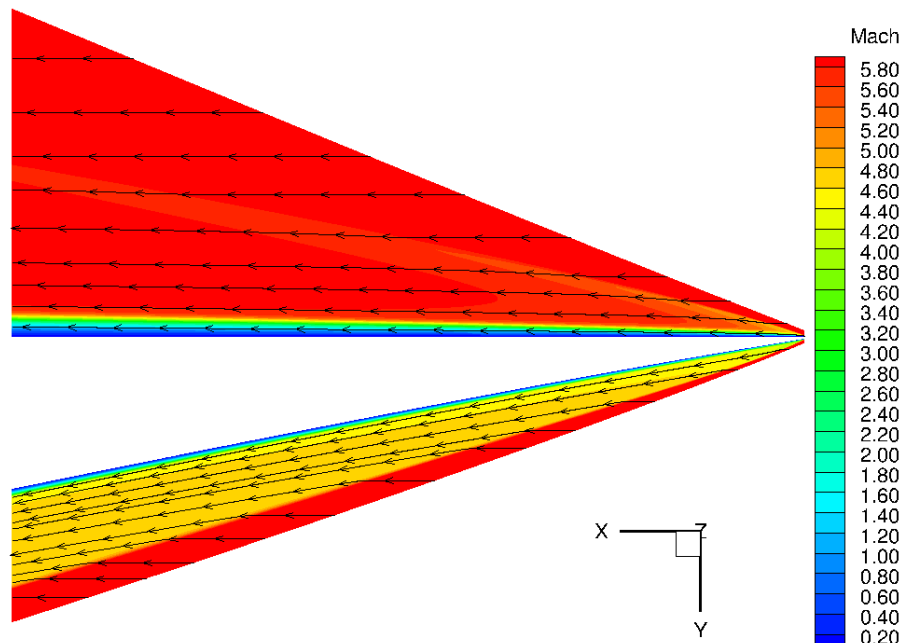


Figure 4.18. Streamline distribution and boundary layer thickness recovery

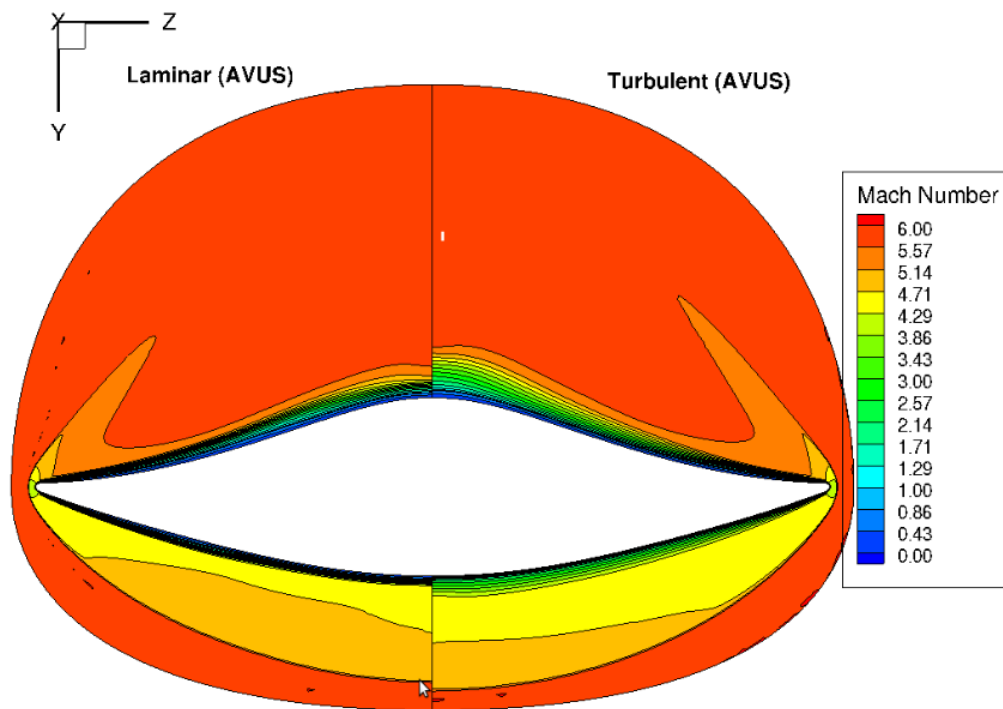


Figure 4.19. Laminar vs. turbulent base plane Mach

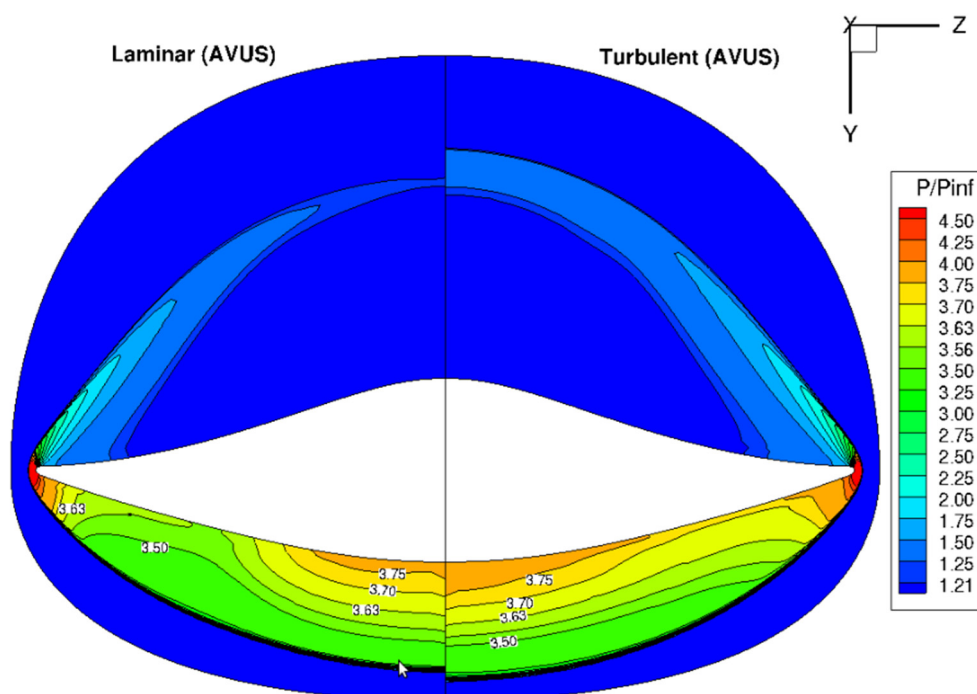


Figure 4.20. Laminar vs turbulent base pressure ratio

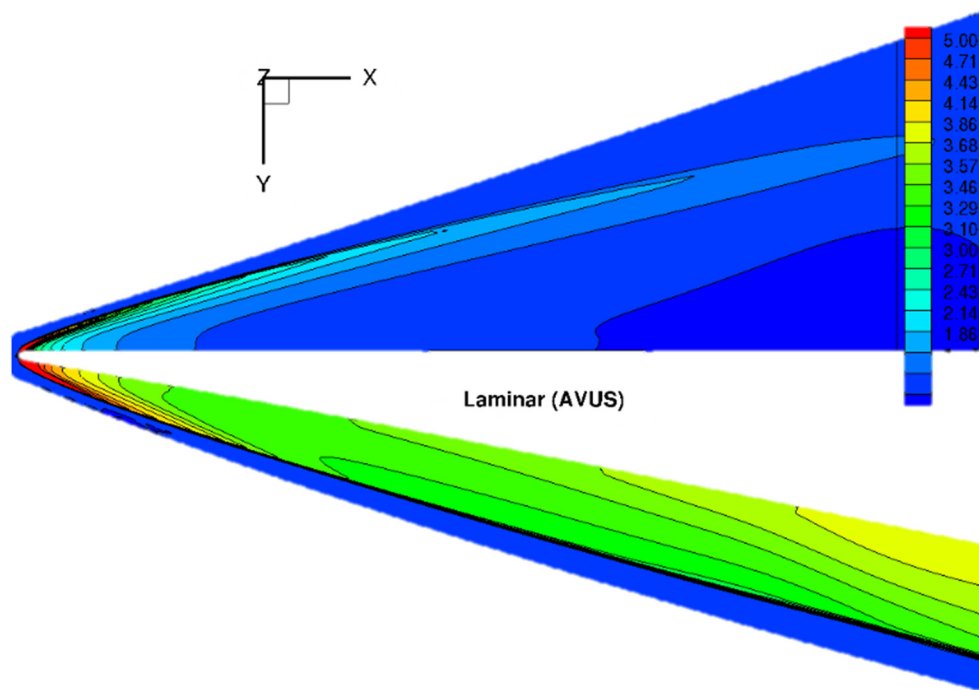


Figure 4.21. Laminar pressure at symmetry plane

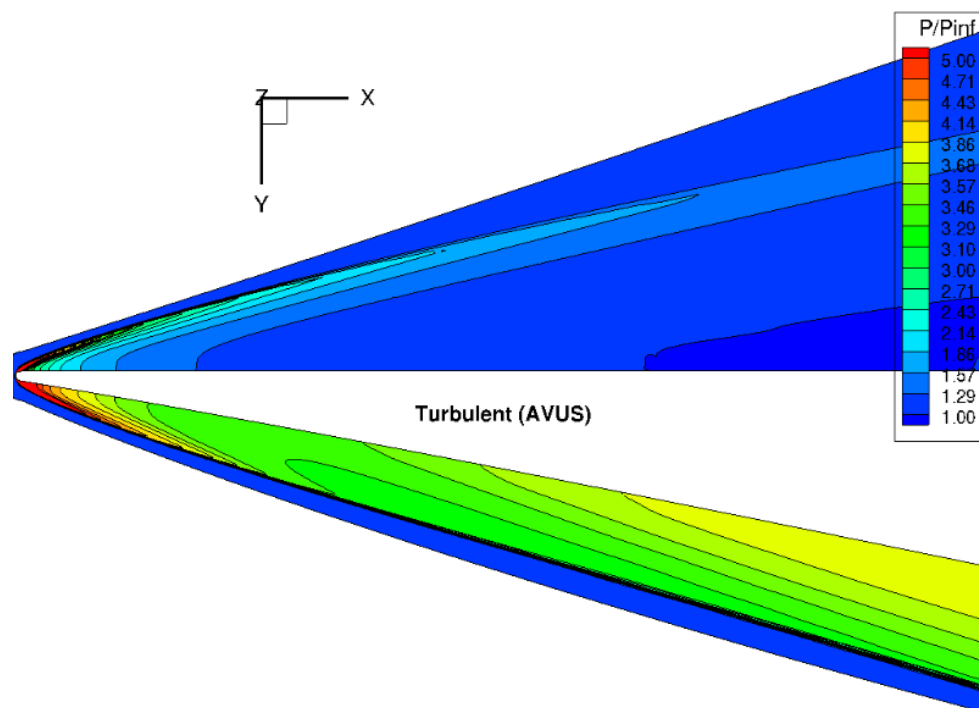


Figure 4.22. Turbulent pressure ratio at symmetry plane

The results of the viscous CFD study demonstrated that the far-field pressure distribution around the waverider under design conditions was recovered. As illustrated in Figure 4.23 and Figure 4.24, the waverider appears to be riding its own shock wave. A relatively weak blunt shock wave with a small standoff distance is captured along the leading edge of the vehicle as seen in the Euler study. Again, the shape of the shock resembles the prescribed design shock. A closer look of the pressure flow field is illustrated in Figure 4.25. There it can be seen that not only is the flow field on the under belly of the waverider uniformly conical, but at cross-sections of one-thirds, two-thirds and at the base of the vehicle show remarkable similarity of that reminiscent of a conical flow field as well.

Further, another two slices of the flow field are presented in Figure 4.26 and Figure 4.27 to give forth another observation. There are shown two azimuthal planes of the pressure distribution contour. Figure 4.26 shows the plane at 0° , which is equivalent to the symmetry plane. Figure 4.27 illustrates the pressure distribution in an azimuthal plane approximately 20° relative to the symmetric plane. Each plane illustrates that the bulk of the flow field remain conical, except for regions close to the leading edge which show the induced pressure region. Reviewing Figure 4.23 thru Figure 4.27, one can observe the induced pressure region covers a set area along the leading edge. Thereby, showing a relatively larger effect on the smaller cross-sections. Again, evidence of the recovery of a conical flow field is clearly visible. However, the influence of the leading edge is visible as well. Nonetheless, CFD studies have reaffirmed the capability of the methodology to produce waveriders by reproducing a similar flow field from which the waverider is derived.

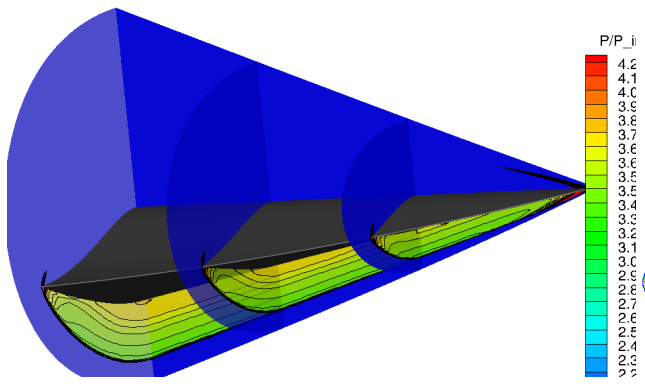


Figure 4.23. Pressure field results

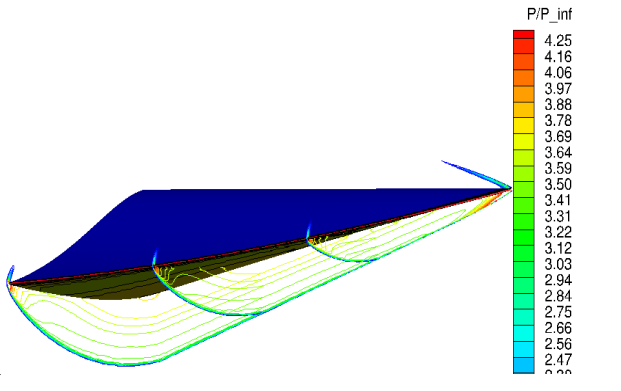


Figure 4.24. Shock with pressure results

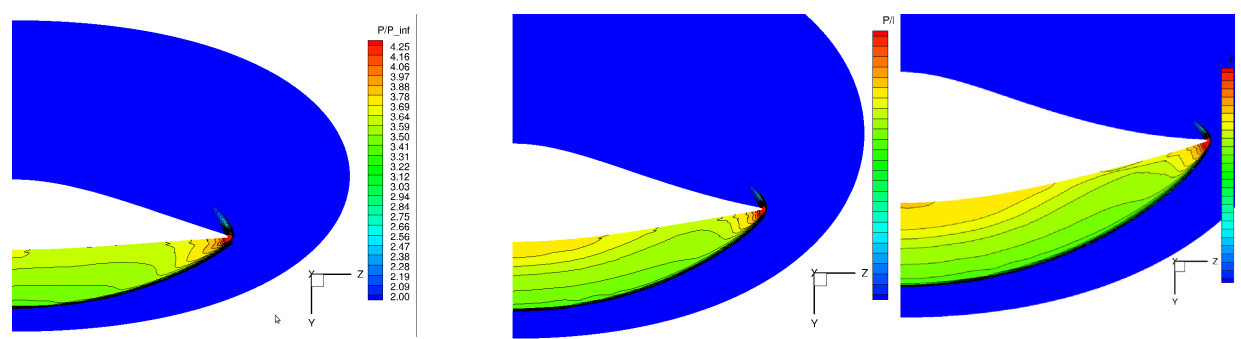


Figure 4.25. Pressure distribution at cross-sections of one-thirds, two-thirds and base plane

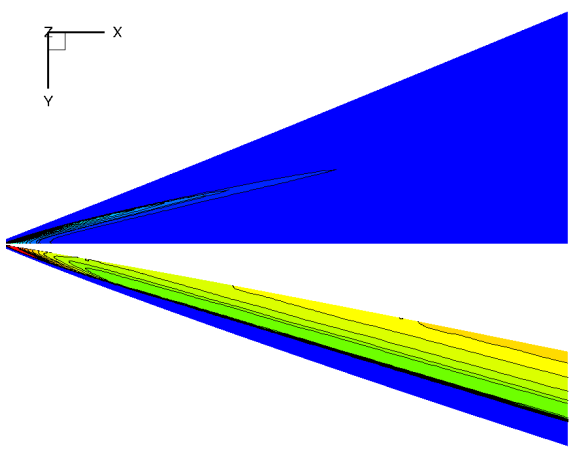


Figure 4.26. Viscous symmetry plane results

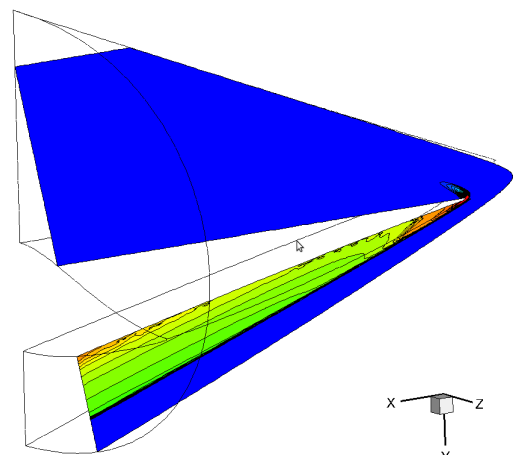


Figure 4.27. Azimuthal plane (20° inclined)

The viscous effects displayed in the flow field translate to the pressure distribution on the surface. The comparisons of the surface results from all the different analysis methods are

discussed, namely the three CFD studies and the inviscid wall pressure as well as the ‘viscous’ wall pressure stated in section 3.2.1. Recall the inviscid surface pressure is determined by the constructed streamlines and the viscous surface pressure incorporates the viscous interaction parameter. Figure 4.28 and Figure 4.29 demonstrates the comparison between the inviscid surface pressure and the viscous surface pressure determined, as discussed in section 3.2.1, for the lower and upper surfaces, respectively. As expected, there is a higher-pressure region in the empirical viscous result along the leading edge as well as an overall higher pressure across the entire surface. This holds true for both the lower and upper surfaces. It is interesting to observe that the viscous pressure distribution on the lower surface no longer alludes to a conical flow except for the region that is downstream towards the root. However, the pressure distribution on the upper surface hints at a conical flow surrounding the surface. Recall, the size and presence of the blunt surface has not been taken into account. Therefore, the differences between the surface pressures are strictly driven by viscous interaction with the leading edge according to the model employed.

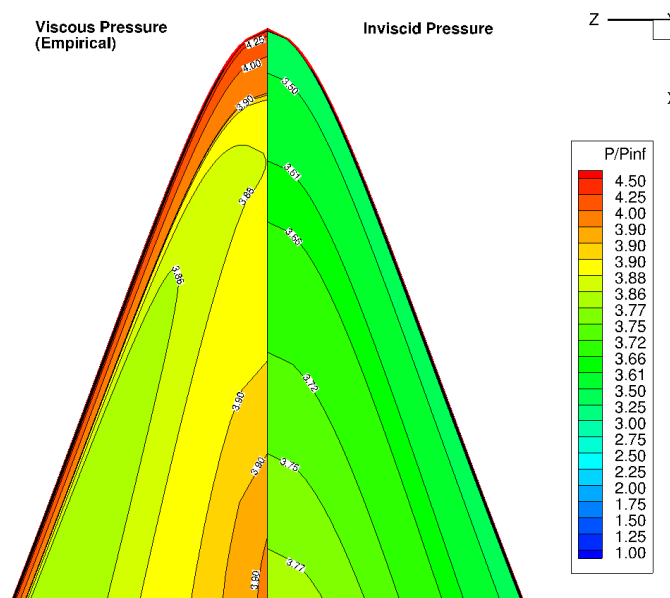


Figure 4.28. Inviscid vs viscous lower surface pressure

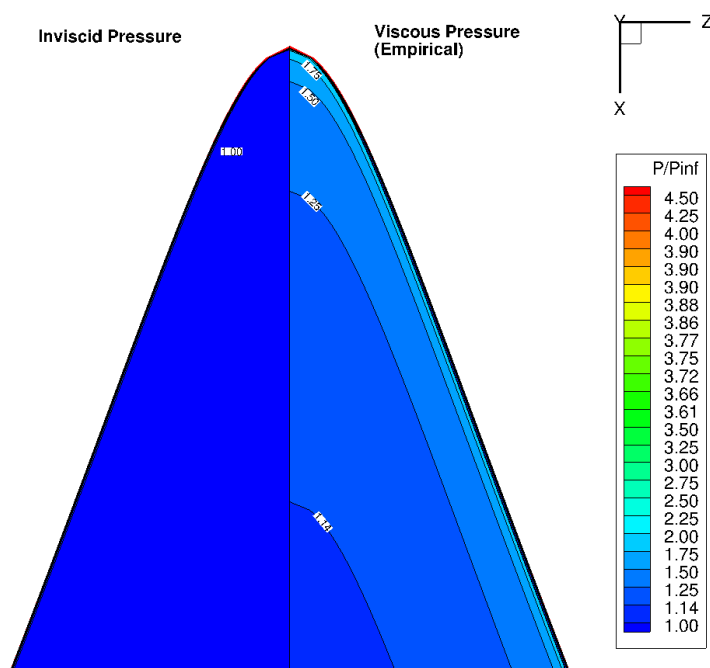


Figure 4.29. Inviscid vs viscous upper surface pressure ratio

For the purpose of curiosity, the CFD viscous (turbulent) pressure distribution was compared to the CFD inviscid (Euler) for the upper surface, shown in Figure 4.30. Solely the blunting effect is shown in the Euler result, showing that induced pressure is greatest towards the nose region. Notice blunting does not induce an increase in pressure across the entire surface like the viscous model. The turbulent results show the combination of influences from blunting, viscosity and turbulence. A small region which is downstream towards the root is unaffected by the leading edge effects. This is contrary to the viscous model used, which suggests that pressure across the entire surface would be higher relative to an inviscid study. This contradiction is further illustrated in Figure 4.31 and Figure 4.32 with the comparison of the viscous model results and the turbulent CFD results for the upper and lower surfaces, respectively. Here all but the leading edge seem to disagree. However, the added blunting effect present in the CFD yield disagreement in the nose region. The lower surface comparison, Figure 4.32 shows more of a disagreement with contour lines and values.

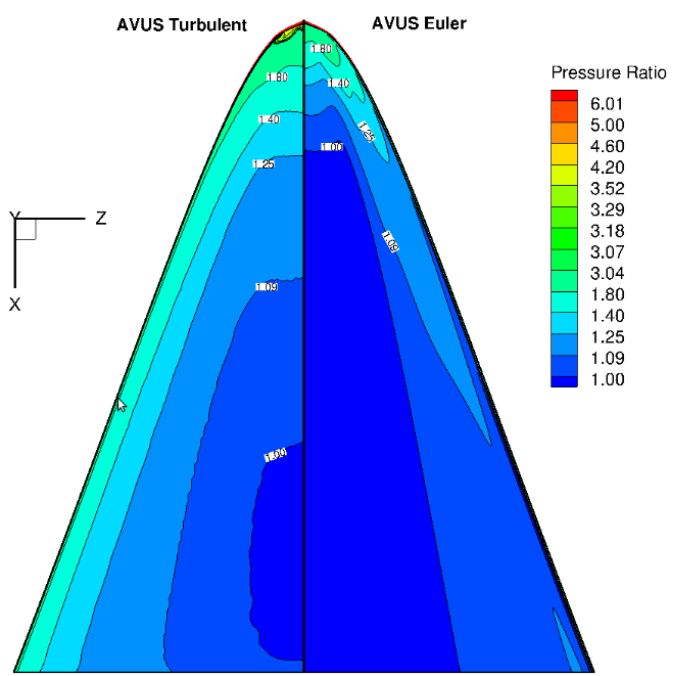


Figure 4.30. Turbulent vs Euler upper surface pressure

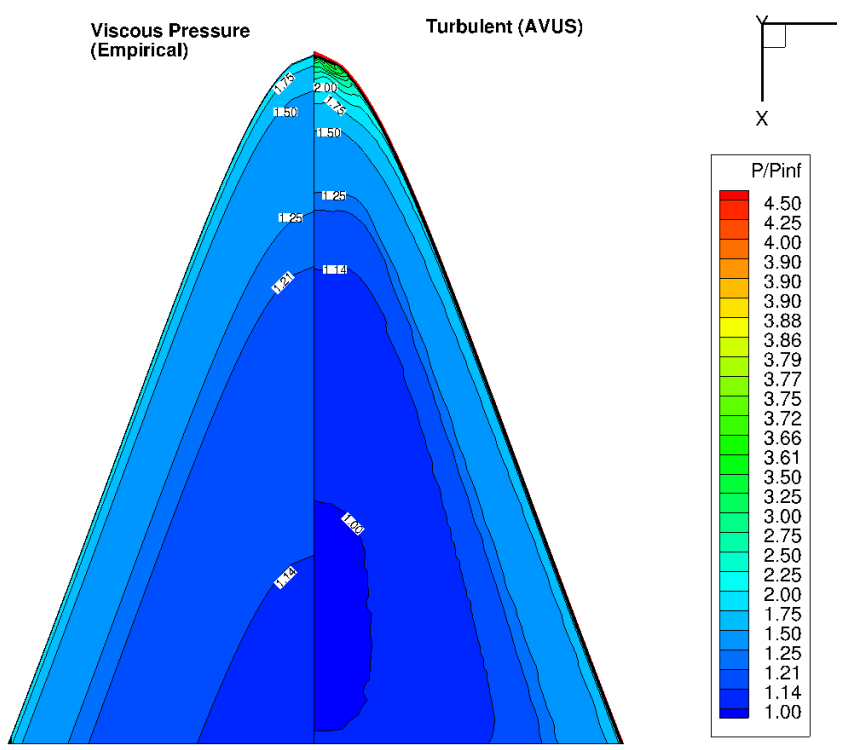


Figure 4.31. Viscous vs turbulent upper surface pressure ratio

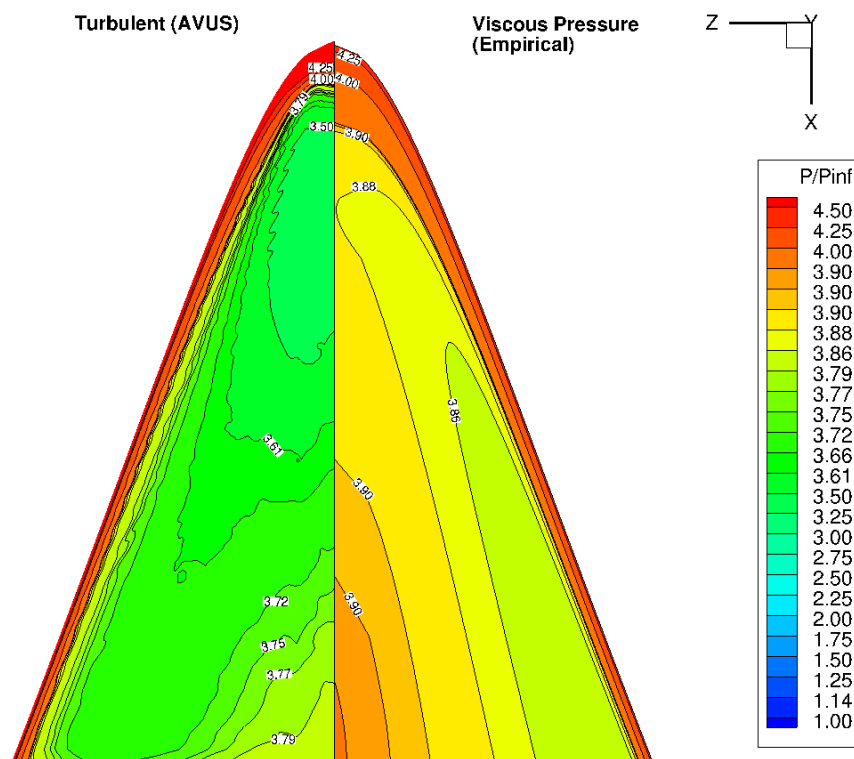


Figure 4.32. Turbulent vs viscous lower surface pressure ratio

The viscous pressure model showed very poor agreement with CFD. Figure 4.33 shows the comparison of the inviscid (streamline) model, denoted as NCAT WRcode, with the CFD turbulent model. Strangely, the pressure from the pure streamline matches closer to the turbulent solution downstream towards the root. Also the middle of the surface shows a low pressure region that is less than any pressure along the inviscid surface. Referring back to Figure 4.31, the upper surface does not show any low pressure region. Figure 4.34 shows a similar trend in the laminar solution. However, its comparison of values with the inviscid model does not agree as well. However, the low-pressure region is a point of investigation. It suggests that there is an expansion experienced slightly downstream from the leading edge. In addition, the intensity of the expansion would possibly be governed by the change in geometry immediately downstream of the leading edge.

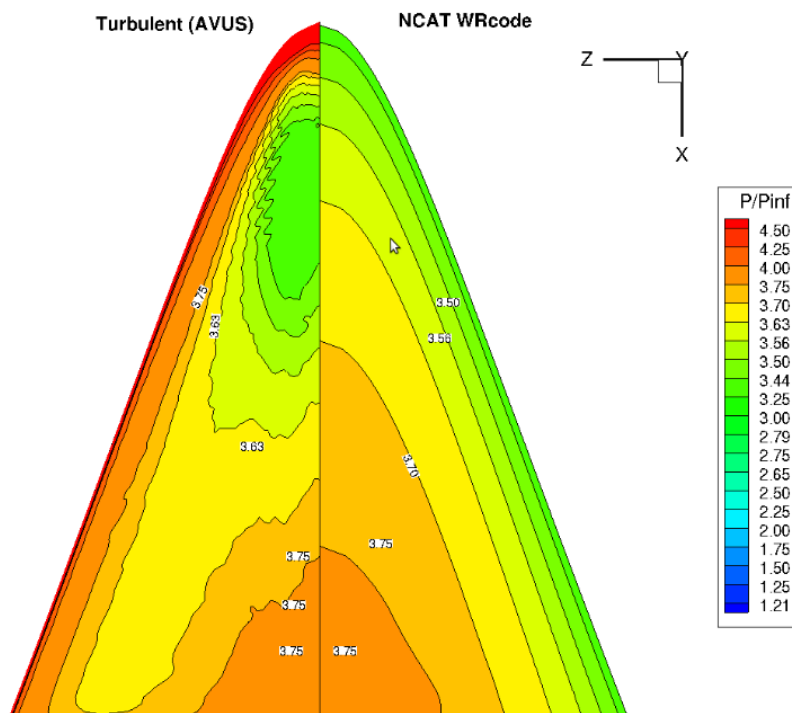


Figure 4.33. Turbulent vs inviscid lower surface pressure ratio

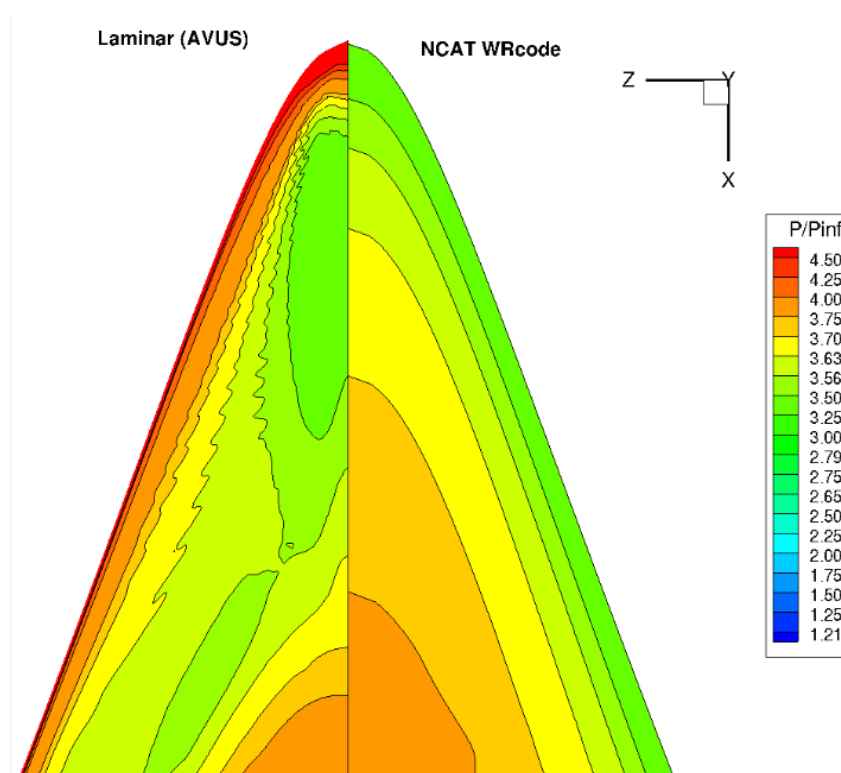


Figure 4.34. Laminar vs inviscid lower surface pressure ratio

Figure 4.35 shows the pressure ratio along the symmetry line of the upper (dashed) and lower (solid) surfaces of the turbulent CFD solution (solid black), viscous model (red) and the inviscid streamline model (blue). The line plot compliments and reiterates the observations presented in the contour comparison plots. The line plot of the turbulent CFD suggests that the blunting effects completely diminish about 25% of the vehicle's length, which is proportional to the size of the blunt radius. In addition, focusing on the line plot comparison on the upper and lower surface, the viscous effect completely diminishes at about 60% of the waverider length. There is also an observable difference between the inviscid and viscous pressure ratio, which begins around 35% of the waverider length. Clearly, the low pressure region observed in the CFD solution along the lower surface does not follow any trend presented in the other solutions.

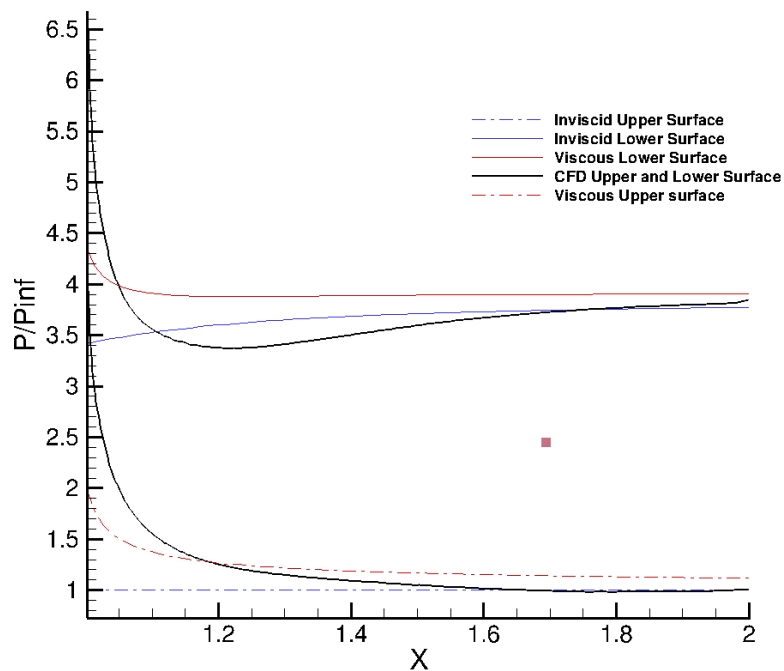


Figure 4.35. Comparison of surface pressure analysis along symmetry plane

However, its minimum pressure value lies very close to the minimum pressure of the inviscid streamline seen at its leading edge. Ironically, the minimum pressure on the lower surface occurs

at the same point downstream along the waverider length where the CFD solution matches with the viscous pressure model used on the upper surface. At this time, no credible explanation or logical correlation for these observations can be given.

For the nose region of the blunt surface, Figure 4.37 shows that the laminar and turbulent results were in good agreement. Figure 4.36 shows the modified Newtonian theory does not only agree well with experimental data but also CFD. This reassures the use of modified Newtonian theory for the blunt surface.

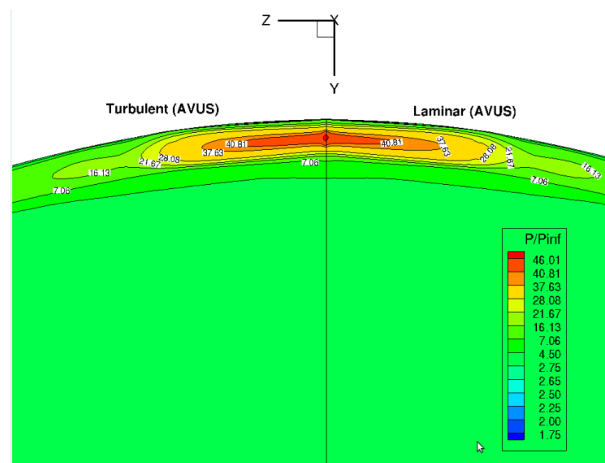


Figure 4.36. Turbulent vs laminar nose surface pressure ratio

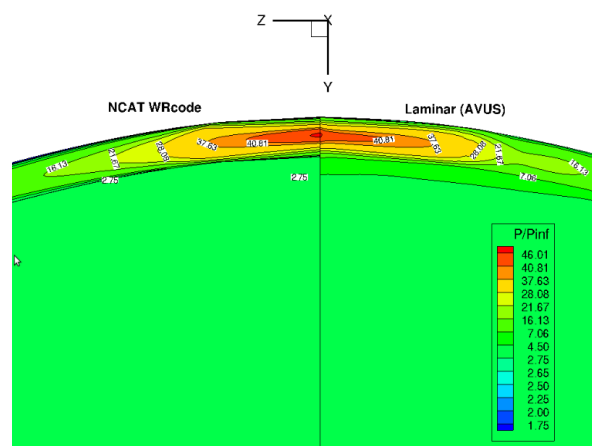


Figure 4.37. Laminar vs modified Newtonian nose surface pressure ratio

Recall, the analysis method discussed in section 3.4.2 integrates all surface information in order to determine the lift and drag of the geometry. TecplotTM was utilized to determine lift and drag from the CFD results. Each analysis method's aerodynamic performance is tabulated in *Table 4.2*. In addition, the performance of the ideal waverider from which the blunted waverider is derived is included. The CFD results yield similar lift, drag and L/D ratios even though the surface pressures profiles varied. The induced pressures, seen by the upper and lower surfaces, are due to viscous and leading edge design effects, and the observed results seem to suggest that they cancel each other. Clearly, the ideal geometry has the highest lift and lowest drag yielding the highest L/D ratio. The modified waverider with the particular size and type of blunting discussed reduced lift and increased drag thereby reducing the L/D ratio by approximately 90%. The lift from the viscous blunted waverider analysis method compared well with the CFD studies, yielding a percent difference of 2%. Unexpectedly, the drag differed greatly with a percent difference of 86%, which drove a percent difference of 85% for the L/D ratio. The surface pressure profile suggested that the comparisons should have been closer- This may be due to an induced shear from the leading edge interaction, which was not incorporated in the analysis method.

With improvement in the analysis method for determining drag, the preliminary analysis phase time would be cut dramatically with trustworthy aerodynamic performance results. Notice, the solution time for each method. The analysis methodology discussed in Chapter 3 is based on strategically applied theory and empirical relations for lightning speed analysis of the surface. Even though, CFD studies yield analysis of the surface as well as the surrounding flow field, the cost is on the order of days as compared to seconds with the WRcode. Refer to *Table 4.2*. The days included in *Table 4.2* do not include independent grid generation. However, the automated grid generation discussed in section 3.5 will add less than five minutes to the solution time.

Table 4.2. Aerodynamic performance comparison of analysis methods

Solution	Lift (N)	Drag(N)	L/D	Solution Time
Ideal Waverider	9.3E+04	2.8E+04	3.289	< 1min
Viscous Blunt Waverider	2.961E+04	9.802E+04	3.02E-01	< 1min
CFD Euler	3.028E+04	2.4714E+05	1.2248E-01	~3.5days
CFD Laminar	3.027E+04	2.4714E+05	1.2250E-01	~5 days
CFD Turbulent	3.027E+04	2.4716E+05	1.2248E-01	~6 days
% Difference CFD vs Method	2%	86%	-85%	-

CHAPTER 5

CONCLUSION

5.1 Accomplishments

In an attempt to contribute to the technical efforts required for the development of the next generation hypersonic aerospace vehicles, a ‘waverider based design’ model was created. Further, the newly created ‘waverider based design’ model which consist of numerous numerical methods was coded in FORTRAN, successfully executed and independently validated. Moreover, this effort demonstrated how at first glance a ‘seemly unrealistic’ waverider configuration can be transformed into a realistic hypersonic vehicle with propulsive and control surfaces. Using the NCAT WRcode, the waverider design space can be formed and use to derive configurations which satisfy the much needed technical requirements of highly integrated fore-bodies, engine and nozzle after-bodies suggested by Kuchemann[16]. The ‘waverider based design’ concept is flexible enough to allow for the creation of a hypersonic vehicle through the assembly of stream surfaces from either a single or multiple independent hypersonic flow fields. As part of this effort, a method for blunting the inherently sharp leading edges of idealized waveriders was formulated using Bezier curves and executed to deliver waveriders with an acceptable degree of sharpness. The design approach adopted in this dissertation is parametric; for example, leading edge shapes and ‘viscous-transformed stream’ surfaces can be manipulated to result in waverider configurations for practical designs. In addition, an aerodynamic performance analysis method was created and validated. Currently, the aerodynamic performance analysis method is capable of determining the local pressure, the convective heat flux, and the skin friction coefficient. In addition, the analysis method is equipped with the capable of evaluating the viscous stresses on blunt surfaces by either using a strategic implementation of Fay-Riddell model or the modified Newtonian theory.

Each step of the design and analysis process, which includes post-shock flow field generation, viscous design space, ideal waverider formation, blunting, and full analysis, were validated. The flow field generating scheme, Ferguson's[2] semi analytical solution to the Euler equations, agreed well with the analytical Taylor-Maccoll solution. It was also validated that the empirical compressible flat plate relations with a transition region were implemented properly. However, it is still unclear whether this technique is appropriate to apply to any generic streamline even though it is valid. The process for the analysis of the generic blunt surface has also been validated via comparison to experimental data. The method for integrating the local surface information to determine its aerodynamic performance was discussed and compared to CFD studies. The determined lift compared well with independent analysis but total drag failed to agree with CFD.

CFD analyses were not only used to verify the predictive capability of the WRcode, but also to validate the configuration modification methods implemented in the code. After observing the results of a large number of case studies, the inverse design philosophy of the waverider concept with configuration modification methods incorporated was successfully validated. The coupling of design and proper analysis efforts can expedite the design process to meet the demand of quick design to flight turn around by minimizing the conceptual design phase. For example, referring to *Table 5.1*, a resulting vehicle configuration's Aerodynamic design will have a potential maturity of 5 from the process presented and can quickly move to level 6 with the completion of a realistic CFD study. In addition, fulfillment of the CFD study is further assisted by the automated grid generation routine developed. The robust grid generation is designed to meet the current demands of solvers related to orthogonality at surface and shock as well as clustering in those regions.

Table 5.1. Hypersonic Vehicle Fidelity Assessment [71]

Design Maturity	Color Code	Propulsion	Aero	Structure Weight	Vehicle Performance	Synthesis & Packaging
10	Blue	Flight Data	Flight Data	Flight Vehicle	Flight Vehicle Performance	Flight Vehicle
8	Light Blue	Wind Tunnel Data	Wind Tunnel Data	Components Fab/Test	6-DOF Hardware Simulation	Mock-up, CAD Multi-Eqn. Non-linear
6	Green	CFD Certified	CFD Certified	FEM Certified	3-DOF/6 DOF Trimmed	CAD Multi-Eqn. Non-linear
5	Light Green	Cycle Certified	Engineering Methods Certified	Unit Loads Certified	3-DOF Trimmed	CAD Multi-Eqn Non-Linear
3	Yellow	CFD Uncertified	CFD Uncertified	FEM Uncertified	3-DOF untrimmed	Single Eqn., Non-linear
1	Light Yellow	Cycle Uncertified	Engineering Methods Uncertified	Unit Loads Uncertified	Energy State	Single Eqn. Linear
0	Red	Ideal Cycle	L/D, Cd Estimated	Design Tables	Rocket Equation	Estimated

Another hidden benefit of the inverse design process, which has both conceptual design and preliminary analysis existing in a single environment, is the exploitation of the flow field and surface information for CFD. The method yields information that can complement the CFD process by supplying a reasonable initial solution, which will further minimize CFD solution time.

5.2 Findings

The flow field generation scheme used herein is highly dependable, flexible and accurate. Its comparison with the Taylor-Maccoll solution highlighted its reliability for flow fields that cannot be determined by the Taylor-Maccoll solution. The comparative process showed the promise of the techniques used as well as some shortcomings. Even though, the Euler results were very encouraging with its ability to recover a flow field akin to the developed design space. The surface pressures did not coincide quite as well. As expected, the addition of blunting perturbed the flow field slightly but the deviation was small enough not to discourage the approach. However, the CFD results also showed that the reality of viscosity and turbulence further exacerbated the perturbation of the ideal flow field and the aerodynamic at the surface. Yielding

an area of research that can use more study and investigation because the strategic approximation for said areas did not trend well with independent study. Even though, locally these effects varied throughout the CFD studies, globally they were washed out as affirmed by comparison of Lift, drag and L/D.

The effects of the particular blunting design applied to the case study yielded a similar induced pressure effect on the upper and lower surface. It also slightly deviated the streamline paths along the leading edge. Therefore, the style of the blunt design in addition to its size influence the aerothermodynamics experienced on the vehicle body as well as the leading edge. It seems possible that a strategic blunt design will mitigate heating while increasing lift as well as drag. Nonetheless, the increase in drag will likely outweigh the increase in lift.

The viscous-interaction parameter model over predicts the pressure across the surface relative to CFD study. This suggests that relations for flat plate fall short in their expansion to a generic surface line derived from inviscid streamline information. Nevertheless, it still holds as a reasonable approximation. Another observation one should take away from this work is that the design methodology does not only promote promising L/D values but also yields an advantageous pressure distribution. Higher pressure concentrated at the center of the under belly towards the root promotes stability in flight.

5.3 **Recommendations for Future Work**

The work presented in this dissertation illustrates a framework for a design process for waverider based hypersonic vehicle. There is room in every step of the process for enhancement and strengthening thereby, enhancing the deliverables of the overall process. Since, the flow field generation method developed by Ferguson has been validated using a conical flow field, his method for determining a post shock flow field derived from a generic three-dimensional shock

surface can be incorporated as a design space option in the process. Also, in the development of the viscous design space, the incorporation of methods that entail blunting and viscous effects on pressure distribution, shear, heating and transition similar to the discussion by Simeonides [72] would be an improvement. In addition, other relations for skin friction and heating can be added. For example, the validation study referring to the work of Neal suggests that the Spalding-Chi relation for determining skin-friction and heating in the turbulent regime may be better suited than the relation relied upon. Improvements in the accuracy of the design space will lead to improvements in the determination of the aerodynamic performance.

The process may also be enhanced with an additional analysis method for configurations in off-design conditions, such as angle of attack, Mach number, altitude and medium. An analysis method that can quickly obtain approximate viscous surface information strictly from the geometric configuration and environment without having to generate the surrounding flow field is favorable. Modified Newtonian theory and Fay-Riddle relationship suggest such a method may be possible to formulate. A design process with a wide class of possibilities coupled with rapid analysis techniques demands a robust optimization routine. The addition of an optimization routine tool will greatly enhance the assistance in design process as well as expedite the conceptual design phase. Therefore, a strategic parametric extraction of configuration from the large design space is also desirable.

Inherently, with an expansion of options for the design space, the variety of baseline configuration is increased. This coupled with an increase in the variety of a blunt surface designs yields the potential to bring forth designs with superior optimal performance for the hypersonic regime. In the end, an interdisciplinary hypersonic vehicle design tool must be capable of providing the appropriate aerodynamic, propulsion, thermal, structural, trajectory, controls,

reliability, and maintainability analyses, which is much beyond the scope of the work presented. However, the extent of the potential benefits of the tool and techniques used in its development are vast and can be built upon.

REFERENCES

- [1] Periklis Papdopoulos, Ethiraj Venkatapathy, Dinesh Prabhu, M. P. Loomis, and Dave Olynick, "Current grid-generation strategies and future requirements in hypersonic vehicle design analysis and testing," *Applied Mathematical Modeling*, vol. 23, pp. 705-735, 1999.
- [2] F. Ferguson, "Expanding the waverider design space using arbitrary generating flowfields," Ph.D. 9327413, University of Maryland College Park, Maryland, 1993.
- [3] S. Zhang, "A design concept for the construction of a complete hypersonic vehicle from two-dimensional flow fields," Masters, Mechanical Engineering, North Carolina Agricultural & Technical State University, 2005.
- [4] H. Apdin, "An engineering method for the design and analysis of waverider derived hypersonic vehicles," Masters, North Carolina A&T State University, 2005.
- [5] Haile Lindsay, Frederick Ferguson, Stephen Akwaboa, and H. Apdin. (February 29). *Hypersonic Vehicle Construction & Analysis Using 2D Flow Fields*. Available:
- [6] Terry Lee Corbett Jr., "The design of waveriders from an axisymmetric flowfield," Masters, Mechanical and Chemical Engineering, North Carolina Agricultural & Technical State University, 2006.
- [7] John Anderson Jr, *Hypersonic and High-Temperature Gas Dynamics, Second Edition*: AIAA, Inc, 2006.
- [8] John. (2010, X-51A Waverider sets scramjet endurance record X-51A Waverider reaches Mach 5 in 140s scramjet flight. (484).
- [9] R. T. Volland, L. D. Huebner, and C. R. McClinton, "X-43A Hypersonic vehicle technology development," *Acta Astronautica*, vol. 59, pp. 181-191, 2006.

- [10] G. Emanuel and V. I. Golovichev, "Rocket launched versus hypersonic orbital air breathing combustion propulsion."
- [11] I. M. Blankson and S. Schneider, "Hypersonic Engine Using MHD Energy Bypass with a Conventional Turbojet," presented at the AIAA International Space Planes and Hypersonic Systems and Technologies, 2003.
- [12] Theresa L. Benyo. (2011, August). Flow Matching Results of an MHD Energy Bypass System on a Supersonic Turbojet Engine Using the Numerical Propulsion System Simulation (NPSS) Environment. Available:
- [13] Wikibooks, "Jet Propulsion/Performance."
- [14] D. Rapp, *Human Missions to Mars : Enabling Technologies for Exploring the Red Planet*. Berlin, Heidelberg: Springer Berlin Heidelberg, 2007.
- [15] John Becker, Richard Hallion, John Vitelli, Ronald Boston, C. Geiger, and R. Houston, "The Hypersonic Revolution Case studies in the History of Hypersonic Technology," vol. 1, 1998.
- [16] D. Kuchemann, *The aerodynamic design of aircraft : a detailed introduction to the current aerodynamic knowledge and practical guide to the solution of aircraft design problems / D. Kuchemann*. Oxford ; New York :: Pergamon Press, 1978.
- [17] K. G. Bowcutt, "Optimization of hypersonic waveriders derived from cone flows, including viscous effects," Ph.D, University of Maryland, College Park, 1986.
- [18] S. Corda, "Viscous optimized hypersonic waveriders designed from flows over cones and minimum drag bodies," Dissertation, University of Maryland, 1988.

- [19] Charles E. Cockrell Jr., "Interpretation of Waverider Performance Data Using Computational Fluid Dynamics," presented at the AIAA 24th Fluid Dynamics Conference, Orlando, FL, 1993.
- [20] T. R. F. Nonweiler, "Aerodynamic problems of manned space vehicles," *Royal Aeronautical Society -- Journal*, vol. 63, pp. 521-528, 1959.
- [21] T. Nonweiler, "Delta wings of shapes amenable to exact shock-wave theory," *Royal Aeronautical Society -- Journal*, vol. 67, pp. 39-40, 1963.
- [22] J. W. Flower, "Configurations for high supersonic speeds derived from simple shock-waves and expansions," *Royal Aeronautical Society -- Journal*, vol. 67, pp. 287-290, 1963.
- [23] Y. Qian and H. Sobieczky, "Waverider Design with Parametric Flow Quality Control by Inverse Method of Characteristics," presented at the Institute for Korean-American Studies, 2002.
- [24] K. D. Jones, "A new inverse method for generating high-speed aerodynamic flows with application to waverider design," Ph.D. 9320435, University of Colorado at Boulder, United States -- Colorado, 1993.
- [25] H. Sobieczky, F. C. Dougherty, and K. Jones, "Hypersonic Waverider Design from Given Shock Waves," 1990.
- [26] M. L. Rasmussen, *Hypersonic flow*. New York: Wiley, 1994.
- [27] K. Cui, D. Zhao, and G. Yang, "Waverider configurations derived from general conical flowfields," *Acta Mechanica Sinica*, vol. 23, pp. 247-255, 2007.
- [28] H. Sobieczky, B. Zores, Wang Z., and q. Y.J., "High Speed Flow Design Using Osculating Axisymmetric Flows," 1997.

- [29] Marcus Lobbia and K. Suzuki. Flow Simulation of a Waverider using the Three-Dimensional Euler Equations. Available:
- [30] M. Dhanasar, "The Development of a Benchmark Model for the Design, and Analysis of a Tip-to-Tail Ramjet-Scramjet Propulsion System " Ph. D., Mechanical Engineering, North Carolina A&T State University, 2009.
- [31] S. Corda, "Star-Body Waveriders with Multiple Design Mach Numbers," *Journal of Spacecraft and Rockets*, vol. 46, pp. 1178-1185, 2009.
- [32] F. Wang, H. Ding, and M. Lei, "Aerodynamic characteristics research on wide-speed range waverider configuration," *Science in China Series E: Technological Sciences*, vol. 52, pp. 2903-2910, 2009.
- [33] G. I. Maikapar, "Waveriders of Complicated Shape," *Fluid Dynamics*, vol. 33, 1998.
- [34] A. Bardenhagen, H. Kossira, and W. Heinze, "Interdisciplinary Design of Modern Hypersonic Waverider using the Integrated program PRADO-HY."
- [35] Helmut Sobieczky and Julienne C. Stroeve. (1991). *Generic Supersonic and Hypersonic Configurations*. Available:
- [36] M. A. Lobbia, "A Framework for the Design and Optimization of Waverider-Derived Hypersonic Transport Configurations," Doctor of Philosophy, Aeronautics and Astronautics, University of Tokyo, 2004.
- [37] Frederick Ferguson, Shengyong Zhang, and Hydar Apdin, "A Design Concept for the Construction of a Complete Hypersonic Vehicle from 2D Flowfields," presented at the AIAA/CIRA 13th International Space Planes and Hypersonic Systems and Technologies, 2005.

- [38] Wilson F. N. Santos, "Bluntness Impact on Lift-to-Drag Ratio of Hypersonic Wedge Flow," *Journal of Spacecraft and Rockets*, vol. 46, pp. 329-339, 2009.
- [39] X.-q. Chen, Z.-x. Hou, J.-x. Liu, and X.-z. Gao, "Bluntness impact on performance of waverider," *Computers & Fluids*, vol. 48, pp. 30-43, 2011.
- [40] J.-M. Liu, Z.-Q. Hou, G.-B. Song, and X.-C. Zhu, "Blunted method for waverider and its effect on performance," *Yuhang Xuebao/Journal of Astronautics*, vol. 32, pp. 966-974, 2011.
- [41] D. Tincher and D. Burnett, "Hypersonic Waverider Test Vehicle: A Logical Next Step," *Journal of Spacecraft and Rockets*, vol. 31, pp. 392-399, 1994.
- [42] Denis O. Vanmol and J. D. A. Jr., "Heat Transfer Characteristics of Hypersonic Waveriders with an Emphasis on the Leading Edge Effects," 1992.
- [43] Aubrey M. Cary Jr. and M. H. Bertram, "Engineering Prediction of turbulent Skin Friction and Heat Transfer in high Speed Flow," 1974.
- [44] Mitchel H. Bertram, Aubrey M. Cary Jr., and Allen H. Whitehead Jr., "Experiments with Hypersonic Turbulent Boundary Layers Flat Plate and Delta Wings."
- [45] M. H. Bertram, "Boundary-Layer Displacement Effects in Air at Mach Numbers of 6.8 and 9.6," 1958.
- [46] R.T. Savage and C. L. Jaeck, "Investigation of Turbulent Heat Transfer at Hypersonic Speeds," The Boeing Company 1967.
- [47] W. F. Cope, "Notes and Graphs for Boundary Layer Calculations in Compressible Flow," N. P. L. Aerodynamics Division, Ed., ed. Great Britain: Her majesty's Stationery Office, 1952.

- [48] Robert D. Quinn and F. V. Olinger, "Flight-Measured Heat Transfer and Skin Friction at a Mach Number of 5.25 at Low Wall Temperatures," 1969.
- [49] E. R. G. Eckert, "Engineering Relations for Heat Transfer and Friction in High-Velocity Laminar and Turbulent Boundary-Layer Flow over Surfaces with Constant Pressure and temperature," *Trans. A.S.M.E*, vol. 78, p. 1273, August, 1956.
- [50] M. A. Lobbia, "Payload-Optimized Waveriders: Design and Validation," 2001.
- [51] Mark E. Kammeyer and M. J. Gillum, "Design Validation tests on a Realistic Hypersonic Waverider at Mach 10, 14, and 16.5 in the Naval Surface Warfare Center Hypervelocity Wind Tunnel No. 9," 1994.
- [52] Charles E. Cockrell Jr., Lawrence D. Huebner, and D. B. Finley, "Aerodynamic Characteristic of Two Waverider-Derived Hypersonic Cruise Configurations," July 1996.
- [53] R. W. Miller, B. M. Argrow, K. B. Center, G. J. Brauckmann, and M.N.Rhode, "Experimental Verification of the Osculating Cones Method for two Waverider Forebodies at Mach 4 and 6," presented at the 36th Aerospace Sciences Meeting & Exhibit, Reno, Nevada, 1998.
- [54] T. C. Rolim, P. G. d. P. Toro, M. A. S. Minucci, A. d. C. d. Oliveira, and R. d. C. Follador, "Experimental results of a Mach 10 conical-flow derived waverider to 14-X hypersonic airspace vehicle," *Journal of Aerospace Technology and Management*, vol. 3, pp. 127-136, 2011.
- [55] (1997, February 18, 2012). *Nasa's LoFLYTE Program Flown*. Available:
- [56] S. K. Liu, "Numerical Simulation of Hypersonic Aerodynamics and the Computational Needs for the Design of an Aerospace Plane," 1993.

- [57] John E. Allen, *AERODYNAMICS The science of air in motion*, Second ed.: Granada Publishing, 1982.
- [58] (March 1, 2012). *Earth Atmosphere Model Metric Units*. Available:
- [59] M. Dhanasar, Frederick Ferguson, Nastassja Dasque, I. Blankson, and L. Uitenham, "Quasi-1D Aero_Thermodynamic Flowpath Modeling of an Inversely Designed Morphing Hypersonic Engine," presented at the 50th AIAA Aerospace Sciences Meeting including the New Horizons Forum and Aerospace Exposition, Nashville, Tennessee, 2012.
- [60] J. D. Anderson, *Fundamentals of aerodynamics*. Boston: McGraw-Hill, 2001.
- [61] Nastassja Dasque and F. Ferguson, "The Design And Validation Of Waveriders Derived From Axisymmetric Flowfields," presented at the ASME 2011 Early-Career Technical Conference (ECTC), Atlanta, Georgia, 2011.
- [62] T. Cebeci and A. M. O. Smith, *Analysis of turbulent boundary layers* vol. 15. New York: Academic Press, 1974.
- [63] L. Neal, "A Study of the Pressure, Heat Transfer and Skin Friction on Sharp and Blunt Flat Plates at Mach 6.8," 1966.
- [64] P.M. Danehy, A.P. Garcia, S. Borg, A.A. Dyakonov, J. A. S.A. Berry, (Wilkes) Inman, *et al.*, "Fluorescence visualization of hypersonic flow past triangular and rectangular boundary-layer trips."
- [65] L. F. Crabtree, R. L. Dommert, and J. G. Woodley, "Estimation of Heat Transfer to Flat Plates, Cones and Blunt Bodies," 1970.
- [66] W.H. Press, B.P. Flannery, S.A. Teukolsky, and W. T. Vetterling, *Numerical Recipes*. New York: Cambridge University Press, 1986.

- [67] D. J. V. Lassaline. March 13, 2009). Supersonic Right Circular Cone at Zero Angle of Attack. Available:
- [68] Homer K. Richards Jr., "An experimental investigation of heat transfer rates on a blunt body in hypersonic flow," Aeronautical Engineering, California Institute of Technology, Pasadena, California, 1957.
- [69] AFRL CFD Research Branch, "Air Vehicles Unstructured Solver (AVUS): User Manual," ed, 2005.
- [70] F. Ferguson, N. Dasque, M. Dhanasar, and I. Blankson, "CFD Analysis of Waveriders Derived from Axisymmetric Flowfields for Reentry Applications," presented at the 50th AIAA Aerospace Sciences Meeting including the New Horizons Forum and Aerospace Exposition, 2012.
- [71] C.R. McClinton, J.L.Hunt, R.H. Ricketts, P. Reukauf, and C. L. Peddie, "Airbreathing Hypersonic Technology Vision Vehicles and Development Dreams," presented at the 9th International Space Plane and Hypersonic Systems and Technologies Conference and 3rd Weakly Ionized Gases Workshop, Norfolk, Va, 1999.
- [72] G. A. Simeonides, "Correlation of laminar-turbulent transition data over flat plates in supersonic/hypersonic flow including leading edge bluntness effects," *Shock Waves*, vol. 12, pp. 497-508, 2003.